JØRUND GIMMESTAD HOP

SODIUM EXPANSION AND CREEP OF CATHODE CARBON

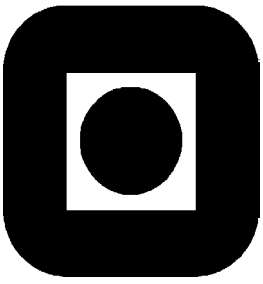

INSTITUTT FOR MATERIALTEKNOLOGI

NORGES TEKNISK-
NATURVITENSKAPELIGE UNIVERSITET
NTNU

AVHANDLING NR. 109 - MAI 2003

This thesis has been submitted to

Institutt for Materialteknologi

Norges Teknisk-Naturvitenskapelige Universitet

Trondheim

in partial fulfilment of the requirements for

the Norwegian academic degree

DOKTOR INGENIØR

May 2003

Preface

This work has been carried out at the Institute for Material Technology, The Norwegian University of Science and Technology, Trondheim. Financial support has been provided by The Norwegian Research Council and the Norwegian Aluminium industry through the PROSMAT program.

I wish to express thanks to my supervisor, Professor Dr. Techn. Harald A. Øye for his interest and guidance during my work.

I also whish to thank Dr. Alexander Zolochevsky for teaching me about time dependent processes and Professor Dr. ing. Trygve Foosnæs for re-reading through the manuscript.

The former SINTEF Applied Chemistry Group, Inorganic Process Chemistry and Analysis, and the rest of the institute are sincerely thanked for their presence in the world.

Summary

An apparatus to measure compressive creep in carbon materials has been developed. Using the final experimental set-up five material properties could be measured in each electrolysis experiment. Creep, sodium expansion, compressive strength and E-modulus were measured for 3 commercial cathode materials at 25 and 980 °C with and without electrolysis. The sodium diffusion coefficient (D) was calculated from the sodium expansion results.

Filler materials for cathode blocks, i.e., certain anthracite and petrol coke qualities, were exposed to sodium vapour to examine crack evolution.

Creep

The three commercial cathode materials were found to deform with time under compression at 25 °C, 980 °C and during electrolysis at 980 °C. Only samples from one block for each quality was studied, so care must be taken before extending the ranking to all classes of cathode materials. The ranking from low to high creep at 980 °C and during electrolysis was:

Semigraphitized < Anthracitic < Semigraphitic

The creep is larger during electrolysis than at 980 °C for all materials and the increase in creep from virgin to electrolysed material at 980 °C is largest for the anthracitic material. Repeated loadings did not influence the shape of the creep strain curve, which could be described by the expression $(\text{time})^n$. The magnitude of the creep strain ranged from 0.01 to 0.07 % with a load of 20 MPa held for one hour. The largest measured creep was approximately 0.35 % after 20 hours of electrolysis in the semigraphitic material.

The stress-strain diagram of the anthracitic material is unchanged before and after electrolysis and exhibits a more linear behaviour than in the other materials. The stress-strain diagram of the semigraphitic and semigraphitized materials changes after loading and tend to increase after electrolysis.

Cracks

All anthracite grains cracked to some extent after being exposed to sodium vapour at 800 °C. The lowest heat treated grains cracked the most. Cracks

through grains were also found in the commercial material during electrolysis. In the petrol cokes only grains calcined to 1500 °C with a structure characterised by a gradient from mosaic to flow was observed to crack after exposure to sodium vapour at 800 °C.

Diffusion coefficient

The diffusion coefficient of sodium in carbon during electrolysis has been calculated with three different solutions of Fick's law and is found to increase with current density and graphitic character of the material. Two of the calculations were based on the expansion of the sample (penetration from bottom and radial penetration) and one on a rather few measured sodium concentrations. The diffusion coefficient was calculated to be in the range $8 \cdot 10^{-5}$ to $5 \cdot 10^{-4}$ cm^2/s at current densities from 0.06 to 0.88 A/cm^2, which is around 10 times larger than reported before (Table 2.1). The cryolite ratio did not influence D as the saturation time for samples in acidic or basic melt was the same.

The ranking from larger to smaller diffusion coefficient in the studied materials was

Semigraphitized > Semigraphitic > Anthracitic

The diffusion coefficient increased with heat treatment temperature in some laboratory produced materials.

1. Introduction

1.1 The Hall-Heroult process [1]

The inventors of the process, Hall and Heroult, discovered independently of each other the electrochemical process to reduce alumina (Al_2O_3) to aluminium metal at about 950 °C. The process has successfully withstood the many attempts to replace it since 1886. The overall cell reaction is given in Eq. (1.1) and a principle drawing of a commercial prebake cell is shown in Figure 1.1.

$$2\ Al_2O_3\ (dissolved) + 3\ C\ (s) = 4\ Al\ (l) + 3\ CO_2 \qquad (1.1)$$

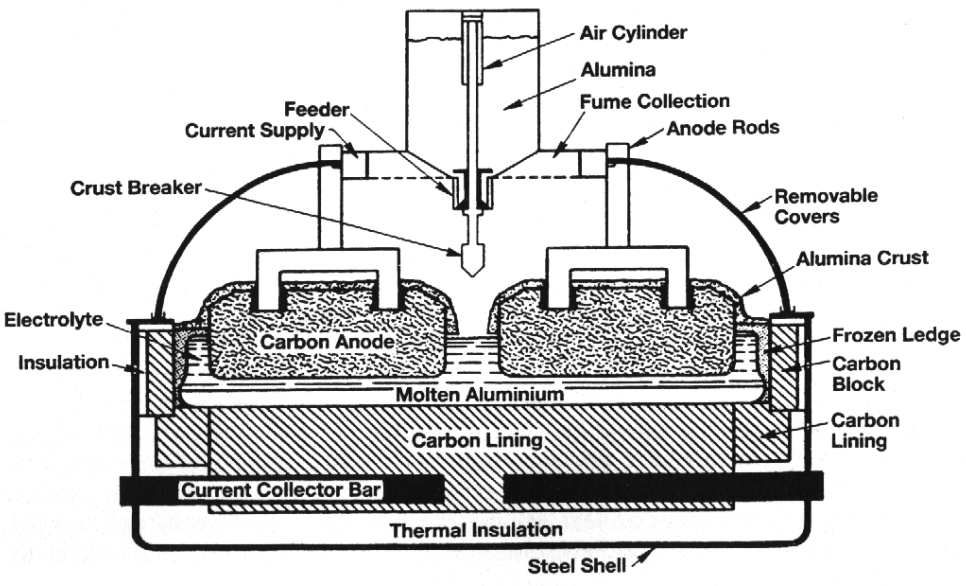

Figure 1.1. Hall-Heroult cell with prebaked anodes [1].

Alumina is dissolved in the electrolyte (Na_3AlF_6 with additions of AlF_3) and reduced to aluminium at the bath/metal interface. The anode is dipped into the electrolyte (bath), and oxygen from the alumina reacts electrolytically with the anode carbon, which gradually is consumed by the formation of gaseous carbon dioxide (CO_2). A height of 15-30 cm liquid aluminium is retained in the cell due to poor wetting. The height of the bath is often in the

same range as the aluminium (20 cm) and the distance between the anode and the top of the aluminium pad (interpolar distance) is typically 4 to 5 cm.

The two most common technologies are Søderberg and Prebake technology. Søderberg anodes are continuous and self-baking, which in principle is advantageous. Anode paste briquettes are added on top of the Søderberg anode, and while the paste passes slowly downwards through a rectangular steel casing, it is baked into a solid anode. Because of lower pollution and total production costs, the Prebake cells with a regular anode change are favoured. The anode is of a better quality and the anode consumption is lower. Still the consumption is higher than the theoretical value of 333 kg C/tonne of Al (~400 for prebake and 500 - 550 kg C/tonne for Søderberg).

In modern prebake cells the alumina is supplied from an overhead bin or hopper and 1 to 2 kg alumina is added every 1 to 2 minutes. It is important that the alumina is dissolved and mixed rapidly in the bath after addition, and that "sludge" or "muck" (undissolved bath/alumina) is not formed under the liquid aluminium. Alumina is also used on top of the frozen bath for thermal insulation and on top of the carbon anodes to prevent air burn. An additional role of alumina is to reduce the emissions by cleaning the anode gas with the "dry scrubbing" method. Alumina powder is used to adsorb the hydrogen fluoride gas evolved, and also to entrap the other vapours, which are mainly gaseous sodium tetraflouroaluminate ($NaAlF_4$). This "secondary" alumina is the used as the feeding material in the cells.

The term “cathode” is often considered as the whole container of the cell, but is from an electrochemical point of view the interface between the aluminium metal and the electrolyte. The carbon cathode conducts current to the cell and special properties are needed to withstand the corrosive environment and stresses attributed to temperature and chemical reactions.

The carbon part of the cathode mainly consists of prebaked or graphitized carbon blocks joined by a carbonaceous seam mix. Steel current collector bars are inserted into grooves at the bottom of the blocks. Layers of refractory and insulation bricks are located underneath the blocks. The carbon lining materials are contained in a rectangular outer steel shell.

After start-up sodium from the melt is absorbed in the carbon cathode and the wetting conditions are changed. This allows the electrolyte to enter the carbon block and further down into the refractory. The electrolyte stops only when it reaches its freezing point in the refractory. The content of electrolyte in the carbon cathode can be up to 35 %.

1.2 Carbon cathodes

The building stone of carbon cathodes are based on the layered graphite structure (Figure 1.2). The graphene layers tend to orient themselves in the length direction in the more or less oval particles (anthracite, graphite or petroleum coke) used as aggregate in the cathode manufacturing. The coke is mixed with a pitch binder and extruded or vibrated into a rectangular body, which is heat treated to temperatures between 1000 and 3000 °C. During forming the particles tend to orient parallel to the extrusion direction or perpendicular to the vibrating direction and the material properties will depend on the direction they are measured.

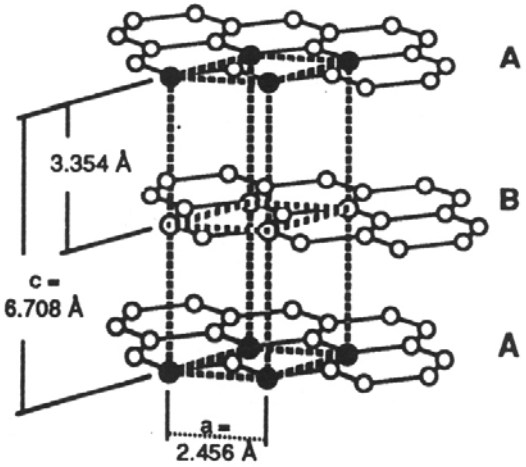

Figure 1.2. The unit cell of graphite [2].

As the heat treatment temperature of the material increases the structure approaches a more graphitic structure (Figure 1.3) dependent on raw material and heat treatment temperature. Properties like compressive and tensile strength, elastic (Young's) modulus, electrical conductivity and thermal conductivity are larger parallel to the graphitic planes (parallel with the extrusion direction and perpendicular to the vibrating direction), while the thermal expansion is larger perpendicular to the layers. The carbon-carbon bonds in the a-direction of the unit cell (Figure 1.1) are strong covalent bonds, while the bonds between the layers (c-direction) are weak van der Waals bonds.

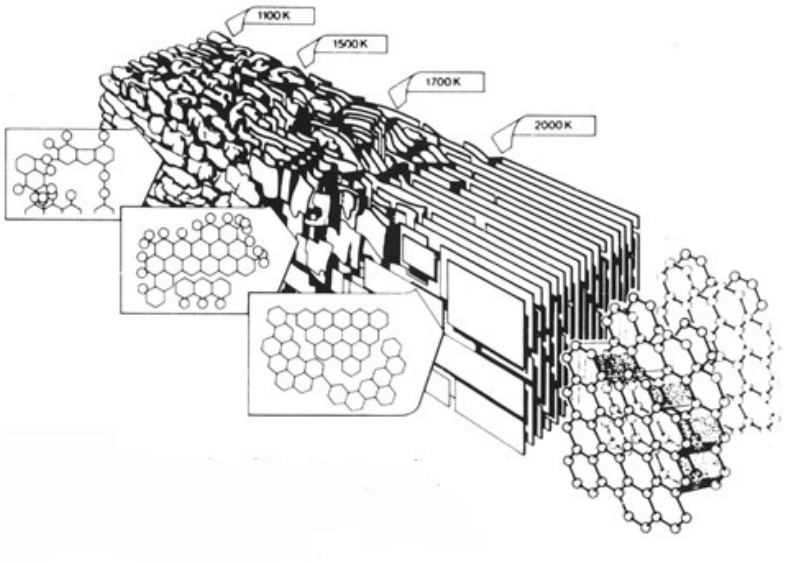

Figure 1.3. The carbon structure at different heat treatment temperatures [2].

Table 1.1. Properties of 3 extruded cathode qualities from two different suppliers. When a range is given, the value cover the property both parallel and perpendicular to the extrusion direction.

Type of block (aggregate in parenthesis)		**Anthracitic (30 % graphite)**		**Semi –graphitic (100 % graphite)**		**Semi – graphitized (100 % petr. coke)**	
		I	**II**	**I**	**II**	**I**	**II**
Real density	**g/cm^3**	1.95	1.94	2.16	2.09	2.21	2.19
Bulk density	**g/cm^3**	1.58	1.54	1.65	1.59	1.62	1.60
Total porosity	**%**		20		24		27
Open porosity	**%**	15		19		20	
Crushing strength	**MPa**	31	22-24	27	23-24	35	21-23
Bending strength	**MPa**	10	6.5-7.5	10	8-10	13	9-11
Youngs modulus	**GPa**	11	7-9	9	6-8	7	5-7
Specific el. res	**μΩm**	25	30-41	13	18-23	11	11-13
Linear thermal exp. coeff.	**μm/Km**	1.9	2.7-3.8	1.8	2.8-3.4	3.8	2.5-3.0
Therm. cond.	**W/mK**	17	10-12	50	22-28	115	100-125
Ash content	**%**	2.5	2.3	0.3	1.2	0.3	1.0
Sodium expansion	**%**	0.5	0.4	0.4	0.25	0.2	0.03

The three main categories of cathode blocks for aluminium reduction cells are anthracitic, semigraphitic and semi- or fully graphitized and is in the written sequence recognised by an increased graphitic character. Some properties and constituents of some chosen qualities from two manufacturers are shown in Table 1.1. The given ranges cover properties both parallel and perpendicular to the extrusion direction.

1.3 Aim of the work

The cell life is wanted as long as possible, as costs are related to relining and loss of aluminium production. The life is determined by the first material to fail inside the steel shell. The cell could fail by a number of reasons but the present focus is on the cathode blocks. During startup the cathode could fail by stresses induced by strains from temperature differences, or by penetrating sodium. The stresses built up in the carbon cathode will remain for several years and mechanical properties related to time are important. An extreme unwanted situation shown is shown in Figure 1.4 where the cathode is cracked in the middle. This could express the motivation for the work.

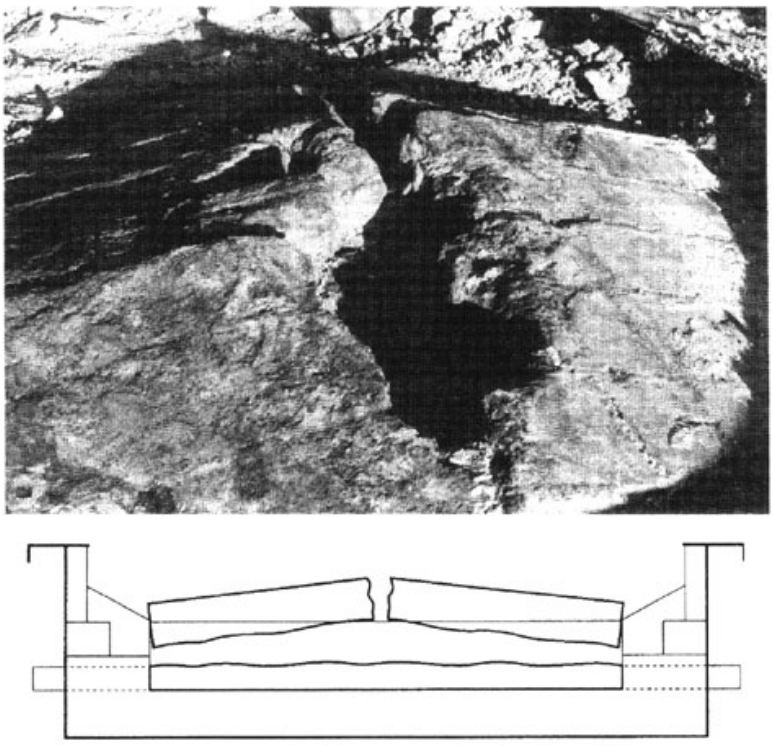

Figure 1.4. Extreme case of cathode failure [3].

2. Deformation of the carbon cathode

Apart from the deformation caused by temperature and external pressures, the expanding effect of the penetrating sodium is among the most crucial. The extent of the sodium expansion is in the range of the thermal expansion from 25 °C to 1000 °C [3]. The different experimental conditions influencing the sodium expansion are discussed in Chapter 2.3, but first the formation and penetration of sodium will be discussed.

2.1 Formation of sodium in the carbon cathode

Sodium in aluminium will be in equilibrium with the melt species (NaF and AlF_3) according to Eq. (2.1) and react further to sodium in carbon Eq. (2.2). Some sodium could also be electrochemically reduced in carbon Eq. (2.3).

The electrochemical transport number for Na^+ is close to one in cryolite-alumina melts. Since aluminium containing species are reduced at the cathode, the electrolyte at the cathode/electrolyte interface is richer in NaF than the bulk electrolyte. Hence the activity of sodium in aluminium will be higher than what is expected from the electrolyte composition [4].

$$Al\ (l) + 3\ NaF\ (in\ cryolite) = 3\ Na\ (in\ Al) + AlF_3\ (in\ cryolite) \qquad (2.1)$$

$$Na\ (in\ Al) = Na\ (in\ C) \qquad (2.2)$$

$$Na^+ + e^- = Na\ (in\ C) \qquad (2.3)$$

Thonstad and Rolseth [5] measured the overvoltage at 1010 °C at different CR's (cryolite ratio = mol NaF / mol AlF_3) and CD. As the overvoltage (η) was dependent on stirring (diffusion controlled) and some scatter in the results was measured, no concluding equation was put forward, but Eq. (2.4) could be fitted to the data.

$$\eta = \frac{RT}{F}\ln\left(\frac{a_{Na}}{a^*_{Na}}\right)^{1010^oC} \approx 0.25 + 0.028 \cdot CR - (0.31 - 0.031 \cdot CR)\ log\ (CD) \qquad (2.4)$$

where a_{Na} and a^*_{Na} are the activities of sodium in the bulk melt and at the aluminium surface respectively and CD is current density in A/cm^2.

During a startup without aluminium addition, and in laboratory scale cells, no aluminium is present and the carbon cathode is directly exposed to the electrolyte. Sodium could in these cases be formed according to Eq. 2.1 and Eq. 2.2 if aluminium metal is produced, however electrochemical reduction of sodium in carbon (Eq. 2.3) is more probable than the reduction of both sodium and aluminium on an aluminium or carbon cathode [6] as discussed in the next section.

2.1.1 Electrochemical deposition of sodium

As an introduction to electrochemical reduction of alkali metal in carbon the work of Xu et al. [7] is discussed. These authors measured the reduction potential of lithium both as lithium metal on graphite and on lithium inserted in the graphite cathode. A molybdenum wire was used as reference electrode and a carbon crucible as the counter electrode in a cell with molten LiCl at temperatures between 650 and 900 °C.

At 650 °C a potential of –1.9 V for deposition of metallic lithium was measured on the molybdenum electrode (Figure 2.1), while on the graphite electrode the potential for lithium deposition was easier and started as high as –0.5 V at 650 °C (Figure 2.2). The reason for the shift of the discharge potential to considerably more positive values was explained as Li^+ was stabilised in the graphite bulk. The reduction potential of lithium in the graphite electrode became even less negative as the temperature increased.

The voltammogram for reduction of lithium on the molybdenum cathode showed a distinct break-off at potential lower than – 1.9 V and followed a straight line corresponding to the IR – drop (Figure 2.1). When the graphite was used as the cathode (Figure 2.2) the potential did not reach this linear shape and when the potential was increased (at -2.0 V in Figure 2.2) the curve was shifted to higher potentials. The reduction potential was reported to depend on the lithium concentration in the graphite sample.

The diffusion of penetrated lithium into the graphite matrix was proposed to be the rate controlling mechanism. When potentials more negative than -3.8 V was applied, the current versus time plot exhibits abrupt fluctuations of the measured current and an eroded sample was observed. Some of the eroded material (explained as exfoliated) was in another article found to be nano materials [8]. Nano materials were also achieved by electrolysis of molten NaCl with a graphite cathode, but the cathode potential was not reported.

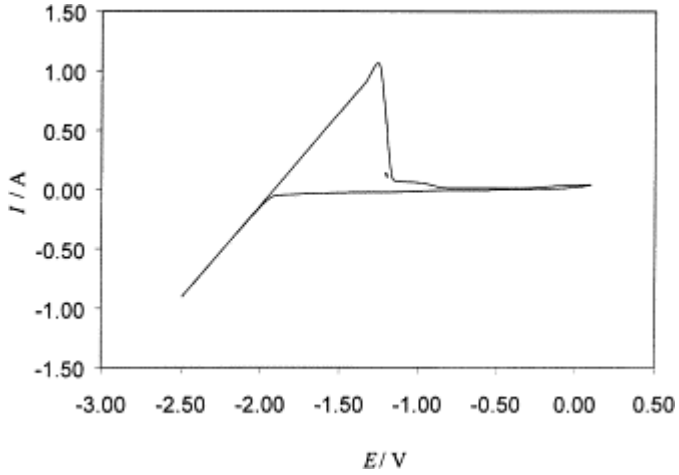

Figure 2.1. Cyclic voltammogram for a molybdenum electrode in molten LiCl at a potential scan rate of v=100 mV s^{-1} at 650 °C [7].

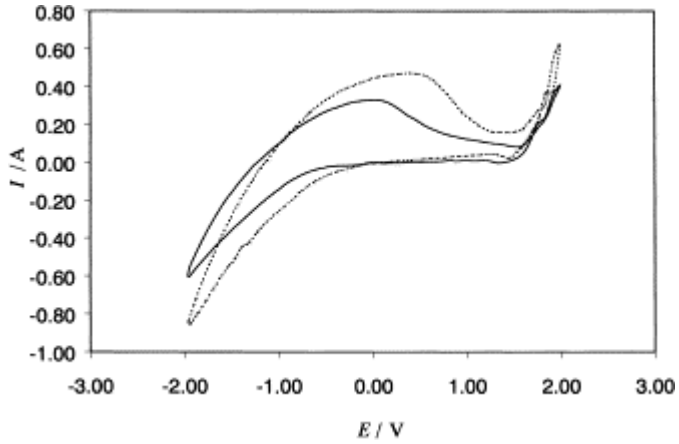

Figure 2.2. Cyclic voltammograms for a graphite electrode in molten LiCl at a potential scan rate of v=100 mV s^{-1} (solid line at 650 °C and dashed line at 900 °C) [7].

Several authors have measured the potential for sodium to penetrate into carbon in electrolytic cells at temperatures below 100 °C [9-12]. Carbon and sodium metal are used as electrodes and a polymer is used as electrolyte. When sodium is deposited in the carbon in these cells, they work like galvanic cells and during charging (electrolysis) the sodium goes out of the carbon. The deposition voltage for sodium in carbon is higher (easier penetration) than for lithium.

Joncourt et al. [12] measured the deposition voltage for sodium in pitch coke heat treated to temperatures between 800 °C and 2200 °C at room

temperature. The pitch coke was the anode and sodium metal was used as cathode. An organic electrolyte ($P(EO)_{12}NaCF_3SO_3$ [P(EO) = commercial 5 M polyethylene oxide]) was used to conduct sodium. The voltage for deposition was higher when the heat treatment temperature of the pitch coke was lower. This is shown in Figure 2.3 (a) where the threshold voltage for the coke heat treated at 800 °C is the highest. The evolution of the d – 002 peak for the sample heat treated at 800 °C is shown in Figure 2.3 (b). The d – 002 distance increases with the sodium content. An inverse relationship between the deposition voltage and the heat treatment temperature of the pitch coke was found.

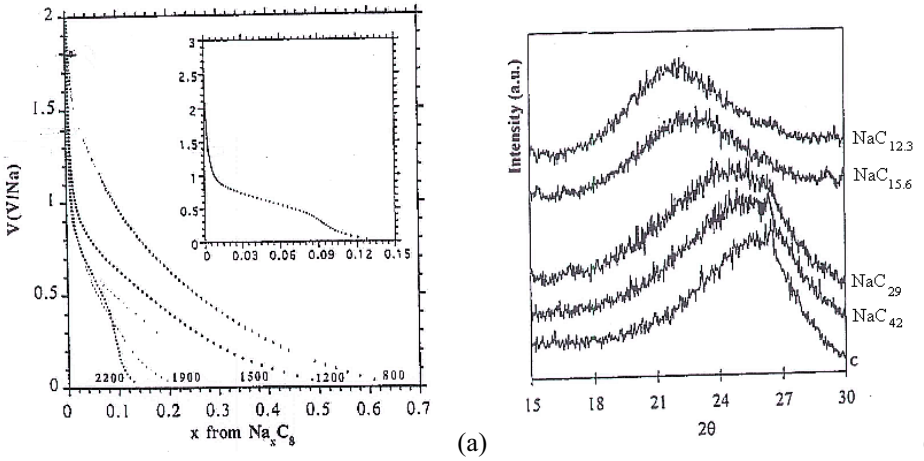

Figure 2.3. Voltage as a function of sodium concentration in carbon heat treated to different temperatures (a) and the X – ray diffraction around the 002 – peak for the pitch coke heat treated to 800 °C (B). The inset in Figure (a) shows a zoom in for the coke heat treated to 2200 °C [12].

In the more disordered carbons (lower heat treatment temperature) a larger amount of sodium was deposited (Figure 2.4). Not all the sodium was found to penetrate between graphene layers, some of the sodium was believed to be adsorbed in porosity [12].

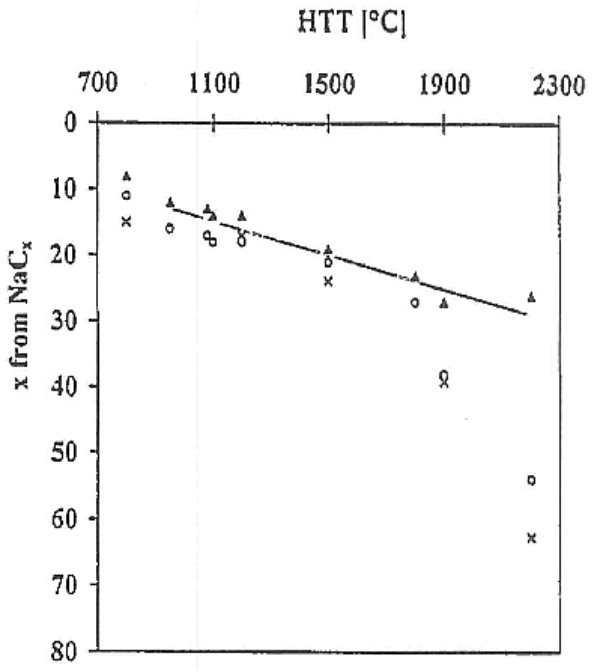

Figure 2.4. Variation in the sodium uptake in pitch coke samples as a function of HTT. ▲ - total uptake determined from the elemental analysis; o – uptake of sodium determined from the X – ray diffraction patters (movement of d_{002} line); x –uptake of electrochemically intercalated sodium determined from coulometric measurements [12].

In addition to electrochemical formation of aluminium and sodium, aluminium carbide is formed at the cathode. Gudbrandsen et al. [13] studied the formation of aluminium carbide at different current densities in a cell with stirring. It was suggested that carbon dissolved cathodically according to Eq. (2.5).

$$C(s) + 3AlF_3(l) + 4Na^+ + 4e^- = Na_3Al_3CF_8(l) + NaF(l) \qquad (2.5)$$

At current densities above 0.1 A/cm^2 no increase in aluminium carbide formation was measured (limiting current density). The measurements were based on the volume loss of the graphite. The current efficiency for aluminium carbide production was around 80 % at current densities below 0.1 A/cm^2 and the loss of current efficiency was explained by reduction of contaminants and sodium.

The deposition of Al_4C_3 [13] and probably sodium in carbon [6] will take place at voltages below the voltage for reduction of aluminium as long as the carbon is not saturated with sodium. To produce aluminium the current density must be higher than the limiting current density for Al_4C_3 (~0.1

A/cm^2 on graphite) and probably higher than the ability of the carbon to transport sodium from the surface into the carbon bulk (as expressed by the diffusion coefficient of the carbon). If a relatively high constant current is applied (~ 0.7 A/cm^2), all the species (Al, Al_4C_3 and Na) will probably form.

Aluminium wets carbon poorly [4] and in electrolysis experiments with a vertical cathode (presented in Chapter 3.6-3.7), the produced aluminium will not stick to the cathode and the carbon surface will be exposed to the electrolyte. In a full-scale cell the produced aluminium will cover the carbon cathode although a thin layer of melt could be present below the aluminium pad [4] transporting melt compounds to the carbon surface.

If the main mechanism for sodium formation in carbon is direct reduction, Eq. (2.6) describes the surface concentration of sodium if this is the only reaction occurring on the surface [7] when the assumptions listed below are made.

- The reduction process is rate controlled by the diffusion of sodium in carbon.
- Reversible electrode process (Nernst equation).
- The concentration of sodium ions in the electrolyte is selected as the standard state for the activity of sodium ions.
- The concentration of sodium in carbon is selected as the standard state for the activity of sodium in carbon.

$$c_{Na}(x=0) = \frac{c_{Na}^{*}}{r_{Na}} \exp(-\frac{E - E^{0}}{RT} F) \qquad (2.6)$$

where

$c_{Na}(x=0)$: Sodium concentration in the carbon at the electrolyte/carbon interface
c_{Na}^{*} : Saturation concentration of sodium in carbon
r_{Na} : Henrian activity coefficient of sodium in carbon
E : Applied potential
E^0 : Standard potential of the half-cell reaction expressed by Eq. (2.3)

2.1.2 Sodium vapour uptake in carbons

On an aluminium cathode at the cryolite composition, aluminium is more noble than sodium by about 250 mV [14]. The overvoltage on the cathode increases with increasing current densities (CD) and decreasing CR [5]. At (CD) above 1.0 A/cm^2 the overvoltage is around –200 mV, and sodium bubbles start to appear. At higher CR a lower CD is needed to produce sodium bobbles.

Graphite intercalation compounds are synthesised by exposing graphite to alkali metal vapour. The alkali metal intercalates the graphene layers and a new compound with a new unit cell is formed. Sodium is in this context an exception as the intercalation in graphite is difficult with the pure substances [15]. The richest synthesised sodium intercalation compound was for a long time NaC_{64} [16]. Later Metrot et al. [17] synthesised richer compounds. The formation of the compounds was reported to be favoured by the presence of small amounts of impurities and low temperature (150 - 400 °C). Herold et al. [18] synthesised intercalation phases by mixing graphite with molten sodium in different alkali halides (NaI, NaBr and NaCl). New phases were not achieved with NaF (which exists in an aluminium cell), probably because NaF have the highest lattice energy of the tested sodium halides. The alkali content increased with increasing temperature; an exception in the graphite intercalation chemistry.

Several authors have measured the uptake of sodium vapour in different carbons [15, 17, 19, 20]. The general trend is higher absorption as the disorder in the carbon increases. The existence of faults (which are electron acceptors) has the effect of lowering the Fermi level of the carbons with respect to the Fermi level of graphite. This allows penetration of an electron donor like sodium. This effect diminishes gradually as the temperature of heat treatment (HTT) increases [21].

Sechet et al. [20] studied the uptake of sodium at 700 °C in pitch coke and anthracite heat treated from 800 to 2400 °C (Figure 2.5). In the X-ray diffraction studies of the sealed samples, a displacement of the 002 line and an intercalation phenomenon was found. They proved their sodium contents to be similar as Metrot et al. [15] (Figure 2.6) and Robert et al. [21]. These authors measured the sodium content at 380 °C and the sodium absorption was concluded to be independent of the carbon temperature in the range 300 °C to 700 °C.

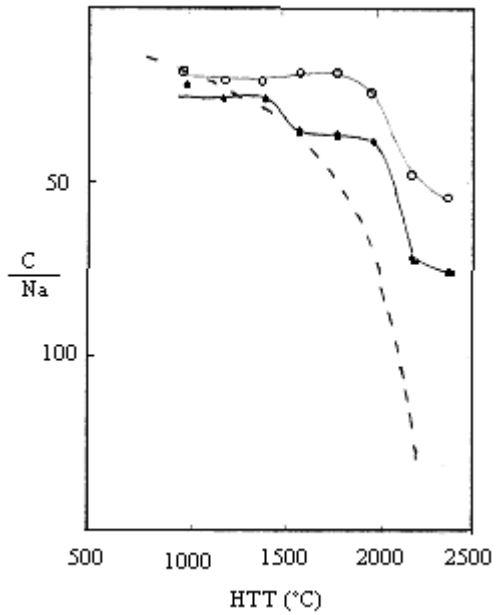

Figure 2.5. Variation in the amount of sodium intercalated in the coke samples as a function of heat treatment temperature (HTT). Dotted line: data obtained with the pitch-coke, full circles: anthracite samples, $P/P_0 = 0.2$, open circles anthracite samples, $P/P_0 = 0.9$ [20].

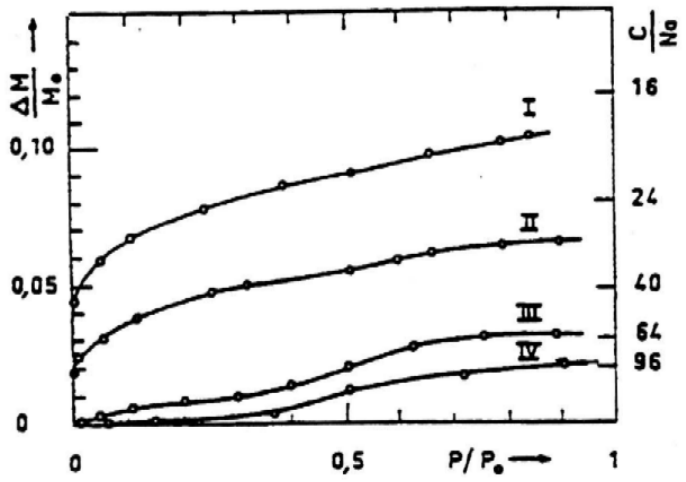

Figure 2.6. 600 °C isotherms of sodium sorption in petroleum cokes. I: HTT 1250 °C, II: 1600 °C, III: HTT 2000 °C, IV: HTT 2400 °C [15].

Mikhalev and Øye [19] studied the uptake of sodium in commercial cathode materials (Figure 2.7). The absorption isotherms had the form typical for surface adsorption and had a good fit to the general BET isotherm, except for graphite. The BET surface calculated from the sodium was larger than

the surface calculated for helium. The sodium should therefore penetrate smaller pores than helium (microporosity) and a ionization of sodium was believed to be an important mechanism.

The much lower absorption of sodium in graphite was also found for higher heat treated materials by Joncourt (Figure 2.4). In agreement with the authors above [15, 20], the more amorphous materials absorbed more sodium. An increase of absorption with decreasing temperature (950 °C – 750 °C) was also found.

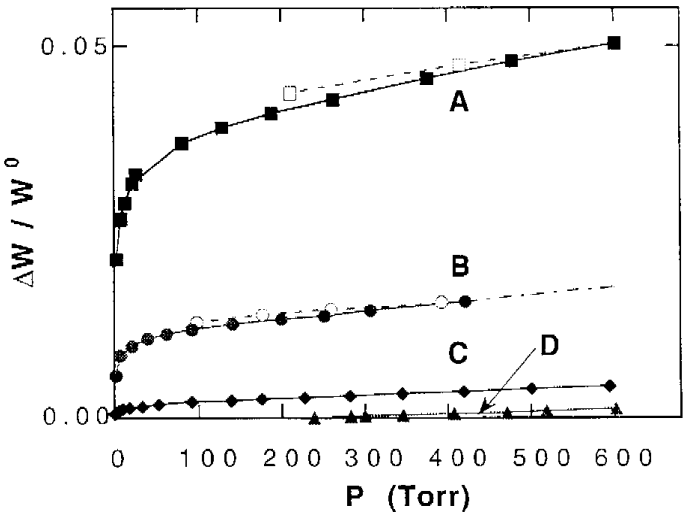

Figure 2.7. Sodium absorption isotherm at 1227 K for $\Delta W/W^0$; increase in weight relative to original weight of carbon materials A-D. Filled symbols; increase in pressure; open symbols: decrease in pressure. A – anthracitic, B – semigraphitic, C – semigraphitized, D – graphite [19].

In graphite new intercalation compounds are formed with sodium, at least if some impurities are present. In less ordered carbons the sodium is adsorbed/absorbed between the graphene layers and in microporosity. The absorption decreases with increasing temperature and crystallinity of the less ordered carbons.

2.2 Sodium penetration mechanism

The penetration of sodium is as reviewed in the previous section explained as penetration between the graphene layers and adsorption in micropores. The transport of sodium in carbon cathodes was first explained by Dell [22] as a vapour diffusion mechanism as sodium is above its boiling point. Later

Dewing [23] argued for a lattice diffusion mechanism. Other authors have agreed with the lattice diffusion mechanism, as the penetration distance is proportional to the square of time [24, 25]. The reported diffusion coefficients are rather large for lattice diffusion, and as discussed below, the penetration distance of sodium could also be proportional to the square of time if another mechanism is operative.

Herold [26] discussed different mechanisms of intercalation. Two mechanisms were proposed. A slow diffusion controlled reaction where the stage number remained unchanged (isostage) described by a substituting reaction. The other mechanism, a very fast mechanism, was related to a change in stage and is the most common reaction. The intercalation was here explained as an "invasion" of the graphite interspaces by dense reagent layers implying a movement of graphene sheets. This matter transfer process, which is closer to a hydrodynamic than to a diffusion type could be called a "sliding process". If ΔG is the free enthalpy of formation of a given compound $C_x i$ (i = intercalate) and $\Delta\Sigma$ is the surface area covered by i, the progression of the intercalated layer could be expressed by a force of traction per unit length $\gamma = -\Delta G/\Delta\Sigma$, which corresponds to a surface tension. The intercalation depth, x and velocity dx/dt was expressed as a friction force of $f = K \cdot L \cdot x \cdot dx/dt$, where K is a constant depending on the nature of the intercalant. The mathematical solution for the depth of the intercalant was then $x = 2 \cdot (\gamma/K \cdot t)^{1/2}$, where the penetration distance is proportional with the square root of time.

The detailed penetration mechanism is uncertain, but will in this work be assumed to be a diffusion process.

2.2.1 Diffusion mechanism, diffusion coefficient

The diffusion in a solid is in general faster along the grain boundaries than in the bulk material. Since the boundaries are thin, most of the diffusing material is lost in the grains, even though the boundary diffusion coefficient is much larger than the lattice diffusion coefficient. When volume diffusion is dominant, the log(concentration) of the diffusing element decreases with the square of the distance from the surface. When boundary diffusion predominates, the log(concentration) decreases linearly with the distance from the surface [27, p. 242].

In cathode materials the aggregate consists of particles with sizes from fine dust up to above 1 cm mixed in a pitch binder. Both materials (binder and aggregate) consist of a more or less ordered graphite structure, with the filler

usually the most ordered. Rice [28, p.2] defines a grain as the primary microstructural unit in polycrystalline bodies. If the surface between each crystal unit is defined as the grain boundary, a substantial part of cathode materials is grain boundaries. If the boundary between the particles and the binder pitch is defined as grain boundary, this will also give a large surface as the surface area of dust and porous particles are large.

When the diffusion coefficient of sodium in different carbons are reported in the literature, the grain boundaries are seldom discussed and a homogenous material is assumed. The reported diffusion coefficients will be an effective diffusion coefficient describing the movement on a macro level.

An overview of reported diffusion coefficients for sodium in cathode materials was given by Zolochevsky et al. [29] (Table 2.1). The calculated diffusion coefficients were higher than most previously reported values and were dependent of the current density.

Table 2.1. Overview of reported diffusion coefficients for Na in cathode materials [29].

T [°C]	CR	i [A/cm^2]	Carbon type	D [cm^2/s]	Reference
980	4	0.7	semigraphitic	$3.99*10^{-4}$	[29]
980	4	0.2	semigraphitic	$1.86*10^{-4}$	[29]
980	4	0.06	semigraphitic	$1.21*10^{-4}$	[29]
920	2.2	0.7	semigraphitic	$0.4 - 0.8*10^{-5}$	[30]
970	2.2	0.7	semigraphitic	$0.5 – 1.2*10^{-5}$	[30]
730			graphite	$0.9*10^{-5}$	[31]
730			coked pitch	$1.1*10^{-5}$	[31]
850			coked pitch	$0.9*10^{-5}$	[31]
850			vitreous	$0.6 – 1.0*10^{-5}$	[31]
850			anthracite	$2.9*10^{-5}$	[31]
950			anthracite	$8.4*10^{-5}$	[32]
970			anthracite	$4.3*10^{-5}$	[33]
970			anthracite	$1.4*10^{-5}$	[22]
980		0.98	anthracite	$4*10^{-5}$	[34]
980			petroleum coke anthracite	$2.5\text{-}5.5*10^{-5}$	[23]
1000			anthracite	$6.3*10^{-5}$	[35]

When a current is conducted through an electrolysis cell, an electric field will arise. An electric field will influence the charged substances. Taking into account that two species (sodium and electrons) are mobile in the structure and that carbon is an electronic conductor the more mobile species (i.e. electrons) move quicker than the ionic species. This creates an internal

electric field in which the slower species are accelerated and the faster ones retarded in order to maintain local charge neutrality. The influence of charged species upon the transport of each other is quantified by the factor W, called the enhancement factor [36, 37]. The definition of W in the case of lithium insertion in carbon was expressed by the activity gradient of the intercalated species (Eq. 2.7).

$$\frac{d\ln a_{Li_xC_6}}{d\ln x} = W \tag{2.7}$$

The intrinsic diffusion coefficient of the mobile species, D, (electronic or ionic species) could be calculated by Eq. (2.8). The self-diffusion coefficient, D_K, is a measure of the random motion of intercalated lithium in a crystal without a concentration gradient.

$$D = D_K \frac{d\ln a_{Li_xC_6}}{d\ln x} \tag{2.8}$$

The enhancement factor was calculated by comparing the above equations to the potential of the electrolytic cell (Eq. 2.9).

$$\frac{dE}{d\ln x} = -\frac{RT}{F}\frac{d\ln a_{Li_xC_6}}{d\ln x} = -\frac{RT}{F}W \tag{2.9}$$

The enhancement factor was calculated from coulometric curves and the diffusion coefficient was found to decrease from $2\cdot10^{-7}$ cm^2/s to $1\cdot10^{-8}$ cm^2/s in going from carbon to $Li_{0.5}C_6$.

Funabiki [38] followed the phase boundary movement of Li in a HOPG (Highly Oriented Pyrolitic Graphite) in an optical microscope. A higher penetration speed in the surface region (5-10 μm/min) than in the bulk material (less than 3 μm/min) was found. In Figure 2.8 (a) the penetrating lithium is seen in the bottom right corner as a dark area. After 4 minutes the lithium has penetrated further and the crack located in the right bottom of Figure 2.8 (a) grows to the centre of the image (Figure 2.8 b). After 9 and 21 minutes (Figure 2.8 c and d) the lithium penetration continues and the structure cracks more. The penetration was reported to be slower across the cracks.

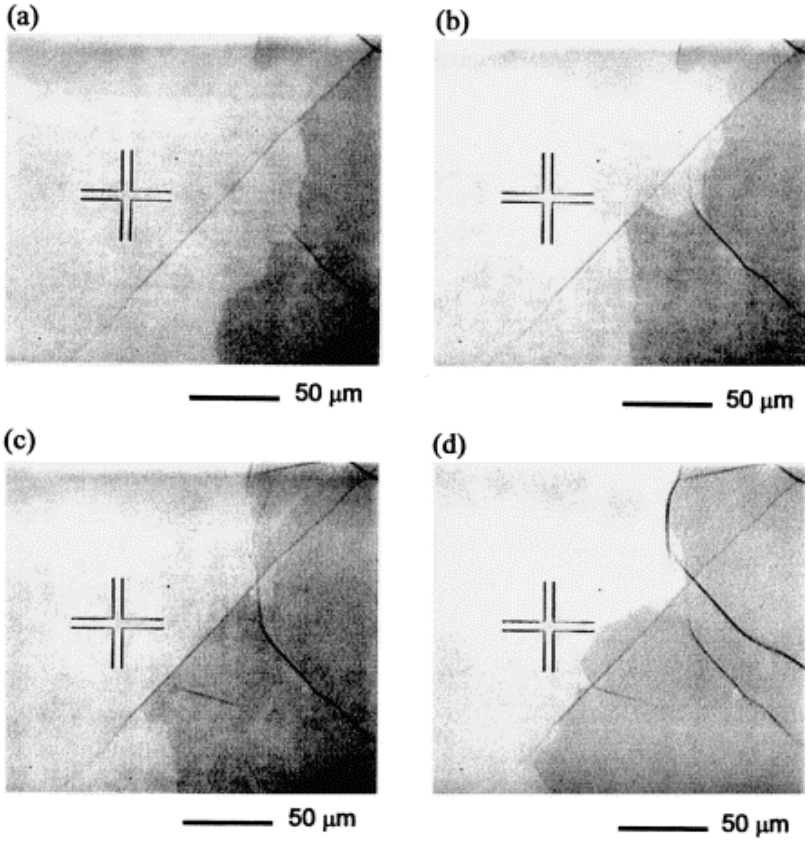

Figure 2.8. Optical microscope images around cracks located far from the surface. Images (b), (c) and (d) were obtained at 4, 9, and 21 min, respectively, after the image (a) was observed [38].

The penetration of sodium in carbon could consist of more than one mechanism. In electrolytic cells the magnitude of the current and structure differences will influence the diffusion.

2.2.2 Concentration profiles

The sodium concentration profile reported by Dell [22] in carbon cathode samples exposed to electrolysis does not distinguish between sodium from the melt compounds and the metallic sodium. Melt compounds like NaF, Na_3AlF_6 and β-alumina ($Na_2O{\cdot}11Al_2O_3$) [24, 30] contain sodium that is not a part of the sodium that penetrates the crystal lattice. In some cases the Na concentrations are measured with the method described by Sleepy [39], where the sodium in the carbon is left to react with water to NaOH, and the amount of sodium is determined by titration. If these samples contain

fluorine from penetrated melt compounds, the analysis will be wrong (Appendix A).

Houston et al. [31] measured the concentration profile of sodium in vitreous (glassy), anthracitic and pyrolytic carbon cathodes. The experiments were performed in sodium chloride potassium - chloride melts. The sodium concentration was measured by the technique of energy dispersive analysis of X – rays (EDAX). In this study the samples were allowed to cool in the furnace in protective atmosphere, and then mounted in an epoxy resin. No electrolyte was observed to penetrate the samples. The concentration profiles (Figure 2.9) were reported not to follow the diffusion profile calculated from Fick's 2nd law. To follow a diffusion curve, the concentration near the surface should be higher. The authors did not mention that the sodium near the surface could be lost during cooling. As observed in the sodium vapour experiments, the sodium escapes the structure when the sodium pressure is reduced [19]. In sodium batteries at room temperature the sodium penetration is reversible and when the current is switched off, sodium will diffuse back to the electrolyte [9-12]. The sodium close to the surface could in the experiments of Houston et al. [31] move back to the melt and cause the deviation from a diffusion concentration shape.

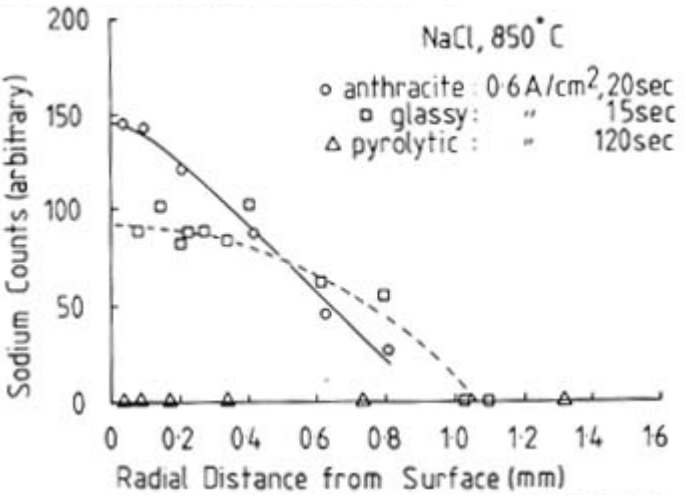

Figure 2.9. Concentration profile of sodium in carbon species after electrolysis in molten NaCl [31].

2.2.3 Relevant solution of Fick's 2nd law [40]

If the driving force for sodium penetration is determined by concentration differences, Fick's law can describe the movement of sodium. The 1st law is described with Eq. (2.10)

Ficks 1st $$F = -D\frac{dC}{dx} \tag{2.10}$$

where F is the rate of transfer per unit area of section, C the concentration of diffusing substance, x the space coordinate measured normal to the section, and D the diffusion coefficient. The derivative of Eq (2.11) is the 2nd law:

Ficks 2nd $$\frac{dC}{dt} = D\frac{d^2C}{dx^2} \tag{2.11}$$

Solutions for semi-infinite medium

For a semi – infinite medium with a constant start concentration (C_0) and zero initial concentration ($C = 0$ at $t = 0$) throughout the medium the solution is described by Eq. (2.13) with the given boundary and initial conditions (Eq. 2.12):

$C = C_0,\ x = 0,\ t > 1$ (2.12)
$C = 0,\ x > 0,\ t = 0$

$$\frac{C}{C_0} = \frac{1}{2}(1 - erf(\frac{x}{2\sqrt{Dt}})) \tag{2.13}$$

where *erf* is the error function expressed as:

$$erf(z) = \frac{2}{\sqrt{\pi}}\int_0^z \exp^{-\eta^2} d\eta \qquad \text{where} \quad \eta = \frac{z}{2\sqrt{Dt}} \tag{2.14}$$

The solution for the total amount of diffusing substance with time is expressed by Eq. (2.15)

$$M_t = 2C_0\left(\frac{Dt}{\pi}\right)^{\frac{1}{2}} \tag{2.15}$$

Radial diffusion into a cylinder

If a long circular cylinder with in which diffusion is everywhere radial and by putting $x = r \cdot cos\theta$ and $y = r \cdot sin\theta$, the diffusion equation (2.10) can be expressed by Eq. (2.16).

$$\frac{\partial C}{\partial t} = \frac{1}{r}\frac{\partial}{\partial r}(rD\frac{\partial C}{\partial r}) \tag{2.16}$$

In a cylinder with a radius b, with the boundary and initial conditions:

$C = C_0,\ r = b,\ t \geq 0$
$C = 0,\ 0 > r > b,\ t = 0$ (2.17)

the solution is:

$$C = C_0\left[1 - \frac{2}{b}\sum_{n=1}^{\infty}\frac{1}{\alpha_n}\frac{J_0(r\alpha_n)}{J_1(b\alpha_n)}\exp\left(-D\alpha_n^2 t\right)\right] \tag{2.18}$$

where $J_0(x)$ and $J_1(y)$ are the Bessel function of the first kind of order zero and the Bessel function of the first kind of the first order, respectively, and $\alpha_n (n = 1,2,\ldots,\infty)$ are roots of $J_0(a\alpha_n) = 0$.

The solution for the amount of diffusing substance that has entered or left the cylinder with time t, M_t, is given in Eq. (2.19). M_∞ is the quantity after infinite time.

$$\frac{M_t}{M_\infty} = 1 - 4\sum_{n=1}^{\infty}\frac{\exp\left(-D\alpha_n^2 t\right)}{(\alpha_n b)^2} \tag{2.19}$$

The diffusion coefficient can be calculated by Eq. (2.20) where $t_{½}$ is the time to reach half the saturation concentration in a cylinder with a radius r.

$$D \approx \frac{0.063}{t_{1/2}r^2} \tag{2.20}$$

The solution for a hollow cylinder with inner radius a and outer radius b, with the surface $r = a$ maintained at a constant concentration C_1, and $r = b$ at C_2 the amount of diffusing substance entering the region $a \leq r \leq b$ in time t is given by:

$$\frac{M_t}{M_\infty} = 1 - \frac{4}{b^2 - a^2} \sum_{n=1}^{\infty} \frac{J_0(a\alpha_n) - J_0(b\alpha_n)}{\alpha_n^2 \left[J_0(a\alpha_n) + J_0(b\alpha_n) \right]} \exp(-D\alpha_n^2 t) \qquad (2.21)$$

where

Y_0 = Bessel J – function of second kind (Y) of order zero.
α_n = the positive roots of $U_0(\alpha_n) = J_0(r\alpha_n)Y_0(b\alpha_n) - J_0(b\alpha_n)Y_0(r\alpha_n)$

The solution for the hollow cylinder (Eq. 2.21) is based on a constant concentration (for example zero concentration) on the inner surface. This assumption might be wrong as the carbon after infinite time probably is saturated by sodium. When the inner radius (a in Eq. 2.21) approaches zero, the solution is equal to the solid cylinder.

The diffusion coefficient generally depends on concentration, but is for simplicity assumed to be constant in dilute systems.

2.3 Sodium expansion

In 1957 Rapoport and Samoilenko [41] designed an apparatus to measure the sodium expansion during electrolysis. The apparatus was in principle similar to the apparatus used in this work (Chapter 3.7) where the cathodic sample was immersed in a cryolite bath. The sample was electronically insulated from the anodic crucible with a non - conducting disk. When the current was switched on, an expansion of the sample was observed. In some experiments without electrolysis a deformation of the sample was observed. The melt in these experiments consisted of 97.5 % NaF and 2.5 % Al_2O_3. Aluminium metal was added to the melt every 30 minutes resulting in a vigorous reaction (Eq. 2.1). The sodium expansion was not reported in these experiments. Aluminium carbide was reported only to form during electrolysis, or in the presence of aluminium metal in these experiments.

The experimental conditions affecting the magnitude of the sodium expansion is shown in Table 2.2. Several authors have later confirmed the findings of Rapoport and Samoilenko (right column in Table 2.2). In the

Table some other experimental conditions that influence the expansion are also reported.

Table 2.2. Factors affecting sodium expansion in carbon cathode materials.

Experimental condition	**Expansion**	**Reference**
Increasing graphite content or heat treatment temperature	Decreases	41, 42, 43
Increasing pressure	Decreases	34, 41, 43, 44
TiB_2 - coating	Decreases	45
Al_4C_3 – coating	Increases	45
Decreasing temperature	Increases	30, 41
Increasing current density (i)	Increases/ i - dependent	29, 41, 42, 46
Additions to the melt:		
Increasing CR	Increase	41, 46, 47
LiF	Decrease	30, 48
CaF_2	Decrease	41
KF	Increase	30
Increase of Al_2O_3 above saturation	Increase	49, 50

The increasing expansion with decreasing graphitic character of the carbon is as described in Chapter 2.1.2. The melt additions, LiF and CaF_2, decrease the expansion because of a reduced sodium activity [30]. Potassium will (as sodium) penetrate the carbon, and because of the larger size (compared to sodium), a larger expansion results. When a melt is oversaturated with alumina the increase in the expansion is explained with a layer of β - alumina formed on the cathode surface. The migration of Na^+ ions in this layer will be favoured over NaF back diffusion and an enhancement of the sodium concentration at the cathode is the result.

If sodium is directly reduced in carbon (Eq. 2.3), the magnitude of the current will determine the sodium production. If a low current is used, it will take longer time to saturate the sample with sodium and the end concentration will be lower due to reduced NaF surface activity [29, 46].

2.3.1 Effect of pressure

When a pressure is applied on top of the sample before the electrolysis starts, the total expansion is reduced [34, 41, 43, 44]. The reduction of expansion has been explained as a slipping mechanism promoted by the sodium between the graphene layers [51] or local crushing in the weakest parts of the structure [34].

Guilliat and Chandler [51] measured the sodium expansion at different pressures up to 7.4 MPa (Figure 2.10). In some experiments the load was removed or relieved after a given time of electrolysis (Figure 2.11). The elastic strain was subtracted in the graphs. It is seen that after application of a pressure of 6.4 MPa the expansion seems unaffected. Almost the same experiment will be shown in this work but the pressure will not be applied before the sodium expansion has ceased. A probable explanation for the expansion not to decrease might be due to a high sodium expansion rate compared to a small creep rate. If the ratio expansion/creep is large, the creep effect will not be visible. After relieving a pressure of 7.4 MPa the sample expands faster. This will later be explained as creep recovery.

Dewing [34] measured the effect of pressure on sodium expansion in electrocalcined anthracitic cathode samples (Ø 3.8 cm) under pressure. Problems with the apparatus and scatter in the results was reported, but the expansion was fitted to the equation:

$$log\ (expansion) = log\ (expansion\ at\ zero\ stress) - 6.4*10^{-4}\ psi \qquad (2.22)$$

Schreiner and Øye [44] measured sodium expansion under pressure in anthracitic, semigraphitic and semigraphitized cathode materials in samples taken out in two different directions from the commercial cathode block. Approximately the same reduction in expansion at a given pressure was measured in all the studied cathode materials. Application of a pressure of 5 MPa gave approximately 50 % reduction in expansion. The sodium concentration was found to be independent of the applied pressure.

Peyneau [43] used larger samples with a diameter of 6 cm to study the sodium expansion. It took 10 hours for the larger samples to reach saturation A reduced expansion of approximately 50 % was found in materials ranging from anthracitic to graphitic material with a pressure range of 3 MPa (Figure 2.13).

Eq. (2.22) is plotted together with the measurements from the different groups in Figure 2.12 (from [52]). The scatter is rather large, but the pressure clearly reduces the expansion.

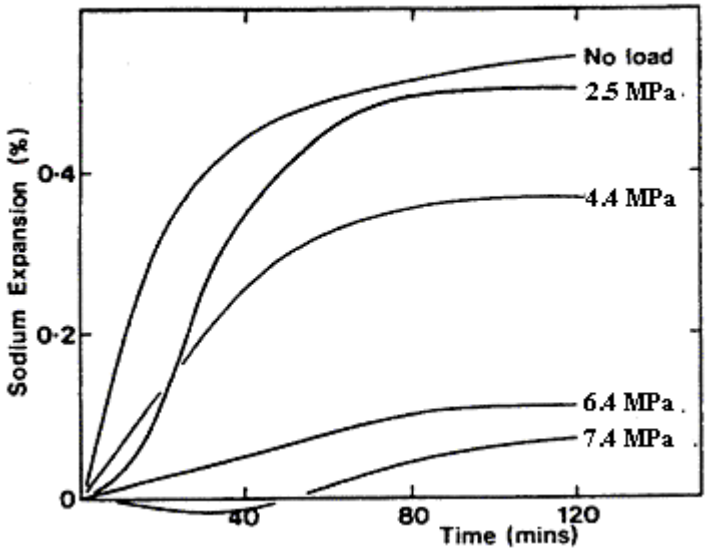

Figure 2.10. Sodium expansion at different pressures [51].

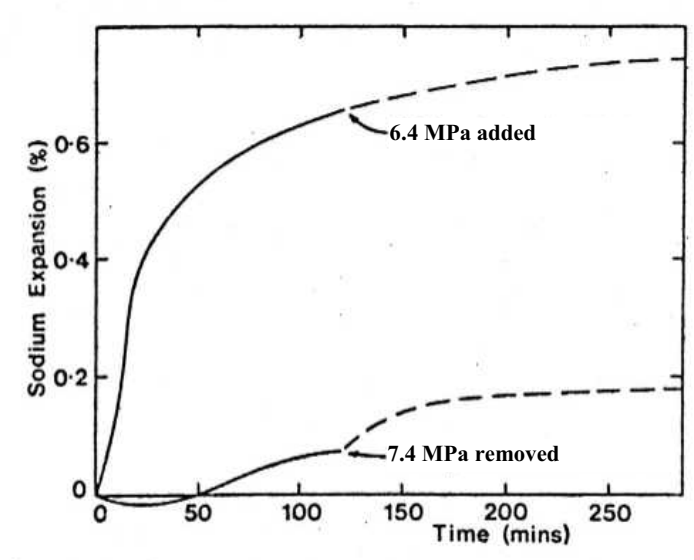

Figure 2.11. Effect of adding or removing a pressure during sodium expansion [51].

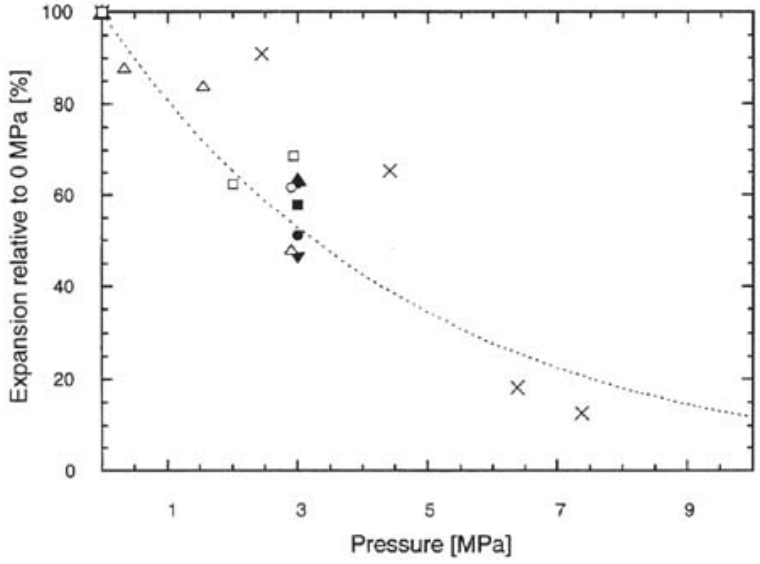

Figure 2.12. Sodium expansion as a function of pressure relative to the expansion achieved without pressure calculated from Schreiner [52]. Open symbols: From Dewing [34] (different shape of the symbols refers to different materials tested). Crosses: From Guilliatt and Chandler [51]. Filled symbols: From Peyneau et al [43]. Broken line: Eq. (2.22) from Dewing [34].

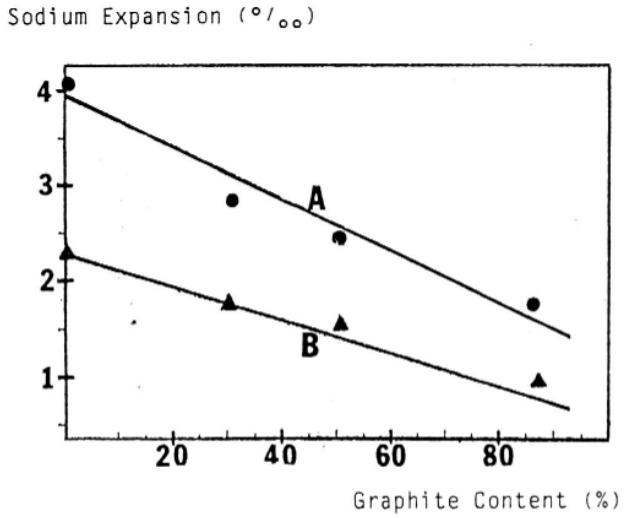

Figure 2.13. Anthracitic samples (ECA), versus graphite content without pressure (A) and with 3 MPa pressure (B) [43].

The stresses in a solid cylinder sample during electrolysis were calculated by Zolochevsky et al. [29] in a semigraphitic material. The total expansion was about 0.5 % in a melt with CR = 4. The calculated stresses approached the crushing strength when a pressure of 2.3 MPa was applied on top of the

sample. As the behaviour of carbon materials could be described as elasto-plastic [53], the formation of cracks does not need to be catastrophic. If a local stress corresponding to the crushing strength appears, the sample can still stand firm. This supports a local crushing explanation. Creep of the carbon will also reduce the stresses as shown in this work. The later reported creep strain can explain some of the scatter between the reported expansion measurements, as the time of the different experiments not was the same.

2.3.2 Effect on strength

In carbon cathode materials, an increase in fracture toughness, E – modulus and strength with increasing temperature is found [53]. This is explained as a healing or closure of microcracks and voids formed during cooling after carbonisation [53, 28].

Dergunov et al. [54] studied tensile strength and ductility in commercial grade graphite with different grain sizes. The graphite was manufactured from petroleum coke and coal tar pitch. Three temperature regions concerning failure were found:

1 Room temperature to 2500 K, brittle fracture. Transgranular failure.
2 2800-3100 K, maximum strength and strain. Mixed failure. This was called the equicohesive temperature, which appears when the strength of the grains is equal to the strength of the boundaries between grains.
3 Above 3100 K, reduction of strength and strain. Intergranular failure.

Patrick and Walker [55] discussed the strength of carbon materials. For high porosity materials the pores are the larger defects and control the critical flaw size. With increasing porosity, the strength of the material decreases. However, in addition to total porosity, the pore size and shape are also of importance. Pores can work both as crack initiators and as crack stoppers. The less round and larger a pore is, the higher stresses will arise in the less round end. Round pores can distribute the stresses over a larger area and work as crack stoppers.

A generalised Griffith model [56] to account for any type of energy dissipation is gained by including the fracture energy. This constant could include plastic, viscoelastic, or viscoplastic effects. When a fracture stress of σ_f is reached in a crack with length $2a$ inside a body with uniform tension stress perpendicular to the crack, the crack will propagate (Eq. 2.23).

$$\sigma_f = \left(\frac{2Ew_f}{\pi \cdot a} \right)^{1/2} \quad (2.23)$$

where

σ_f = Fracture stress
E = Young's modulus
w_f = Fracture energy
a = Half crack length

Patrick [57] found the tensile strength of carbon materials to fit Eq. (2.24) better than Eq. (2.23). The maximum and minimum diameter of the pores gave an impression of the sharpness of the pores and was used to predict coke tensile strength from structural data.

$$\sigma = k(F_{max})^{-0.5} \exp\left[-2 (F_{max}/F_{min})^{0.5} P_y\right] \quad (2.24)$$

where
σ = Tensile strength
F_{max} = Maximum diameter
F_{min} = Minimum diameter
P_y = Fractional volume porosity

In addition to the porosity, the optical texture influences the strength. It has been proposed that cokes of mosaic optical texture exhibit the highest strength as the mosaics of coke are more tightly bonded. The mosaic structure could also easier stop cracks because of the randomly oriented structure. It has also been suggested that the boundaries between optical components in coke can initiate/propagate cracks [55].

Under tensile loading the mechanism of coke failure involves the formation of stable micro cracks, initiated at the larger pores, the number and length of which increase with increasing load. Eventually, a flaw of critical size is formed and propagates uncontrollably through the specimen. The role of the nature of the carbon matrix of the coke in the formation of these microcracks is uncertain but it is clear that the structure of the pore-wall material may also influence the strength of the coke materials.

For cathode materials during electrolysis, before saturation, the sodium expansion causes a strain gradient, with resulting stresses that could be close to the ultimate strength of the material [29]. The crushing [30] and bending

strength [58, 59] is reduced and tend to increase when the sample is saturated by sodium (Figure 2.14). A lower strength decrease was measured with more graphitic material and more acidic melt (smaller sodium expansion). The original strength is probably not reached after saturation as the sample is damaged during electrolysis.

The samples used in bending strength measurements will bend as sodium penetrates the bottom part immersed in the electrolyte [60]. Some of the strength decrease during electrolysis was explained due to bending of the sample and not as a strength decrease in the electrolysed material. The sample did not return to the original shape after electrolysis probably because of the destructive effect of the penetrating sodium.

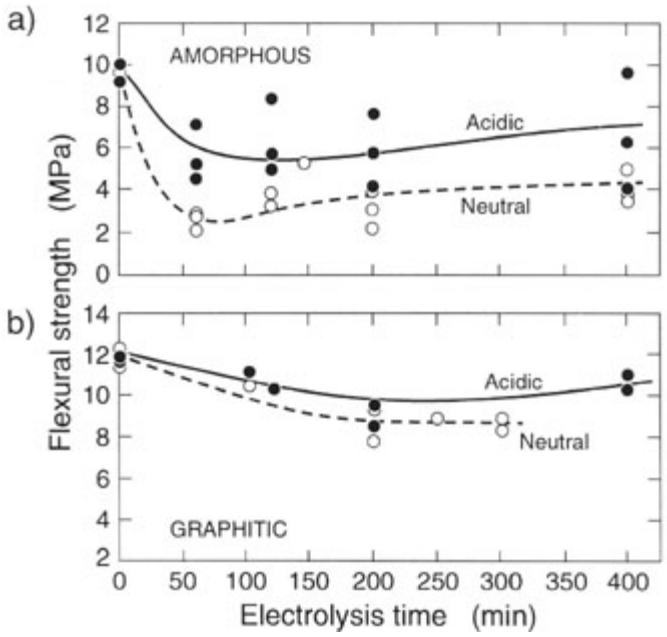

Figure 2.14. Comparing the effect of electrolyte composition on the rate of change in the flexural strength of both amorphous (a) and more graphitic (b) cathode specimen [58].

2.3.3 Sodium expansion models

Asher [16] proposed a model for the sodium expansion based the crystal structure from X-ray measurements in graphite and a petrol coke. The expansion of different graphite's exposed to sodium vapour at 400 °C was measured. The dilation was reported to appear complete at this temperature as no more expansion was observed when the temperature was increased to 440 °C. The dilation ranged from 0.36 % to 1.0 % dependent of graphite and extrusion direction. A petroleum coke heat treated to 2000 °C expanded 2.3 %. By X – ray diffraction measurements NaC_{64} was identified, and the distance increase of the 8th stage unit cell was measured to increase 5 % in the c – direction. (The intercalated sodium layer expanded every 8th graphene layer from 3.35 to 4.5 Å, Figure 2.15).

The proposed model is shown in Figure 2.16. In a specimen of length L, the expansion, e, in the c – direction of each crystal would contribute to an amount of $t \cdot e \cdot \sin\beta/100$ in the X – direction, t being the height of the crystal, and β its inclination to the X-direction. The total percentage dilation of the whole sample was then represented by Eq. (2.25).

$$E(\%) = \sum \frac{t \cdot e(\%) \cdot \sin\beta}{L} = \frac{T}{L} e(\%) \qquad (2.25)$$

Where T is a constant characterising the sample in the measured direction. The model described the measurements well, but Schreiner [52] argued that not all of the carbon consisted of the new compound $C_{64}Na$ as the authors later found parts of graphite in the synthesised material.

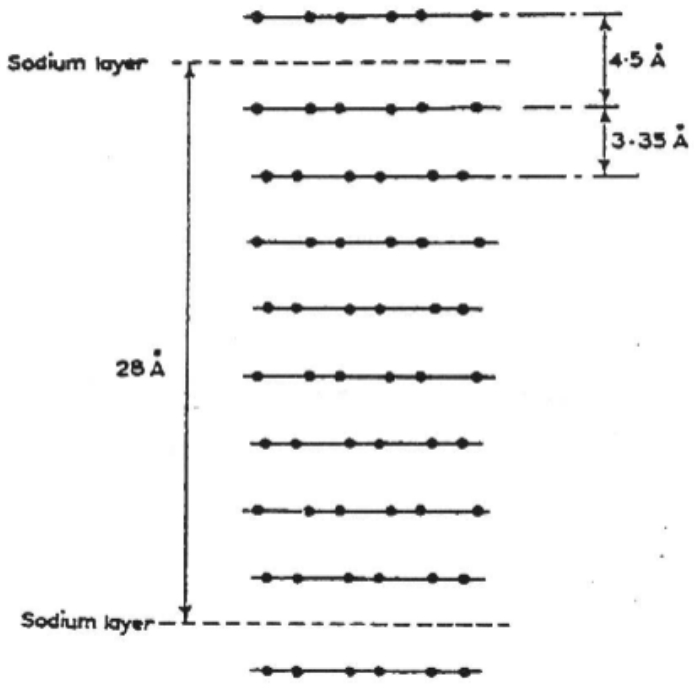

Figure 2.15. Structure of the 8th stage compound NaC_{64} [16].

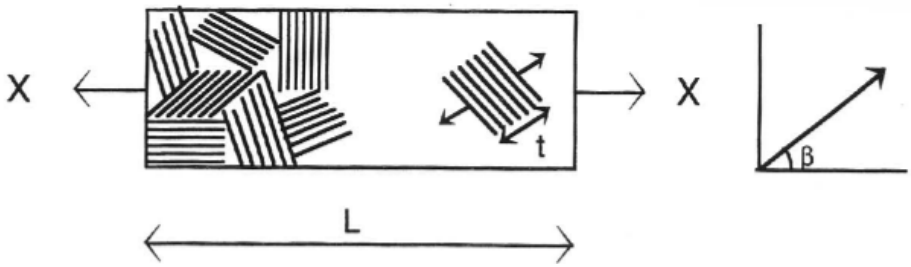

Figure 2.16. The variables in the expansion model of Asher [16].

Slavin and Blyushtein's sodium expansion model [61]

The rate of sodium transport in and out of the carbon was assumed to be proportional to the sodium concentration.

$$K \cdot d\varepsilon/dt = d[Na]_C/dt = K'[Na]_e - K''[Na]_C \quad (2.26)$$

which was integrated to

$$\varepsilon = K \cdot (K'/K'')[Na]_C\,(1 - exp(-K''t)) \quad (2.27)$$

Where ε is the linear expansion of the sample, t the electrolysis time, *K, K'* and *K''* constants, and $[Na]_e$ and $[Na]_C$ are the concentrations of sodium in the electrolyte and carbon, respectively. Further constants based on experience and experiments were introduced to include temperature (T), electrolyte composition, K_{el}, and height of the block (h). The initial dilation was described as:

$$\varepsilon_{in} = \frac{K_{el}}{K_C}\exp\frac{3100}{T}\left[1-\exp\left(-\frac{t}{100h}\exp(\frac{1500}{T}\right)\right] \qquad (2.28)$$

Naas [30] argued that Eq. (2.28) probably was best to consider as purely empirical, but this equation was successfully applied to predict the sodium expansion in operating cells in the former Soviet Union.

Naas [30] measured sodium expansion of cathode materials with different additions of alkalis in the electrolyte and calculated diffusion coefficients in the range $0.4\cdot10^{-5}$ -$1.2\cdot10^{-5}$ cm^2/s. The expansion was assumed to be proportional to the sodium concentration, the same assumption as here, but the expansion - time curve was fitted to the solution of Fick's law for diffusion into a semi – infinite slab, and not radial diffusion which is the case for the Rapoport specimen. A so-called constant effective penetration depth was chosen for x in Eq. (2.29).

$$\varepsilon(x,t) = A'c_{sat}\left(1-erf(\frac{x}{2\sqrt{Dt}})\right) = A'c_{sat}\left(1-erf(k_d)\right) \qquad (2.29)$$

where
D = Diffusion coefficient
t = Time
$A'c_{sat}$ = Constants

It seems more likely that this model predicts the concentration at the given distance x during time. If the expansion data of Naas [30] is studied in detail, the expansion curves look similar to the ones measured in this work.

Zolochevsky et al. [29] also assumed the concentration of sodium to be proportional to the expansion for modelling of Rapoport samples. Fick's 2nd law was used to model the expansion, but the solution for radial penetration into a cylinder was used. This seems more realistic for the immersed Rapoport sample. The solutions used in this paper are also used in this work and are shown in Chapter 2.2.3.

2.4 Creep

Creep is the designation of a time dependent non-elastic deformation, which occurs in many materials within certain ranges of stress and temperature. Creep is a function of strain (ε), stress (σ) and time (t). The material parameters are temperature (T) dependent and the creep rates in general increase with increasing temperature. The creep curve shown in Figure 2.17(a) is common to a large number of materials. The corresponding creep rate ($d\varepsilon/dt$) versus time is shown in Figure 2.17(b). Three periods of time are observed. The periods are called primary, secondary and tertiary creep. The respective creep rate periods are identified with decreasing, constant and increasing creep rate [62].

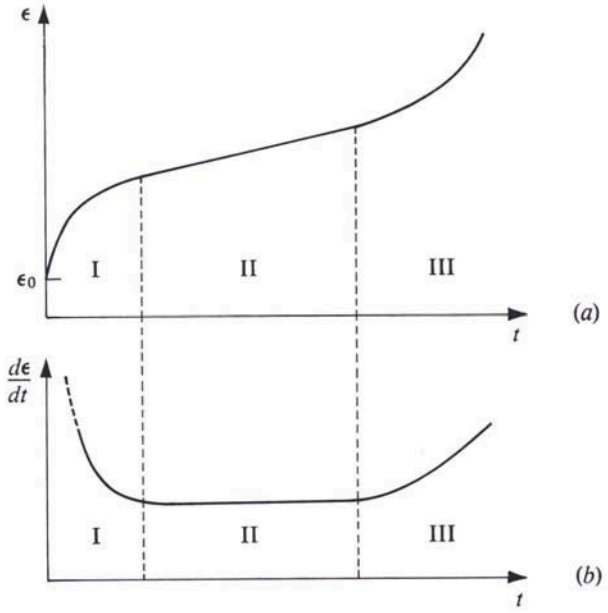

Figure 2.17. Creep and creep rate in a constant stress creep test [62].

A recovery of some of the deformation is observed when a structure is unloaded. If the material is exposed to a constant displacement instead of a constant stress, the stresses will be relaxed with time.

Previous creep measurements in carbon materials are mostly measured in graphite at high temperatures (above 2000 °C) where the application often is in nuclear reactors [54, 63-66]. The creep strain, (total strain - elastic strain, e-e_0), is often described with Eq (2.30) with the constant n typically around 0.5 [63, 66].

$$e\text{-}e_0 = A \cdot t^n \quad (2.30)$$

Dergunov et al. [54] measured the creep in commercial grade graphite with different grain sizes. The graphite was manufactured from petroleum coke and coal tar pitch. Eq. (2.31) was fitted to the creep behaviour.

$$\varepsilon = ke^{b\sigma} \log t + k_c(\sigma/\sigma_0)^n \cdot t \quad (2.31)$$

The creep curves were equal at the first and second loading. The lowest temperature for the creep measurements was 2300 K (2027 °C) and a stress exponent of $n = 2.92$ was measured.

As the materials studied in this work are not exposed to more than 1000 °C and the materials exhibit a structure of a more disordered nature, the creep mechanism is probably not comparable with the reported creep strains in graphite. Also the failure mechanism is different above and below approximately 2200 °C [54].

At high temperature limited plasticity is possible in polycrystalline carbons, and this may have several origins including dislocation motion, grain-boundary sliding. Generally significant plasticity is not observed and the almost universal consequence is that cracks are eventually nucleated at the boundary [55]. This can lead to several phenomena such as changes in shape of individual grains or the sliding of adjacent grains relative to reach other across a boundary.

Another material with some properties similar with carbon cathodes is concrete. This material consists of, like cathode materials, an aggregate and a binder. The concrete material exhibits a similar non-linear stress-strain diagram above ~30 % of critical load (Figure 2.18). This behaviour is explained as micro cracking in the transition zone (zone between aggregate and binder). The material also has shrinkage cracks from the drying process as observed in cathode materials after cooling [3]. The critical strengths are also comparable to carbon, as the compressive strength is several times higher than the tensile strength.

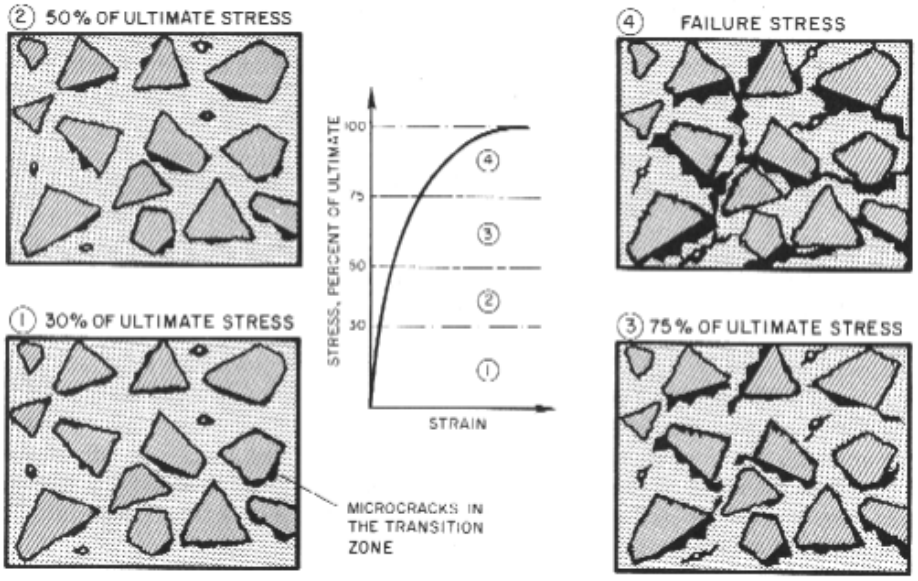

Figure 2.18. Diagrammatic representation of the stress-strain behaviour of concrete under uniaxial compression. [67]

The stress - strain (load - extension) diagram for a carbon cathode material and concrete during loading and unloading are compared in Figure 2.19. It is seen in both diagrams that the curve is different during loading than unloading. The diagram for concrete (Figure 2.19b) is achieved in a compression test, while the diagram for the carbon (Figure 2.19a) is achieved during bending of a cathode sample with a machined notch [53]. These diagrams might not be good for comparison, but as seen from the results during compression in this work (Chapter 4.4) the same behaviour as seen in both diagrams in Figure 2.19 is observed.

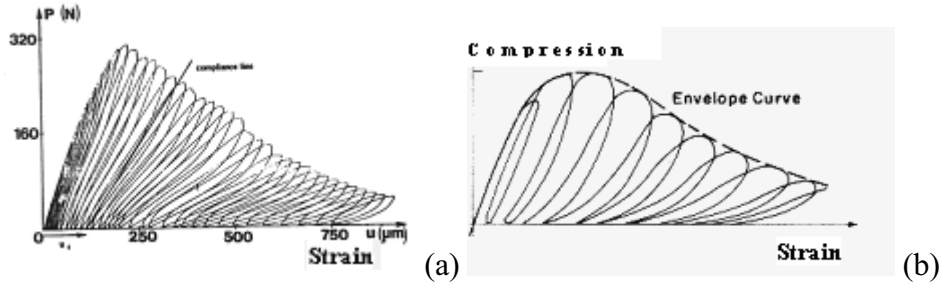

Figure 2.19. Loading – unloading cycles of a carbon sample (a) [53], and uniaxial loading on concrete (b) [67]. Each ellipse describes one loading - unloading operation.

Creep in concrete at room temperature is split into basic and drying creep. The mechanism of the creep not related to drying is not completely

established but is sometimes explained as microcracking in the transition zone (Figure 2.18) [67].

The creep curves of concrete look similar as some plastics, wood and metals, which often can be fitted to viscoelastic models [68]. These models are based on a certain number of elastic springs and dashpot systems (i.e. Maxwell and Kelvin elements, Figure 2.20) put in series or parallel to fit the creep curve. Instead of using this method, Eq. (2.32) has often been found to yield a good description of creep of materials with viscoelastic behaviour at constant stress (similar model as in some graphites, Eq. 2.30).

$$\varepsilon = \varepsilon^{0} + \varepsilon^{+} t^{n} \qquad (2.32)$$

Where ε is total strain, ε^{0} elastic strain and a stress function is included in the constant ε^{+}.

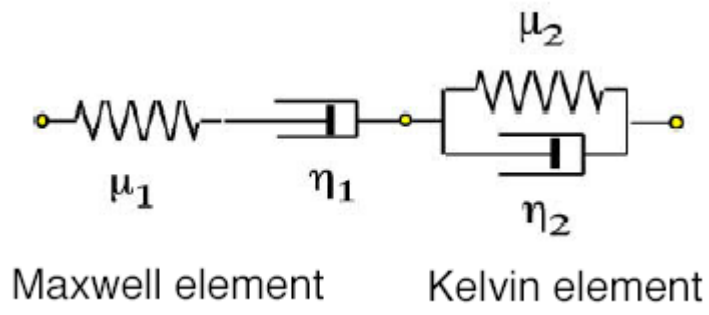

Figure 2.20. Sketch of Maxwell and Kelvin elements in series [68]. μ is the spring stiffness and η the coefficient of viscosity for the dashpot (piston moving in a viscous fluid).

3. Eksperimental

3.1 Materials and chemicals

The studied materials are listed in Table 3.1. Three commercial cathode materials and a laboratory produced material made of petrol coke and coal tar pitch was studied. Grains from a Chinese anthracite mine (analysis in Appendix B) and petrol cokes from different refineries were studied in sodium vapour. Optical microscope images of the different materials are shown in Chapter 4.1. The chemicals used in the experiments are listed in Table 3.2.

Table 3.1. Materials used in the experiments. Procedure of the heat treatment of the laboratory produced materials, anthracite and petrol coke is described in Chapter 3.1.1. Abbreviation: ECA - electrocalcined anthracite (heat treated to approximately 1000 - 2500 °C).

Material	Filler	Binder	Heat treatment	Grain size
Commercial Anthracitic	30 % graphite 70 % ECA	Coal tar pitch	~1200 °C (Block)	
Commercial Semigraphitic	100 % Graphite	Coal tar pitch	~1200 °C (Block)	
Commercial Semigraphitized	100 % Petrol coke	Coal tar pitch	2300-2800 °C (Block)	
Laboratory produced	100 % Petrol coke	Coal tar pitch	1500, 2000 and 2500°C (Block)	0.2 – 0.5 mm
Graphite			~3000 °C	
Petrol coke grains			1500, 2000 and 2500°C	0.8 –1.5 mm
Anthracite grains (analysis in App. C)			1500, 2000 and 2500°C	0.8 –1.5 mm

Table 3.2. Chemicals used in the experiments.

Chemical	*Supplier*	*Grade*
CaF_2	Merck	>97%
AlF_3	Smelter grade	≈10 % Al_2O_3
Na_3AlF_6	Riedel – de Haën	97-98 %
NaF	Merck	>98.5 %
Al_2O_3	Merck	>99.5 %
Na	Fluka Chemica	Purum, in kerosene
NaOH	Panreac	Titrosol 0.1 M
HCl, 32 %	Merck	>99.99 %
Ar	Hydrogas	99.99 %
Melted electrolyte (analysis in appendix C)	R&D Carbon, Switzerland	CR = 3.89 (from analysis) CaF_2 5 % α-Al_2O_3 0.4 % β-Al_2O_3 4.5 %

3.1.1 Procedure for heat treatment of laboratory produced cathode material and grains

The laboratory produced materials in Table 3.1 were heat treated to different temperatures in an induction furnace with graphite elements (ASTRO) controlled with a pycnometer. The height of the crucible was 23 cm, which caused a temperature gradient. The gradient was measured at 1500 °C and 2000 °C with a thermocouple in the centre of the furnace.

At 1500 °C the temperature in the bottom and top was 1309 °C and 1491 °C respectively, giving a temperature gradient of 182 °C. At 2000 °C the temperatures was measured between 1746 °C and 2029 °C, giving a temperature difference of 283 °C. The thermocouple was not designed for the highest heat treatment temperature (2500 °C), but a temperature gradient larger than measured at 2000 °C (ΔT = 283 °C) must be expected.

3.2 X-ray diffraction

The chosen samples were crushed in a ball mill for about 15 seconds. The milling container was made in steel. Approximately 1 gram of the powder was mixed with an internal standard (≈ 5 % silicon) and mounted in a Siemens D5005 diffractometer with CuK_α radiation. The 2θ range was 24° - 29° with a step of 0.015 2θ and a step time of 5 seconds.

3.3 Image analysis

Samples from sodium vapour test and electrolysis experiments were studied in a high–end Leica/Reichert MeF3A metallurgical optical reflecting light microscope. Pictures were captured with a digital 1-chip CCD RBG colour video camera. The images were processed with NIH image software [69] by a Macintosh computer. This equipment captures images automatically and combines them together. The samples exposed to sodium or molten electrolyte were ground and polished without cooling fluid to avoid reaction with water.

Some anthracite grains were studied to quantify the cracks. The analysis procedure is shown in Figure 3.1.

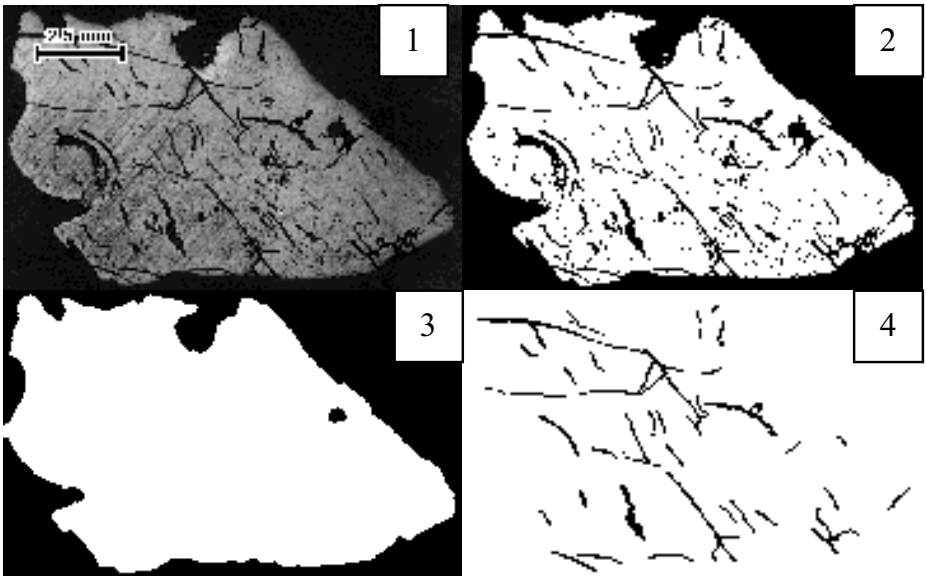

Figure 3.1. The analysing procedure of a grain.

1 The original image.
2 The image was transformed to black and white (binary) and the smallest areas (1-2 pixels) were removed. (One pixel is the smallest area in the picture.)
3 Areas that not were cracks were found (areas outside the grain and large porosity).
4 The black areas (not cracks) from picture 3 were removed from picture 2. The automatic image analysis did not fully give the wanted results and a manual removing of pixels was needed. This was particularly a problem for the sodium exposed grains as sodium reacted with air causing a duller appearance in the microscope.

The network of cracks in picture 4 (Figure 3.1) had to be divided into smaller sections in order to quantify the crack widths. The crack widths were distributed into bins with a crack width of 15 μm. The cutting makes the length a non-relevant parameter and the width vs. area of the cracks is chosen as the parameter for comparison.

3.4 Sodium content analysis

Electrolysed samples were cleaned for frozen electrolyte with SiC sandpaper. The cylindrical samples were cut in circular slices and ground in a steel ball mill. The powder was weighed and left to react with 0.1 M HCl for several weeks in closed glass or plastic bottles. Twenty-five ml samples was titrated against 0.1 M NaOH, logging at least one value for each pH – unit. The titration was performed to above pH = 11.

3.5 Sodium vapour test

The samples were washed in water and dried for at least 8 hours at 100 °C. Sodium metal was cut in small pieces (< 0.15 cm^3) with a scalpel and placed in the bottom of a closed container (Figure 3.2). A four-chamber sample holder held the samples at least 3 cm above the metal. A gold gasket sealed the gap between the steel-lid and steel-container. The device was evacuated and filled with Argon gas three times before leaving an Argon pressure of 100 Torr at 25 °C. The container was heated to 800 °C which was held for two hours. The heating rate was 200 °C/hour. As the top of the container was outside the furnace a reflux of sodium was obtained. After cooling, the pressure was verified to be equal to the start pressure of 100 torr and the samples were treated further in air.

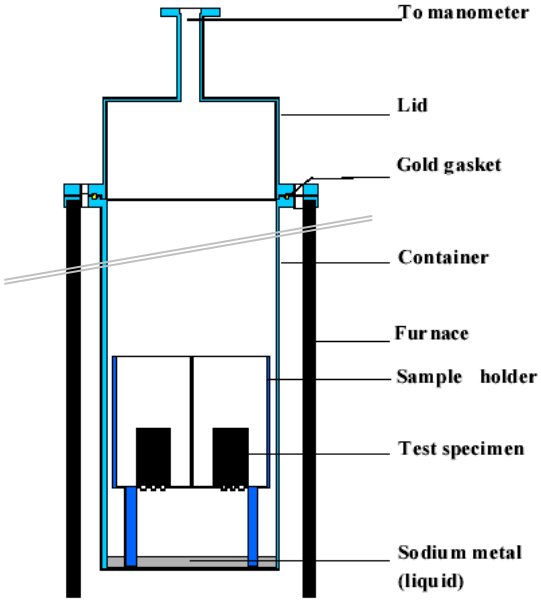

Figure 3.2. Apparatus used for sodium vapour test.

3.6 Sodium expansion

The objective for the first described apparatuses in this chapter (Figure 3.3 and Figure 3.4 a and b) was to measure creep in cathode materials during electrolysis. For several reasons the creep measurements were not reproduced but good sodium expansion measurements were achieved, as the expansion is much larger than the later measured creep (Chapter 3.7). In the process to get good creep data, experimental conditions as current density and sample geometry were changed and sodium expansion data for different experimental conditions were achieved.

The main objective of the apparatuses shown in Figure 3.5 - Figure 3.7 was to quench samples for sodium content analysis. Unfortunately, problems also occurred in most of these analyses but also here sodium expansion results were achieved.

All the apparatuses are modifications of the Rapoport test [41] except the apparatus described in Figure 3.7 where the cathode is located below the electrolyte. The rest of the apparatuses presented in this chapter consist of a cathode sample immersed in a basic cryolitic melt (CR = 3.89) at 980 °C ± 1 °C with a graphite crucible as anode.

3.6.1 Sodium expansion, immersed cathode, solid cylinder

The first apparatus used was made by R&D Carbon, Switzerland (RDC-193). This apparatus is to be standardised for sodium expansion under pressure [70]. A sketch of the apparatus is given in Figure 3.3.

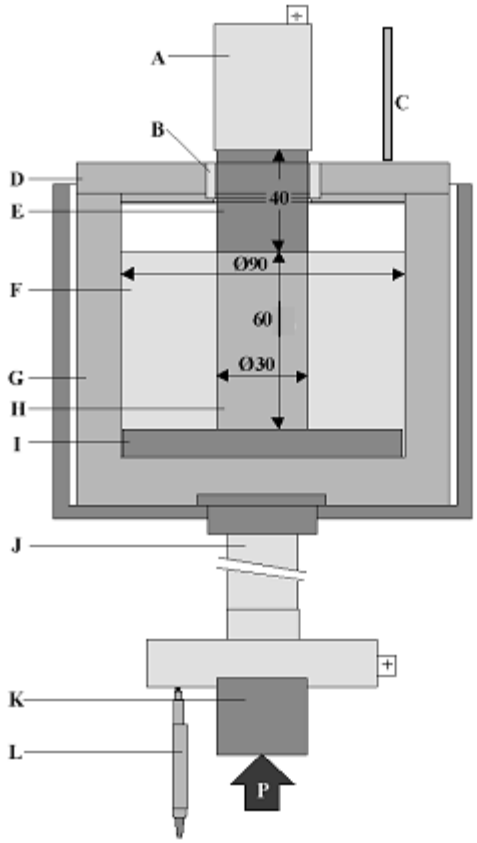

A – Heat resistant steel stop rod
B – Insulating ring
C – Thermocouple (Type K)
D – Graphite lid
E – Graphite cylinder, sample extension
F – Cryolite melt
G – Graphite crucible
H – Sample (Ø30 mm, length 60 mm)
I – Alsint disk
J – Heat resistant steel crucible
K – Hydraulic cylinder
L – Distance measuring unit, (LVD transducer)

Figure 3.3. R&D Carbon apparatus to measure sodium expansion

The sample (H) is electrically insulated from the anodic graphite crucible (G) with an alsint disk (I). A graphite extension (E) rests on top of the sample. A lid (D) with an insulating alsint ring (B) covers the crucible. The load is applied by a hydraulic cylinder (K). A thermocouple (C) on top of the crucible controlled the temperature to 980 ± 1 °C. The electrolysis current is supplied by a DC power supply adjustable to 50 A/12.5V. The

length-measuring device (L, Sylvac ± 0.1 μm) is located below the furnace at 25 °C.

The solid cylindrical sample with a diameter of 30 mm and length of 60 mm (H) was placed on the alsint disk (I) inside the crucible and the graphite extension (Ø 30 mm, length 40 mm) was placed on top of it. The pre-melted bath (CR = 3.89) was poured into the crucible (G) and the lid was put on top with the graphite extension passing through it. The crucible was placed into the steel crucible holder (J) and raised by the hydraulic cylinder (K) until the extension top stopped towards the heat resistant stop rod (A). After approximately two hours of heating and two hours of stabilisation with argon flushing through the furnace, the wanted current was switched on. After the expansion had ceased to a stable value, a pressure of 10 MPa was applied for creep measurements. The signal from the transducer (L) was logged once a minute during the experiments.

The measurements were not reproducible after the pressure of 10 MPa was applied. Some of the problems were attributed to the atmosphere in the furnace as oxidation on the top of the graphite extension was observed. When the load was applied the graphite extension top (with small air corrosion) touching the steel stop was probably weakened and some compression of the partly corroded surface could occur.

The transducer measured the movement of all the equipment above it, not only the movement of the sample. When small distances are measured over several hours, the steel stop rod (A) or the steel crucible holder (J) probably caused some of the disturbances as steel has a certain creep at high temperature.

An unwanted minimum pressure was needed for the hydraulic cylinder to run at a constant pressure. In the beginning of the measuring period the minimum pressure was 1.5 MPa (in the sample) but after some time this pressure increased to 2.3 MPa. Some creep will probably be introduced in the sample by this pressure during sodium expansion, and make another uncertainty.

The alsint disk (I) was also dissolved during long time experiments although the area touching the sample appeared unaffected.

3.6.2 Sodium expansion, immersed cathode, hollow cylinder

The next modifications are shown in Figure 3.4 (a) and (b). The difference between the two set-ups is the loading extension located between the sample and the measuring unit. The measuring device (A) is located on the top of the furnace. The loading piston (F) was required to move independent of the measuring device (E in Figure 3.4a and H in Figure 3.4b). To achieve this, two measuring points were needed on a hollow cylindrical sample (I, $Ø_{inner}$= 7 mm, $Ø_{outer}$= 30 mm) in both set-ups. The centre boron nitride measuring pin (D) touched the bottom boron nitride disk (K) inside the cylinder. In the set-up described in Figure 3.4 (a) the measuring pins (E) went through three machined holes in the piston and touched the sample top. In the modification shown in Figure 3.4 (b) an outer cylinder (H) touched the cylinder periphery with the load piston cylinder (F) inside. The load was in both cases transferred to the sample by a steel frame (C) that was not influenced by the transducer.

Apart from the loading device the principle is the same as described in the previous section. The crucible (L) has a smaller diameter of 76 mm to fit inside the new furnace, and the insulating disk was made of boron nitride (K).

The loading device presented in Figure 3.4b was first tried. The stress in the steel piston (F) was too high and it bent due to creep at higher stresses. The piston was therefore scaled up to get a lower pressure in the piston as shown in Figure 3.4 (a), but also this piston bent after some experiments. Titanium was also tried as this material should have higher resistance to creep, but also this was bent. Graphite was the most promising material, but air corrosion in the top of the furnace was a problem. Graphite would also expand due to sodium and would introduce an extra deviation.

There were also some problems with the measuring pins, as the first steel pins stuck after longer time experiments. Graphite pins eroded in the top and alsint pins solved too fast in the cryolite vapour. An attempt to machine boron nitride pins with this small diameter/length failed.

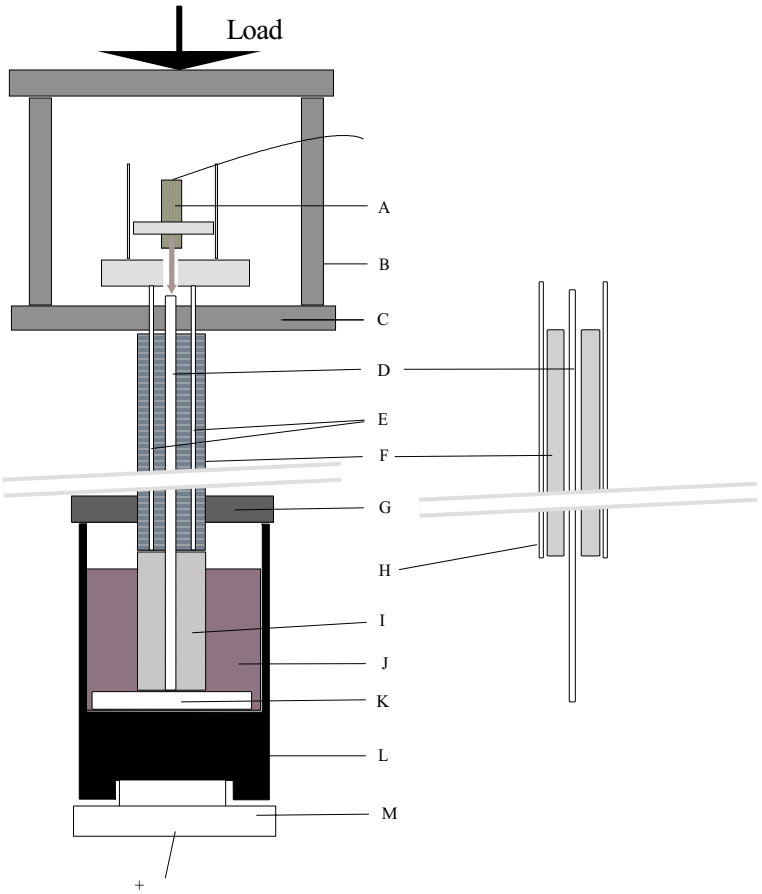

Figure 3.4 a (left) and b (right). Modified arrangement of the Rapoport test. Apparatus used for measurements of hollow cylinder.

A- Distance measuring unit (to computer)
B- Load frame (steel)
C- Load support (steel)
D- Measuring pin (boron nitride)
E- Measuring pins
F- Load piston
G- Graphite lid
H- Cylindrical extension
I – Cathode sample
J – Cryolite bath
K - Sample support (boron nitride)
L - Crucible (graphite)

3.6.3 Sodium expansion, immersed cathode, quenching

The purpose for the apparatus described in Figure 3.5 was to quench samples for later sodium content analysis in addition to measure sodium expansion. The arrangement is simpler than the previous described, as no load was applied in these experiments. The sample extension (B) is screwed into the sample (C) and the expansion is measured with a transducer (A) on top of the furnace. The apparatus made it possible to lift the sample out of the bath and cool it rapidly under the top lid of the furnace. The temperature under the lid in the furnace was approximately 500 °C.

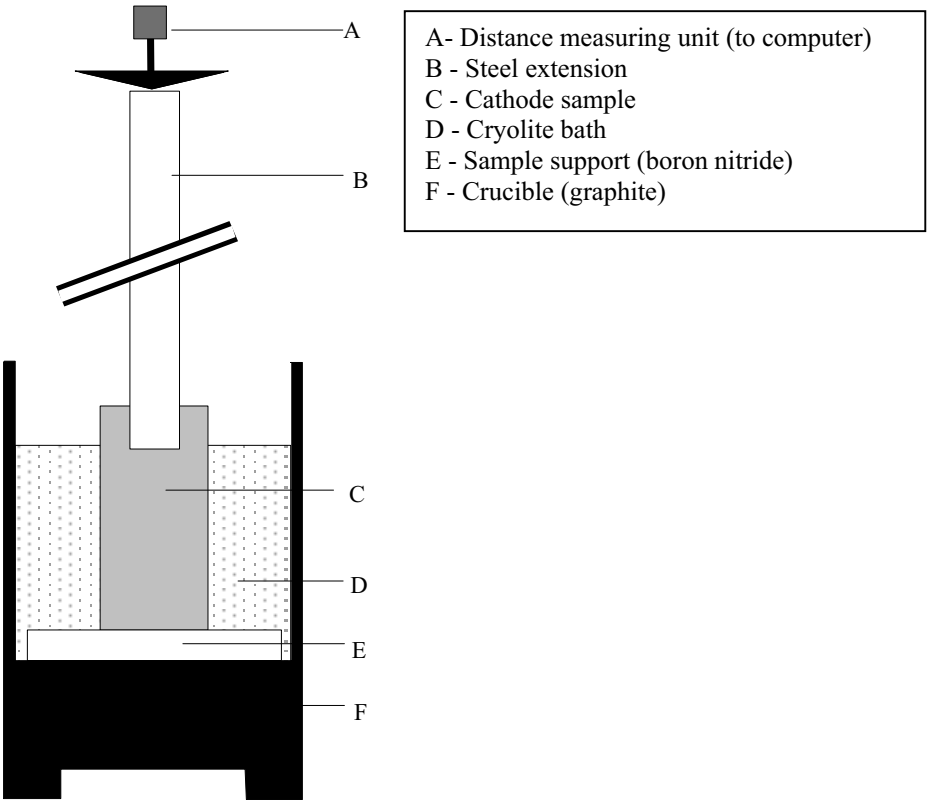

Figure 3.5. Apparatus used for quenching and sodium expansion.

3.6.4 Sodium expansion, cathode above electrolyte

To introduce a sodium gradient to the samples for later sodium concentration analysis the apparatus shown in Figure 3.6 was used. In addition to prepare samples for sodium concentration measurements, the sodium expansion was measured.

The principle was similar as described before expect for the position of the solid cylindrical sample (Ø30 mm, length 60 mm). The sample (C) rested on a machined alsint support (E) that only allowed the bottom part of the sample to touch the melt (D). The alsint support looked like an upside down stool, letting 4 spots touch the sample. After heating and stabilisation a current of 5 A was applied, giving a cathodic current density between 0.4 and 0.5 A/cm^2. The expansion was logged once a minute with a computer connected to the LVD transducer (A). The graphite crucible (E) held the melt and worked as the anode.

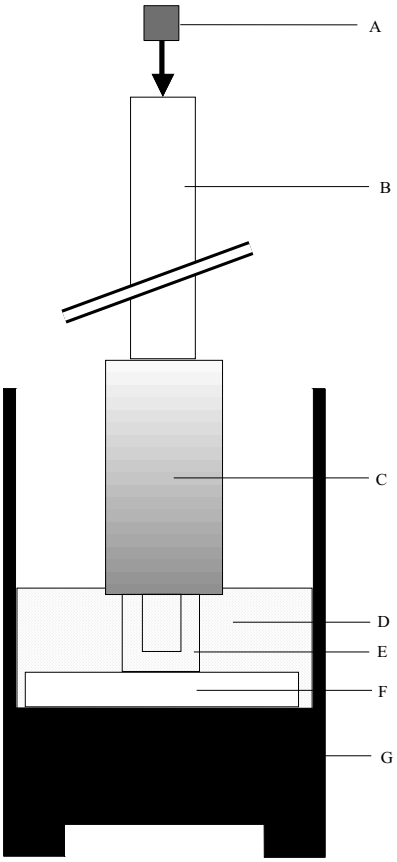

A – LVD transducer
B – Steel tube extension
C – Sample (Ø30, length 60 mm)
D – Cryolite melt
E – Alsint support
F – Alsint disk
G – Graphite crucible

Figure 3.6. Experimental set-up for the cathode located above the electrolyte.

The samples were electrolysed for 2 hours. After electrolysis some samples were cooled down in the furnace and some were cooled down more rapidly by rising the sample up in the top of the furnace (500 °C). The samples were further treated in air.

The first experiments with the principle described in Figure 3.6 were performed in the furnace shown in Figure 3.3. A minimum hydraulic pressure was needed to hold the apparatus together which resulted in a relative high pressure of 5.3 MPa on the supporters touching the sample.

3.6.5 Sodium expansion, cathode under electrolyte

The experiments with the cathode located under the electrolyte were performed in the apparatus shown in Figure 3.3. The difference in the set-up is shown in Figure 3.7. The sample length and diameter was 50 mm. The current density was 0.7 A/cm^2. The minimum pressure from the pressure rod (2.3 MPa) corresponds to a pressure of 2.1 MPa on the outer upper periphery of the sample touching the alsint cylinder. The samples were electrolysed for a given time and cooled down in the furnace. The bath constituents were ground off the surface and the sample was cut in several slices. Each slice was cut into one outer part (Ø27-Ø50 mm) and one inner part (Ø25 mm). The samples were analysed for sodium as described in Chapter 3.4.

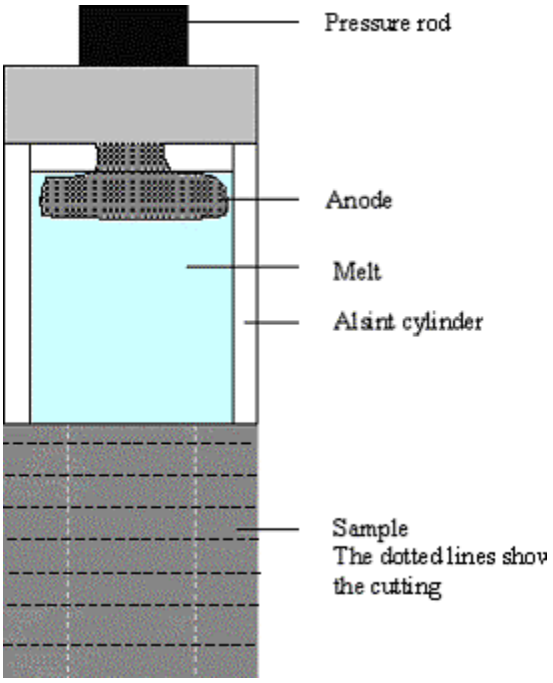

Figure 3.7. Experimental set-up for experiments with the cathode located under the melt.

Cracks and air corrosion in the graphite anode was observed after cooling. This led to poor sodium expansion measurements, but a few sodium content measurements were accepted.

3.7 Creep test

The modified apparatus giving reproducible creep results is shown in Figure 3.8. The purpose of the apparatus was to separate the loading parts (B, C and D) from the extension pins (E) to avoid measuring creep from the steel parts of the apparatus. The wanted load was applied through the loading frame (B) and transferred to the sample (F) through the loading piston (D). Three holes were machined through the loading piston for the measuring extension pins (E) to move independent of the load.

The temperature was either controlled with a thermocouple in the crucible or with a thermocouple located below the crucible (I). When 980 °C was reached the arrangement was left to stabilise for at least 2 hours. At this point the sample was both electrolysed and re-stabilised (creep in electrolysed material), or the creep measurements were started without electrolysis (creep in virgin sample). The strain was logged once a second or once a minute using Excel™. The load was logged at faster intervals using the software for the press. The load was applied using a Lloyd 100 kN – press, fitted with a 100 kN load cell.

The temperature gradient across the sample was from 978 °C to 986 °C with the maximum temperature in the middle of the sample. The temperature below the crucible varied with less than one degree during the experiments. The temperature was also logged outside the alsint tube surrounding the set-up. This temperature varied with less than one degree without electrolysis, and less than 2 degrees in electrolysis experiments. The larger variations for the electrolysis experiments were probably due to the voltage variations during electrolysis. The voltage increased about 0.5 V during one experiment.

The resolution of the length-measuring device is 0.1 μm which in the 60 mm long samples correspond to a strain of $1.6 \cdot 10^{-6}$. This strain is only a fraction of the measured disturbances, so the relatively small noise presented in the result is contributed from other parts of the apparatus, like small unbalances in the measuring sticks and at 980 °C vibrations from the heating element in the furnace.

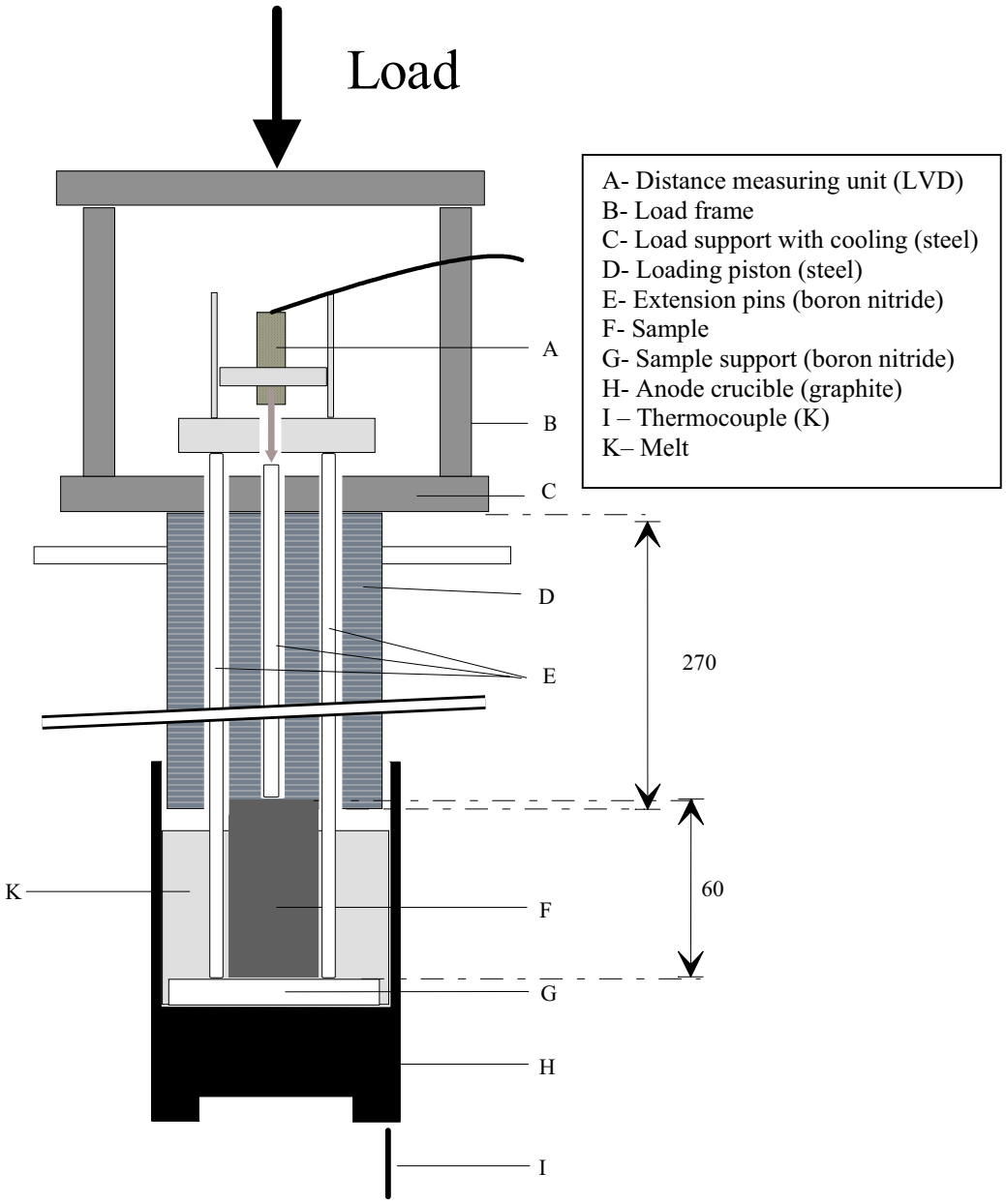

Figure 3.8. Cross section of apparatus used for creep measurements.

The loading procedure was as follows. The wanted pressure was applied for one hour before releasing the pressure for half an hour. The pressure was increased with 5 MPa after each unloading. The reason for the loading-unloading procedure was to assure that the measuring pins (E) were moving independent of the loading piston, and to achieve data for several pressures in one experiment.

An example of the measured strain in a complete electrolysis experiment is given in Figure 3.9. In the experiments without electrolysis the strain looks similar, but without the sodium expansion in the beginning.

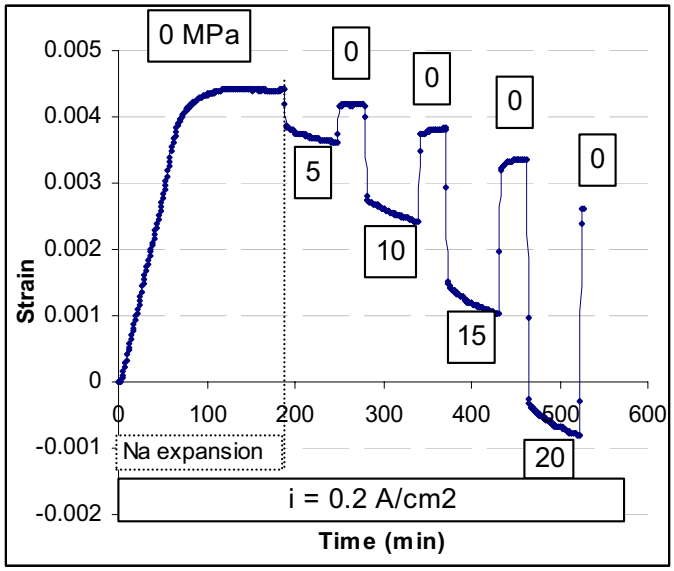

Figure 3.9. Relative strain versus time in an experiment with electrolysis (semigraphitic material). The different operations during an experiment are shown in the text boxes.

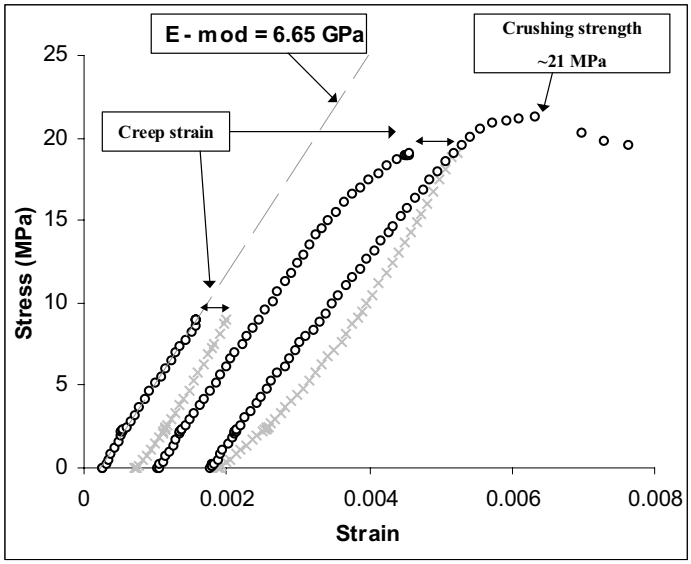

Figure 3.10. A typical stress-strain diagram during one experiment for 10 MPa and 20 MPa (semigraphitic during electrolysis). The darker symbols represent loading and the lighter unloading. The loading at 5 and 15 MPa are not shown to make the Figure clearer.

A typical stress - strain diagram from the loading – unloading procedure is shown in Figure 3.10. The unloading curves (light grey crosses) returns with a different shape than the loading curves (darker circles). The difference in strain between the top of the loading-curve and the top of the unloading-curve represent the creep strain.

The sample is shorter after the applied pressure is released (because of creep). The length reduction is seen as the difference in strain before and after a loading.

The range of the load-cell was large compared to the smaller loads used in the study. The smallest pressure of 5 MPa corresponds to a load of 3.5 kN. It is recommended that the load should be kept above 10 % of the load-cell limit (10 kN).

After the load was removed the load cell readings should return to zero. Unfortunately, the load cell sometimes returned to a value of 0.79 kN or approximately 1 MPa pressure when no load was applied (Figure 3.12) despite stable load readings from the load – cell within ± 0.1 MPa (Figure 3.11). When this happened the load cell always returned to the same value, 1 MPa, and the error was therefore only disturbing the first load in the programmed loading sequence (Figure 3.12). On the subsequent loading the load cell worked satisfactory with a few exceptions mentioned later. The error was recognised when the pressure increased from approximately 1.5 to 3 MPa in 0.05 seconds, when this time normally should have been above 5 seconds (Figure 3.13).

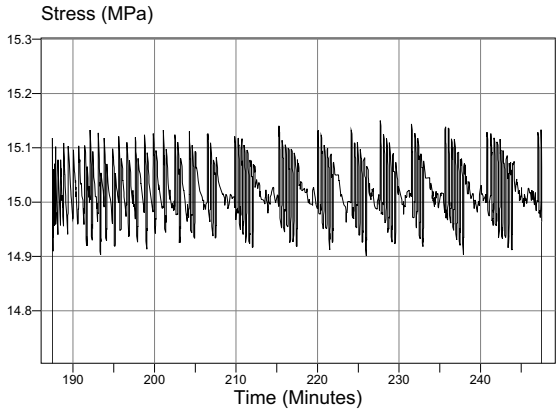

Figure 3.11. Example of variation of stress at a loading at 15 MPa. The variation is approximately ± 0.1 MPa.

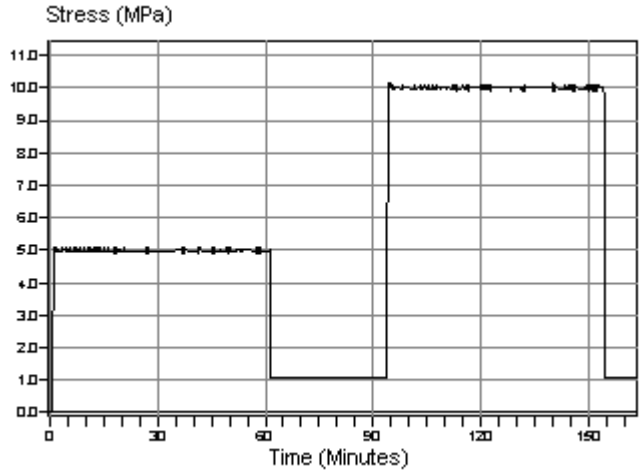

Figure 3.12. Stress vs time readings from the load cell. The stress does not return to zero after the first pressure to 5 MPa. After the subsequent pressure, 10 MPa, the load – cell returns to 1 MPa, the same value as before the pressure of 10 MPa.

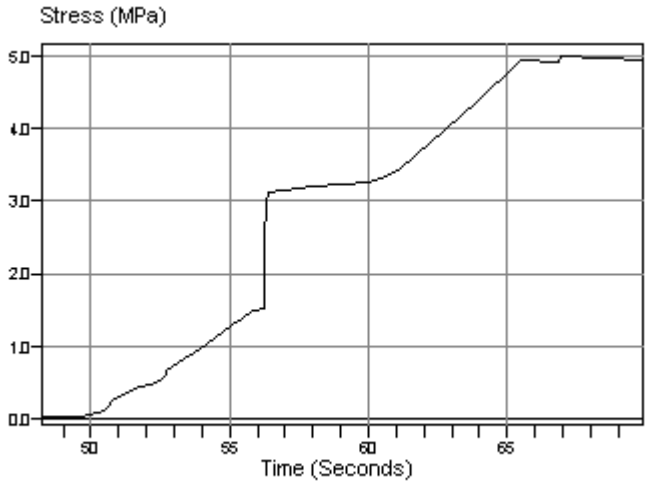

Figure 3.13. Stress vs time reading in a loading to 5 Mpa. The rapid increase in pressure from 1.5 to 3 MPa pressure at 56 seconds are wrong and probably caused an unstable pressure.

The load was applied with a speed of 1 mm/min, and around 3-5 seconds (dependent of the stiffness of the sample) was needed increase the pressure with 1 MPa (Figure 3.13). At higher loads the pressure will increase with a

lower speed, as the stress-strain diagrams are non-linear. A difference in pressure of 1 MPa would give an elastic strain of $1.3 \cdot 10^{-4}$ - $2.5 \cdot 10^{-4}$ (dependent on E- modulus).

The instability of the load cell seemed to be introduced during loading, but it is also possible that the pressure is not constant after the load is applied, despite the stable load – readings. It is only in the first loading of 5 MPa in some experiments the error was observed, in addition to one loading to 15 MPa. Of the total number of creep curves this only correspond to approximately 10 % of the measurements. The experiments with unstable loading are listed below and are mentioned in each case in the results.

Anthracitic electrolysis, parallel I,	5 MPa
Semigraphitic virgin, parallel I,	5 MPa and 15 MPa
Semigraphitic electrolysis, parallel I,	5 MPa
Semigraphitic electrolysis, parallel II,	5 MPa
Semigraphitized virgin, parallel I,	5 MPa
Semigraphitized electrolysis, parallel I,	5 MPa

All experiments are performed two times. If two parallels with stable loading are compared with two parallels where one loading is unstable, the experiments with the unstable load do not need to be more scattered. The reason for this is probably the non homogenous nature of the materials.

The strain and the stress were logged on two different equipments and put together manually. A perfect loading is not possible to achieve, as the load then has to be applied instantaneously. At the exact time when the wanted load is reached, the measured strain goes from elastic strain to creep strain. This time depends on the sensitivity of the measuring device and is here restricted by the logging frequency of the strain, which was once a second. Some of the creep strain occurring between zero to one second after a stable pressure was observed will be lost. The later presented creep strains are in other words minimum values.

In some experiments the time was extended. In these cases the described loading sequence was followed (Figure 3.9) but after application of the last pressure (often 20 MPa) the load was held for about 18 hours and the creep recovery was measured for at least 6 hours. In some experiments only one load was applied to study if the loading sequence had an effect on the creep and the stress-strain diagram.

3.7.1 Creep test, blank run

Although most of the measured strain was related to compression of the sample, the boron nitride support below the carbon sample would yield. The strain of the disk was measured in a blank test by substituting the solid cylindrical sample with a carbon hollow cylinder. In these experiments all 4 rods (3 around and 1 in the middle) rested on top of the boron nitride disk, as the middle rod passed through the hollow sample. When the hollow cylinder was loaded it pushed down the boron nitride disk as in an experiment, and the movement of the middle part relative to the part outside the sample periphery, was measured. The experiments were performed at room temperature with a load corresponding to 20 MPa on the studied samples (solid Ø30 mm). The elastic strain of the disk is compared with the stress - strain behaviour of the anthracitic material in Figure 3.14.

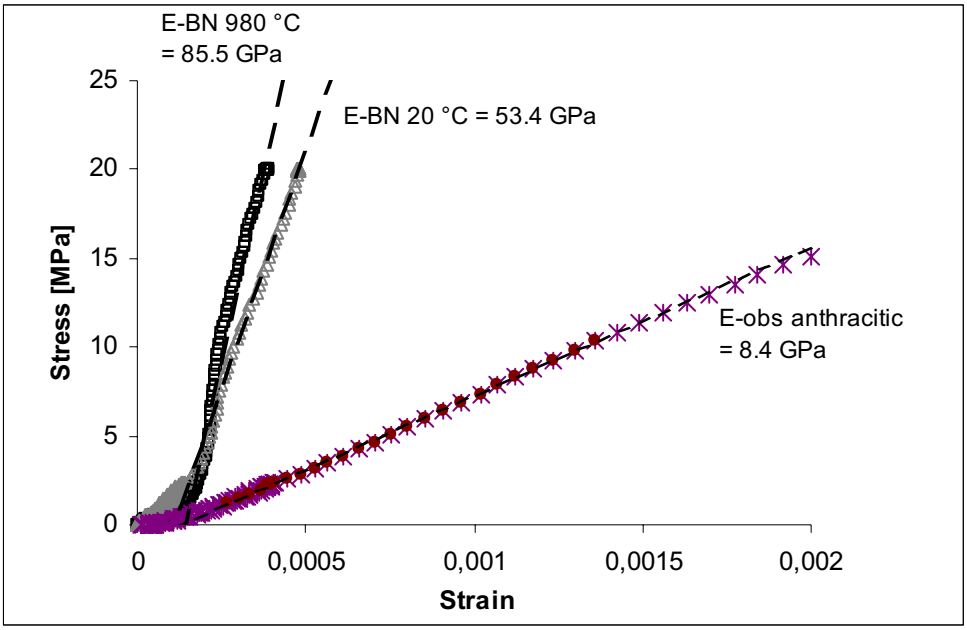

Figure 3.14. Stress – strain diagram for blank tests.

The disk is relatively elastic up to approximately 2.5 MPa (Figure 3.14) and strains below 2.5 MPa presented in the later stress - strain diagrams should be disregarded. The later presented diagrams show the correct shape above 2.5 MPa, as the disk behaves approximately linear above 2.5 MPa pressure, both at 25 °C and 980 °C, but the absolute strain at each stress is too high. To calculate the true modulus of the carbon samples the strain of the disk (at each stress) must be subtracted from the measured total strain (strain in sample and disk together). The true E – modulus can be calculated from the

E – modulus of the disk at 20 °C and 980 °C (53.87 GPa at 20 °C and 85.5 at 980 °C) by Eq. (3.1) and Eq. (3.2) respectively).

$$E_{25°C} = \frac{E_a \cdot E_{obs}}{E_a - E_{obs}} \approx \frac{53.87 \cdot E_{obs}}{53.87 - E_{obs}} \tag{3.1}$$

$$E_{980°C} \approx \frac{85.5 \cdot E_{obs}}{85.5 - E_{obs}} \tag{3.2}$$

where
E – true modulus
E_a – modulus of apparatus
E_{obs} – measured E modulus

The measured E – modulus will deviate more with increasing E – modulus. The E – modulus in this work was measured between approximately 4 GPa and 9 GPa and is in these two extreme cases 4.7 % and 16.7 % larger than observed respectively (at 25 °C, Eq. 3.1). The presented stress – strain diagrams are presented with the measured points (not corrected), as the materials are discussed relative to each other with respect to the shape of the curves. The appearance of a correct curve would be shifted a little higher in the stress – strain diagram above 2.5 MPa.

The creep of the boron nitride (BN) disk was also measured in the blank experiments. The lowest creep measured, the anthracitic material at 25 °C, is plotted together with the creep of the BN disk at 25 °C in Figure 3.15. In this worst case where the creep of the BN disk influences the most, the disk causes approximately 1/3 of the creep in the anthracitic sample.

After the load cell is moved above the loading rig the sample is free to expand and the creep recovery is measured. The creep recovery of the disk is in the same range as in the anthracitic sample (disk included), indicating that the anthracitic sample has no creep recovery at 25 °C. The later presented creep curves are not corrected for the creep of the disk, but in the experiments at 980 °C the measured creep is at least 10 times larger than the creep of the BN disk.

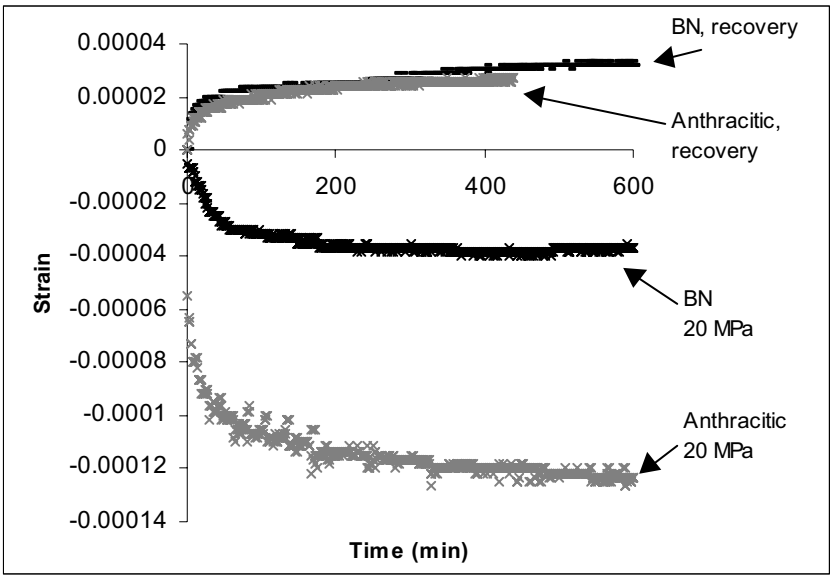

Figure 3.15. Comparison of creep of the boron nitride disk and anthracitic material at 25 °C with a pressure of 20 MPa.

In the creep experiment of the BN – disk at 980 °C the alumina measuring rods dissolved in cryolite and disturbances were measured. But the measurement is anyway shown in Figure 3.16 to show that the creep is small and possibly the same as at 25 °C.

If the creep of the semigraphitized material at 25 °C and 980 °C is the same (Figure 3.16) at these temperatures, the creep of the BN – disk is independent of temperature in this range. The assumption might seem somewhat gross, but graphite and boron nitride have the same crystal structure and is not expected to creep at temperatures as low as 20 °C - 980 °C (as other ceramics [27]). The semigraphitized material is the most graphitic and homogenous of the studied materials, and an approximately equal creep at 25 °C and 980 °C is not unthinkable. The creep measurements at high temperature will be shown to exhibit much larger creep than reported here.

The creep of the semigraphitized material is 5-7 times larger than the BN – disk at 25 °C. The creep of the semigraphitized material is the smallest of all the measured creep data at 980 °C, and it is seen that the difference between the parallels are larger than the total creep in the boron nitride disk (Figure 3.15).

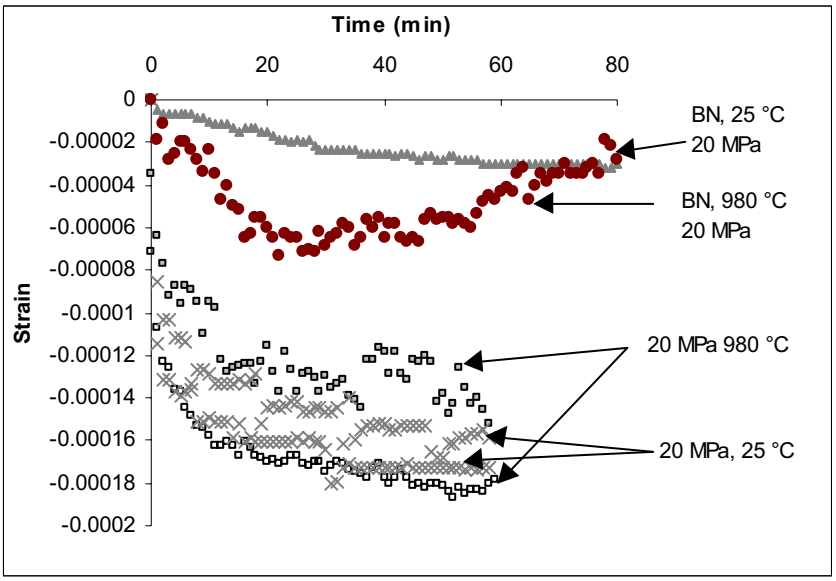

Figure 3.16. Comparison of creep in semigraphitized material at 25 °C and 980 °C (2 parallels at each experiment). The creep of the boron nitride disk is shown at 25 and 980 °C in the top of the diagram.

4. Results and discussion

4.1 Structure study

The different carbons were exposed to sodium vapour at 800 °C. Pictures of the surface were captured by an optical microscope before and after the test. After the test a second polishing of the surface was needed to get good reflection in the microscope, but as sodium is reactive to air, the short time between the polishing machine and the microscope caused a more dull appearance on the pictures after the test. As the sample is polished for a second time, the new surface is a little deeper in the structure. But as seen from the pictures, the surfaces are comparable.

4.1.1 Anthracite grains

Around 50 green anthracite grains (grains without heat treatment) were heat-treated to 1500 °C, 2000 °C and 2500 °C and compared before and after sodium exposure. All anthracite grains crack somewhat after sodium exposure. The cracking is largest in green grains as shown in Figure 4.1. These grains were usually too disintegrated for further handling after sodium exposure. Some of the cracks after the experiments are probably heat treatment cracks as the experiments are performed at 800 °C. This is seen as the unreacted grain calcined to 1500 °C in Figure 4.2 (a) has more cracks than the unreacted green grain in Figure 4.1 (a).

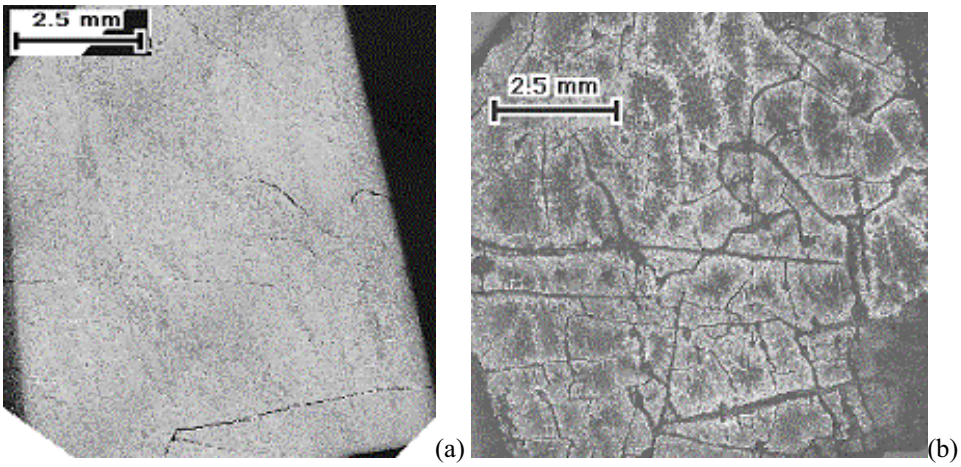

(a) (b)

Figure 4.1. Green anthracite before (a) and after (b) sodium vapour.

The grains calcined to 1500 °C (Figure 4.2) crack more than grains calcined to 2000 °C and 2500 °C (Figure 4.3 and Figure 4.4 respectively). The degree of cracking is less pronounced in the grains heat-treated to 2000 °C and 2500 °C.

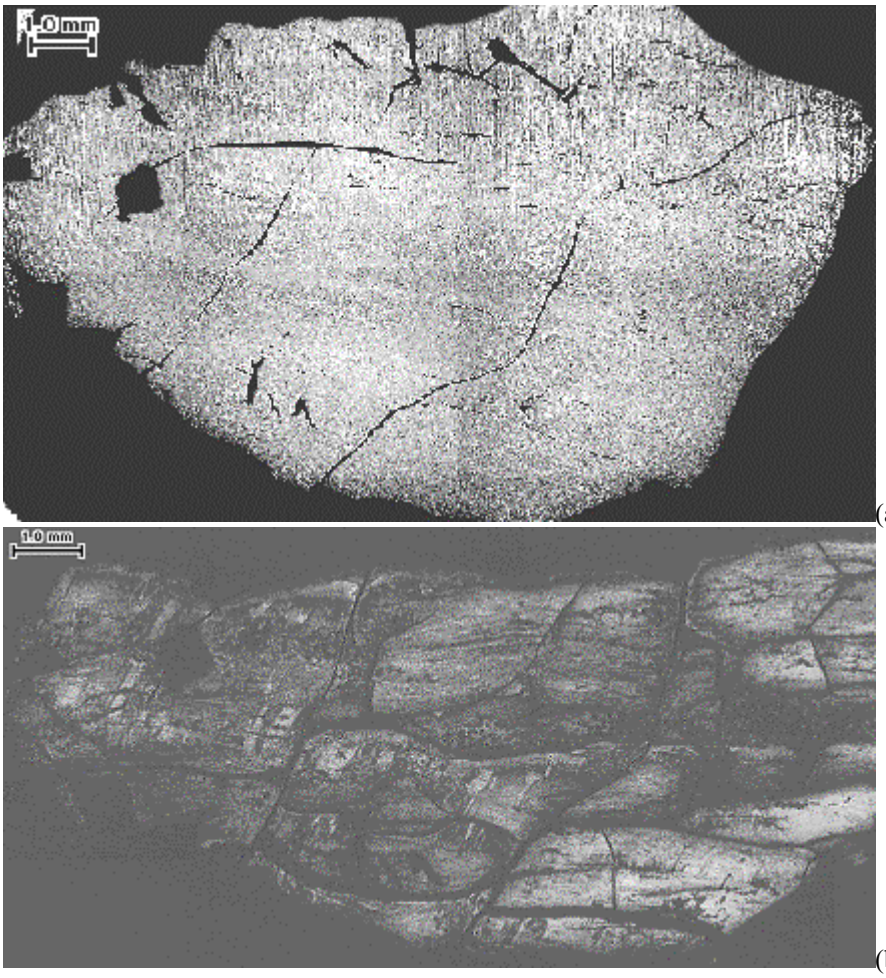

(a)

(b)

Figure 4.2. An anthracite grains calcined to 1500 °C before (a) and after (b) sodium vapour.

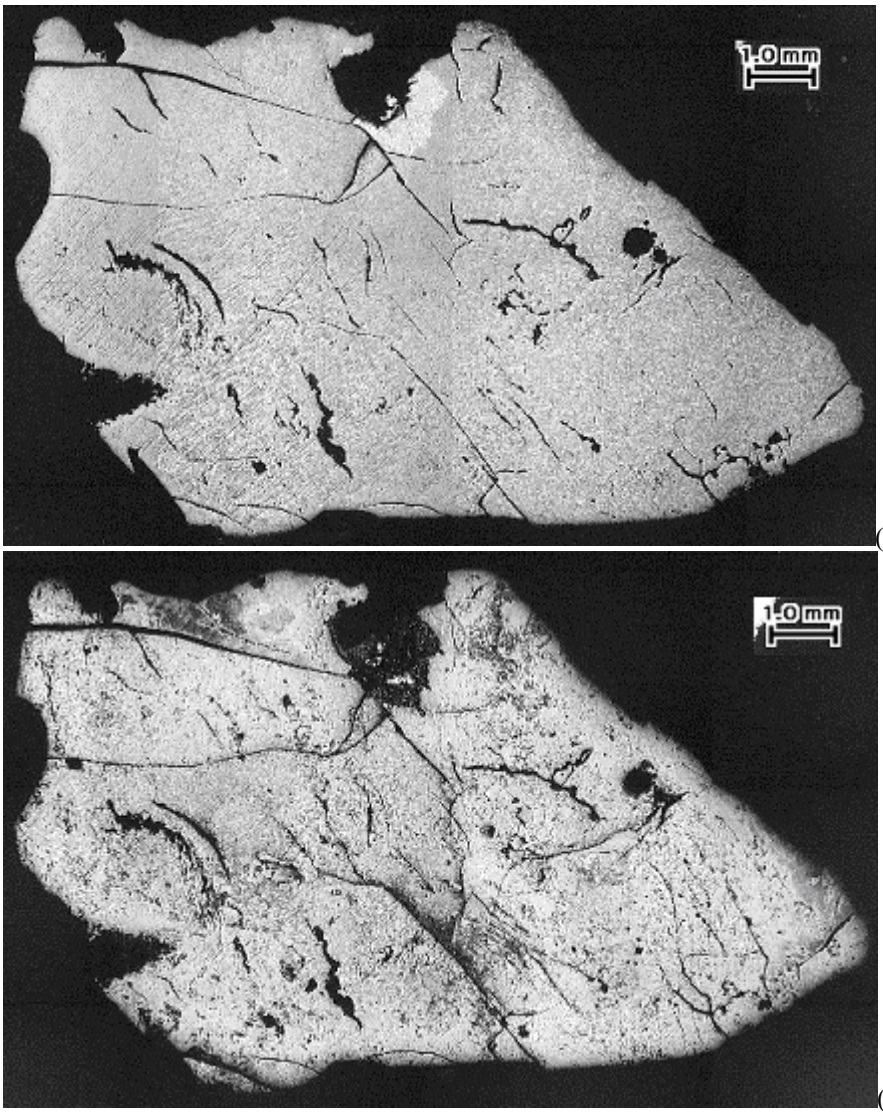

Figure 4.3. An anthracite grain heat treated to 2000 °C before (a) and after (b) sodium vapour.

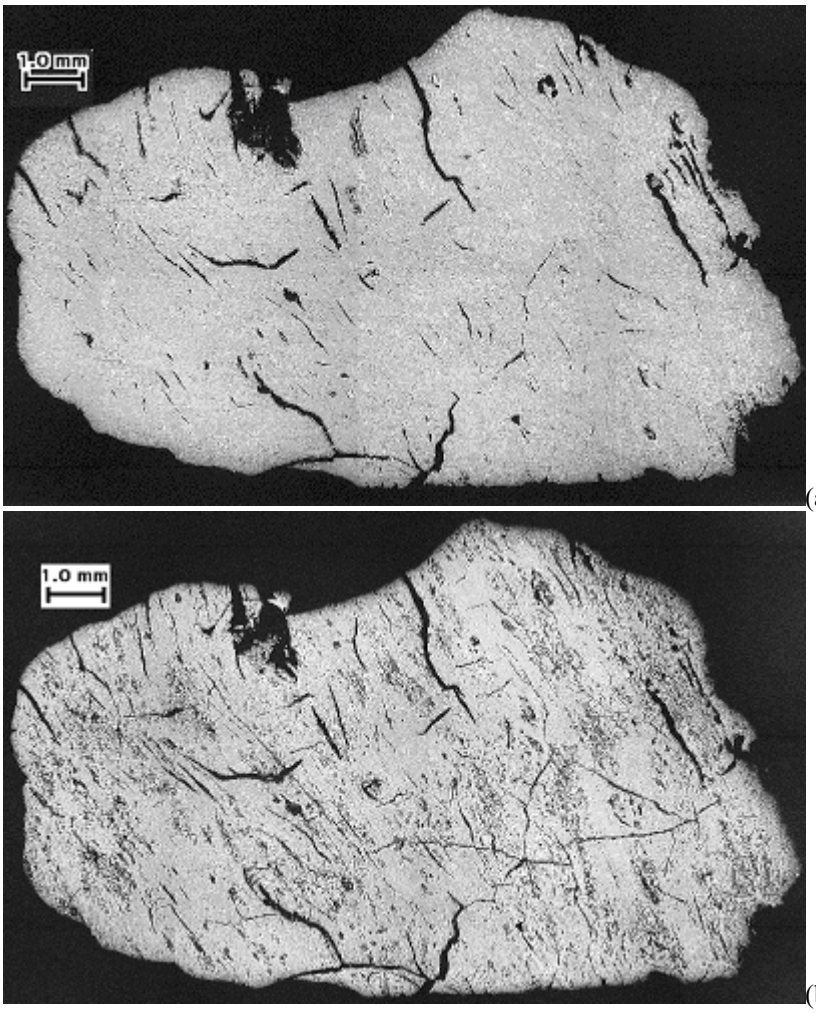

Figure 4.4. An anthracite grain heat treated to 2500 °C before (a) and after (b) sodium vapour.

Quantifying of cracks

The cracks in two grains for each heat treatment temperature were quantified by the use of image analysis before and after sodium exposure. A computer program as described in Chapter 3 handled the digital pictures of the grains. A comparison of total crack area and percent crack increase before and after sodium exposure is shown in Figure 4.6. The crack distributions are compared in Figure 4.5. It is seem that new cracks appear, both small and large, and some of the original cracks grow wider.

The resolution in the images determines the smallest crack width. As one pixel has a size of 15 x 15 μm, the smallest analysed crack width is wider than 15 μm. This smallest pixel size is the same for all the grains except for grain 1 calcined to 2000 °C before sodium exposure, where one pixel is 7.5 x 7.5 μm.

A small total crack area will be more influenced by uncertainty. The sample heat treated to 2500 °C, grain 1, has small crack areas and the uncertainty can explain the rather large percent crack increase (Figure 4.6). The original cracks grow wider. This is seen as the negative values in the crack differences (Figure 4.5) where the original crack widths disappear and the total crack area above this width increase.

The final correction of the images before the cracks were quantified was performed manually on each grain. This involved a subjective evaluation of what was considered as a crack. This was hardest for 2500 °C grain no. 2 where many small and short cracks/pores were discovered before and after sodium exposure and some of the accepted cracks might be more pores and the reported crack-values might be somewhat high.

The cracks are wider (up to ~180 μm) after the sodium exposure test (Figure 4.1 to Figure 4.4) than observed after electrolysis (~ 60 μm (Figure 4.10)). The pressure the binder phase exerts on the anthracite grains could explain the difference. The grains do not have the same possibility to expand freely and the cracks will be forced together. The activity of sodium is also higher in the sodium vapour test (Chapter 2.1) and a larger amount of sodium will be absorbed in the carbon.

Originally two grains were prepared for the grains calcined to 1500 °C, but one of the grains broke in several pieces during the sodium vapour test. A piece of the analysed grain at 1500 °C had fallen off, so the real crack increase after sodium exposure is even larger than reported.

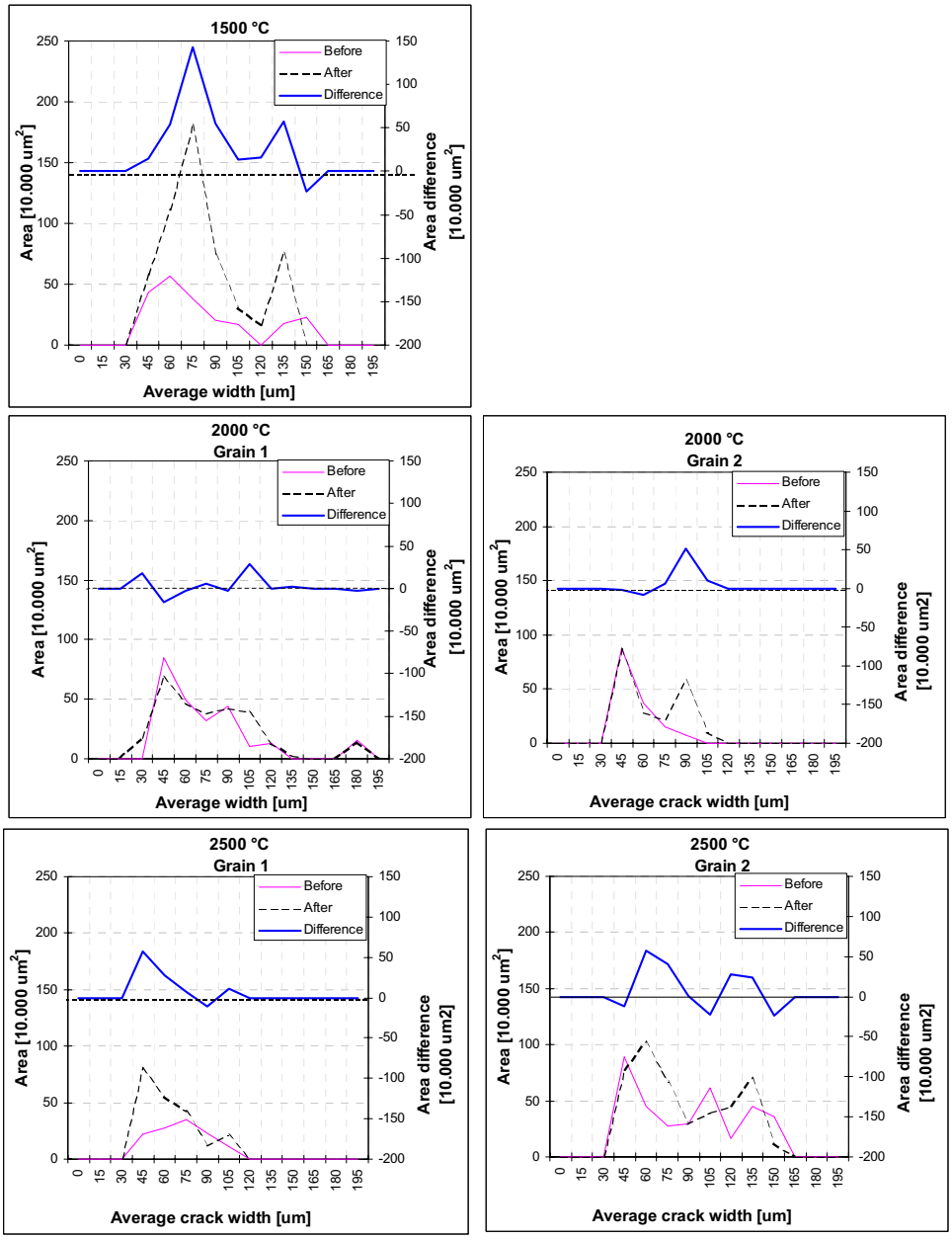

Figure 4.5. Crack distributions of the 5 analysed grains:

Graph on top: one grain calcined to 1500 °C,
Middle graphs: two grains calcined to 2000 °C (2000 °C grain 1 and 2000°C grain 2)
Bottom graphs: two grains calcined to 2500 °C (2500 °grain 1 and 2500°C grain 2).

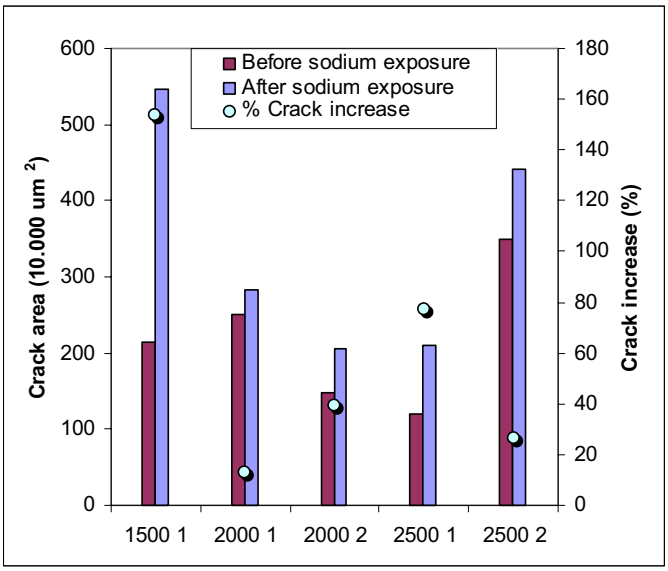

Figure 4.6. Crack area before and after sodium exposure on the 5 different grains. The circles indicate percent crack increase with the scale on the right vertical axis.

A partly automated method to quantify cracks in anthracite grains is presented. The amount of cracks increased more in the grains calcined to 1500 °C than in the grains calcined to 2000 and 2500 °C after sodium exposure. The trend with less cracking with increasing calcining temperature is reported before [3].

4.1.2 Petrol coke calcined to 1500 °C, 2000 °C and 2500 °C

Petrol cokes calcined to different temperatures was studied with respect to cracks before and after sodium exposure. No quantitative analysis was performed, but some typical trends were observed. Most of the grains withstood the sodium vapour without cracking and only 3 of the studied 63 grains were found to crack.

The grains that cracked were recognised with a particular structure and is shown in Figure 4.7. The pictures show the same area of a grain before (a) and after (b) sodium exposure. This type of sphere – like structures did not crack when the heat treatment temperature of the grains was higher (2000 °C and 2500 °C). A close up of the weak part of a grain heat treated to 1500 °C is shown in Figure 4.8. The weak area is probably in the border between flow and a more mosaic structure shown in Figure 4.8 (c). A bond located in the upper left part of the image going to the bottom right part is recognised with a more flow structure than the other parts of the image.

The reason for the other structures (calcined to 1500 °C) to withstand the sodium vapour could be a more pronounced flow structure in general (Figure 4.9). The different optical structures found within the cracked grains could have different ability to absorb sodium and could expand to a different degree and direction. Stress gradients in the structure border could become larger than the critical strength and cracks could be introduced.

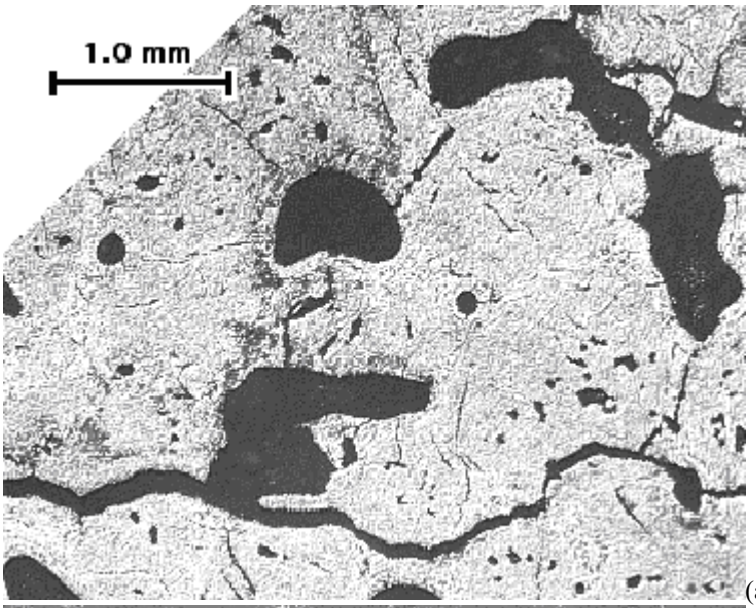

(a)

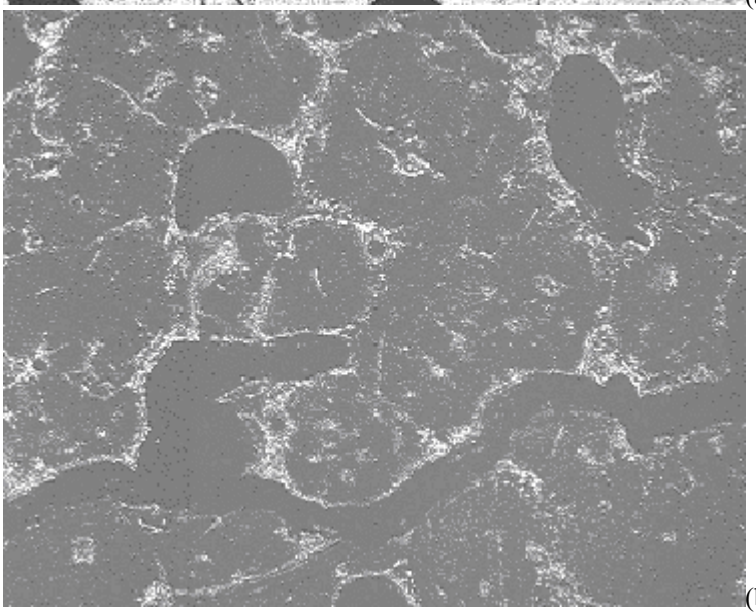

(b)

Figure 4.7. Petrol coke calcined to 1500 °C with the typical structure that cracked. The upper picture is before sodium exposure and the lower after. The large crack grows in the bottom part of the picture.

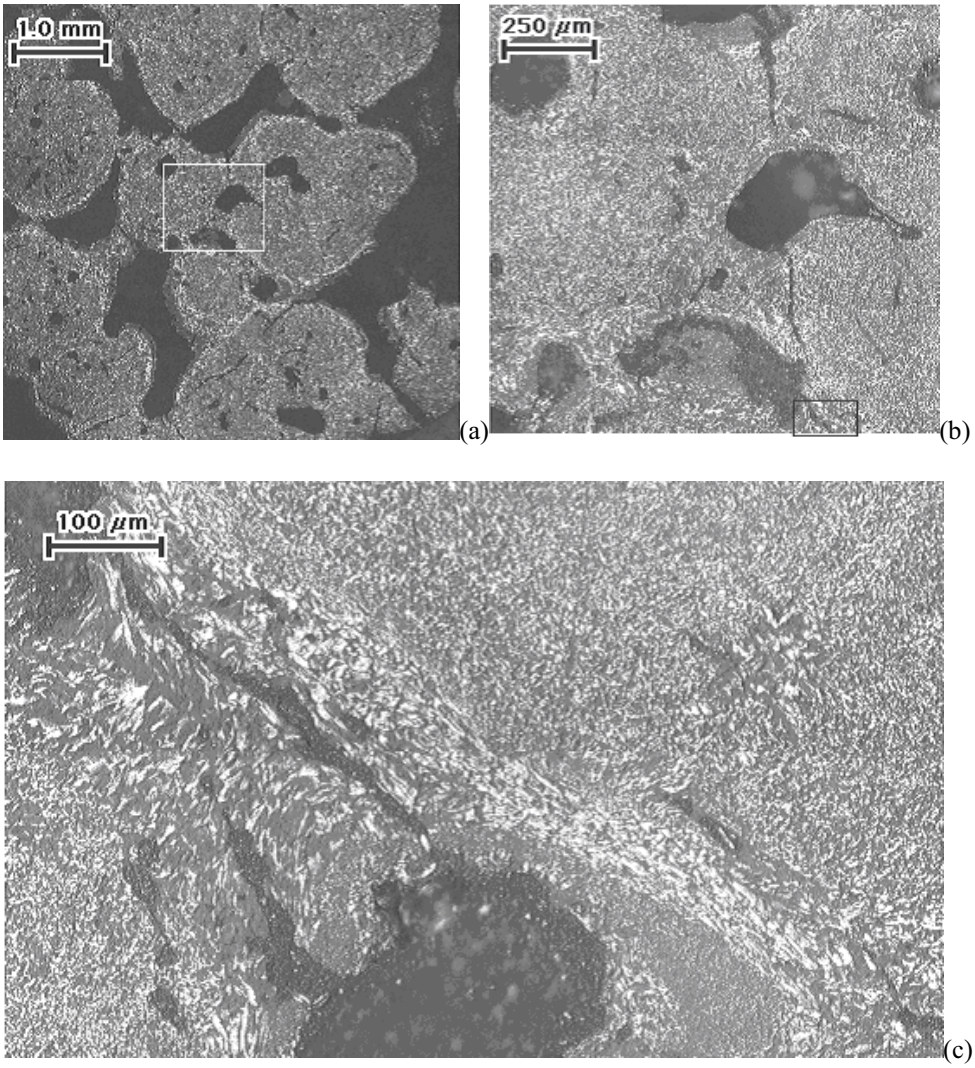

(a) (b) (c)

Figure 4.8. Details in the type of structure that cracked after sodium exposure. The image is captured in polarised light. The rectangle in picture (a) is zoomed out to picture (b). The rectangle of picture (b) is zoomed out to picture (c).

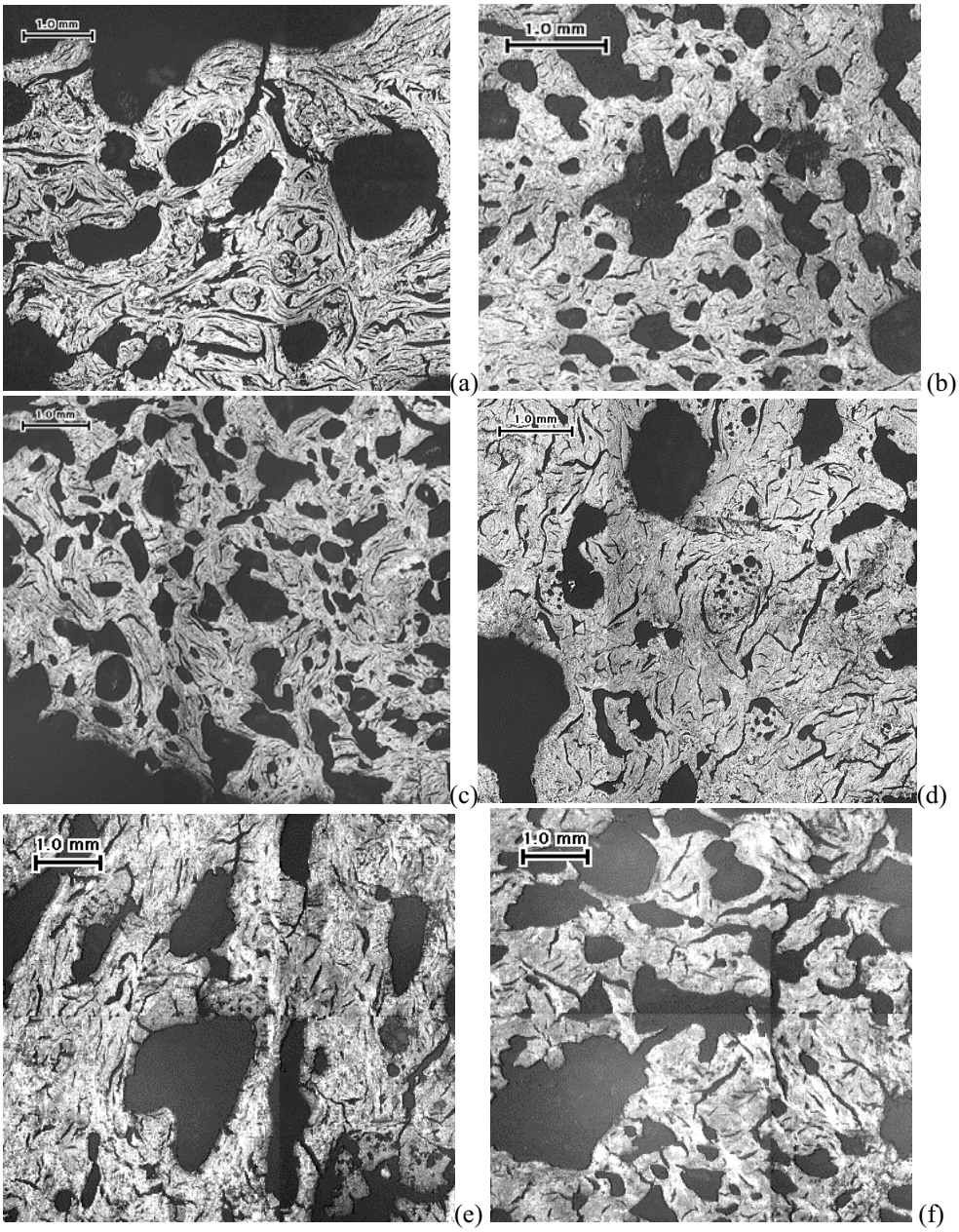

Figure 4.9. Examples of structures heat treated to 1500 °C that not cracked after exposure to sodium vapour.

4.1.3 Commercial cathode materials

The anthracitic material (30 % graphite) had the lowest resistance against sodium and large new cracks were visible (Figure 4.10). New visible cracks on the sides of the semigraphitic cylindrical sample were also observed, but on the pictured surface (Ø25 mm) no new cracks were observed (Figure 4.11). The semigraphitized material showed no visible new cracks after sodium exposure or electrolysis (a picture of the structure before and after electrolysis is shown in Figure 4.14).

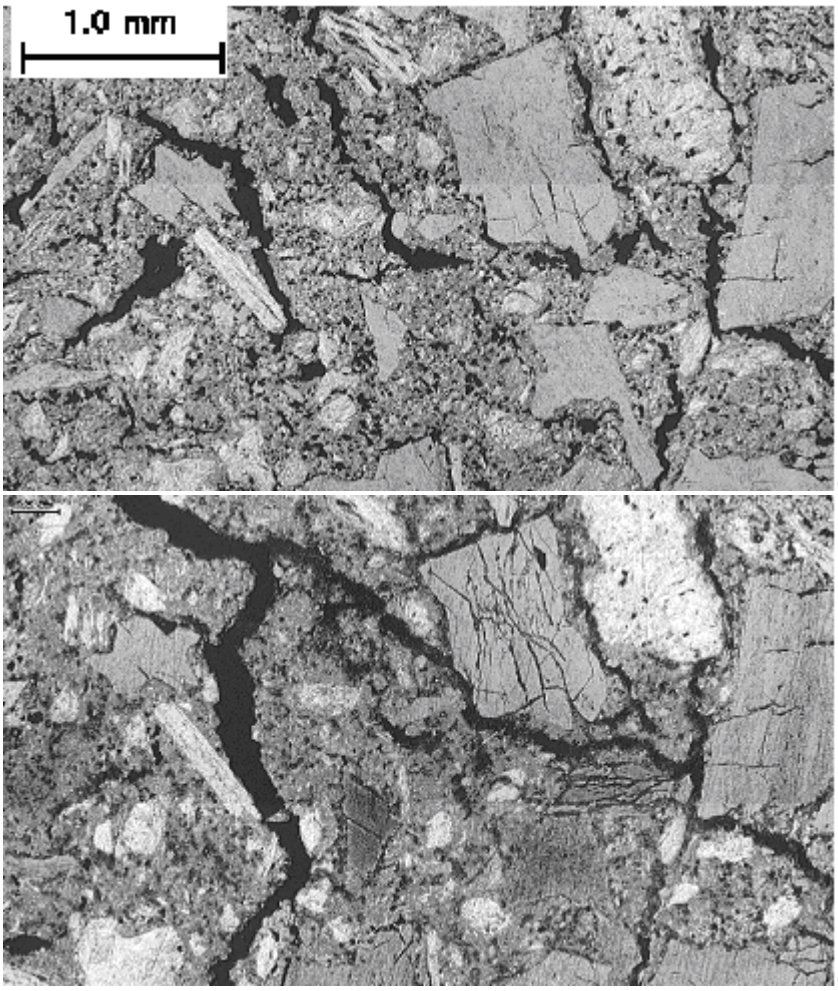

Figure 4.10. The same area of the anthracitic material (30 % graphite) before (a) and after b) sodium exposure. Cracks are seen in the anthracite grains and larger cracks are propagating in the binder phase. A graphite grain is seen in the upper right position with a lighter appearance after sodium exposure.

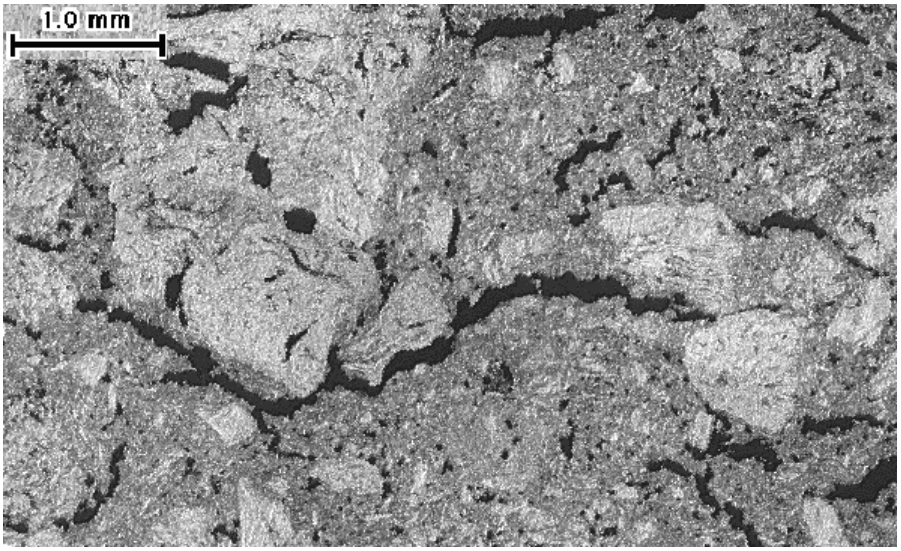

(a)

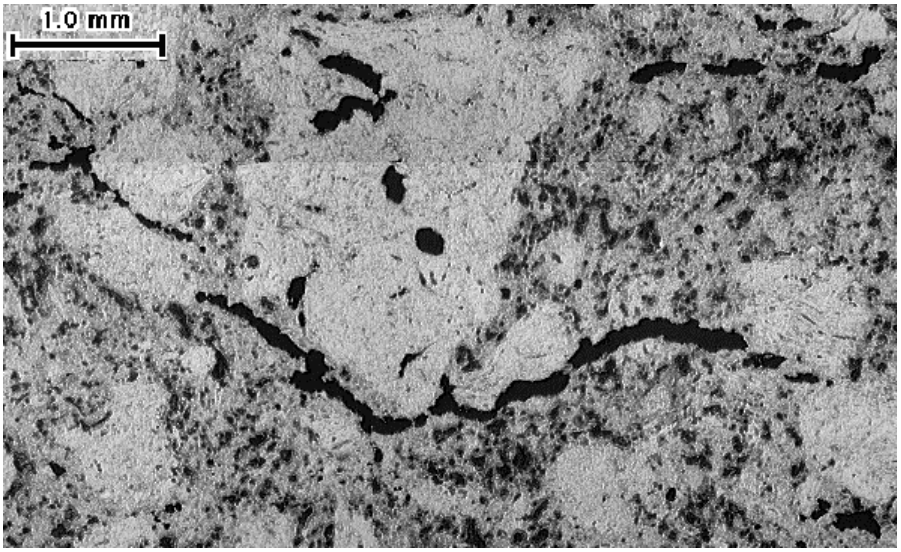

(b)

Figure 4.11. Semigraphitic material before (a) and after (b) sodium exposure.

4.1.4 Laboratory produced cathode materials

The laboratory produced materials consisted of petroleum coke with grains sieved in a fraction between 0.2-0.5 mm. These materials have a large amount of macro porosity (Figure 4.12). The samples heat-treated to 1500 °C were split up in the binder phase after sodium exposure. The absence of fines (grains < 0.2 mm) will cause a low strength of the material because of the small contact area between the grains. The material heat treated to 1500

°C was destroyed after sodium vapour exposure (probably because this material has a high sodium expansion, Figure 4.30). The materials heat treated to 2000 °C and 2500 °C withstood the sodium vapour test without changes in the structure.

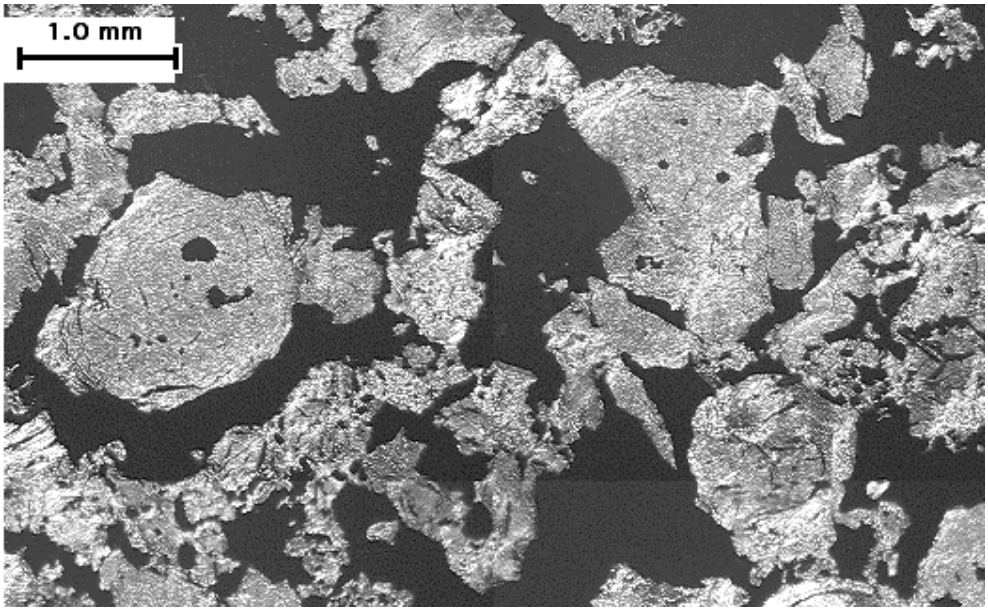

Figure 4.12. Structure of the laboratory produced cathodes.

4.1.5 Electrolysed surface study

The surfaces of the three commercial cathode materials were compared before and after a given time of electrolysis. In these studies, new cracks were only observed in the anthracitic material and the cracks were found in the anthracite grains (Figure 4.13). The cracks grew up to 1 hour of electrolysis, thereafter shrunk up to 6 hours. This behaviour can be explained by the penetration of sodium. The first pictures (Figure 4.13 a-c) can be attributed to a stress gradient in the material with a relaxation after 6 hours (Figure 4.13 d) when the material is saturated by sodium. In the other materials, semigraphitic and semigraphitized, no cracks were found at the given magnification. The penetrated bath constituents made it difficult to distinguish between the binder phase and penetrated bath. Cracks in this part of the structure might have been overlooked.

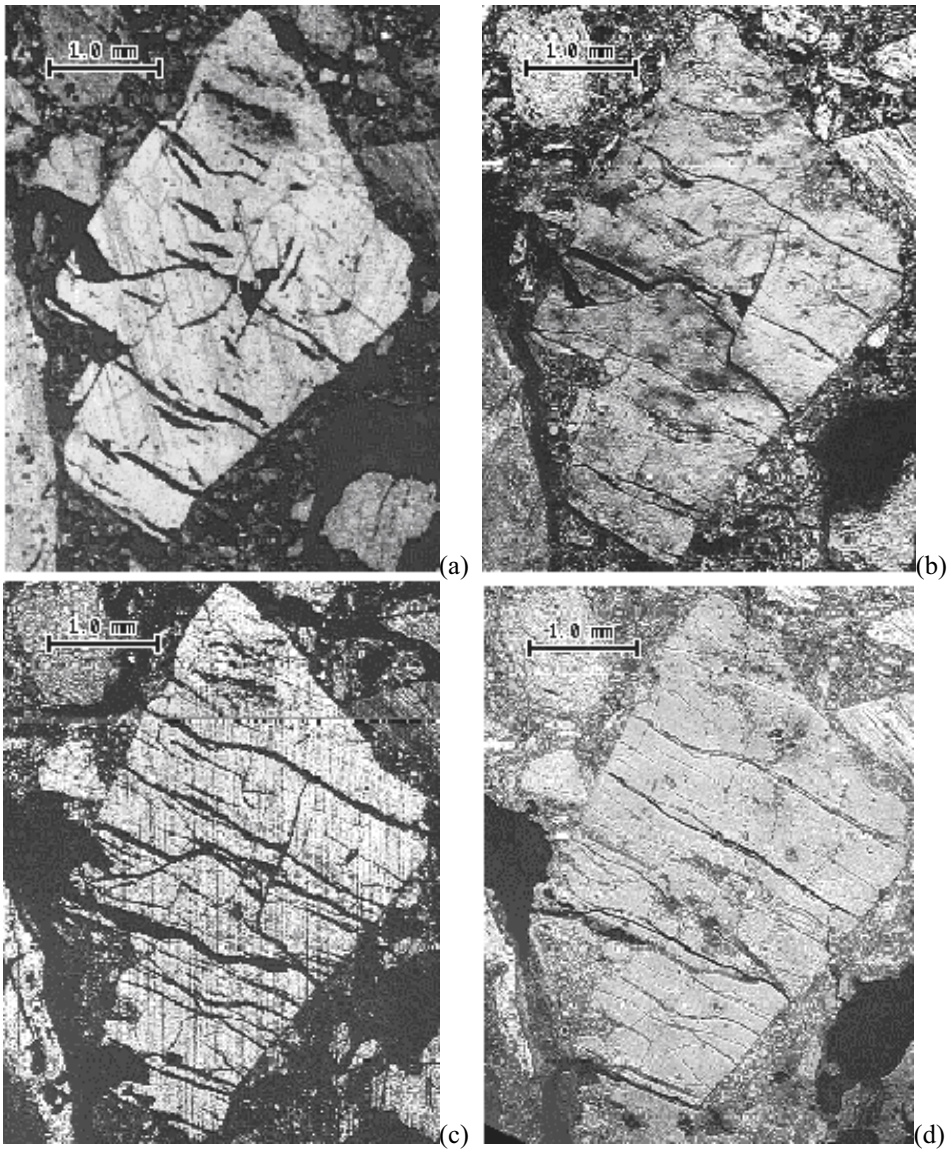

Figure 4.13. Crack development in an anthracite grain during electrolysis. Picture (a) before electrolysis, picture (b) after 30 minutes, picture (c) after 1 hour and picture (d) after 6 hours of electrolysis (i=0.2 A/cm^2).

An attempt to generate cracks in the semigraphitized material during electrolysis was made with a melt oversaturated with alumina (A_c^e = 0.4) and a higher current density of 1.5 A/cm^2. A melt oversaturated with alumina should give an enhanced sodium expansion [49] which possibly introduces cracks. No new cracks were found before and after 4 minutes of electrolysis (Figure 4.14). The surface was also pictured after 30 minutes of electrolysis with the same result.

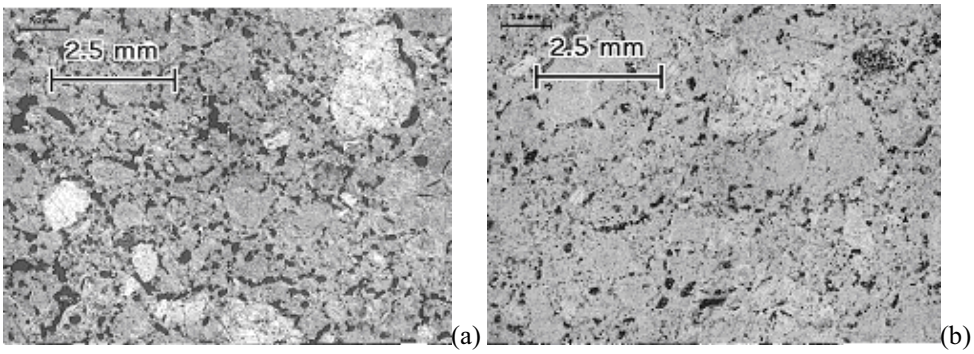

Figure 4.14. Pictures of the semigraphitized sample before (a) and after 4 minutes (b) of electrolysis. No new cracks are observed.

The E – modulus is higher in the anthracitic than in the semigraphitic material (Chapter 4.4.4). The heat treatment temperature of the binder is the same (~1200 °C) so the difference is probably attributed to the filler material which is 100 % graphite in the semigraphitic material and 30 % in the anthracitic (the rest is anthracite). This probably means that the anthracite grains are stiffer than the graphite grains and the stresses are probably higher in the anthracite for a given expansion. The anthracitic material has the highest sodium expansion during electrolysis (Figure 4.26) and the highest sodium content after the sodium vapour test (Figure 4.46). The large expansion combined with a high E -modulus will introduce high stresses.

On the macro level the structure of the anthracite grains is more laminated than the petrol coke grains, which exhibit a more random structure. The weak point in an anthracite grain is probably between the laminates and in cracks initiated from the heat treatment. The anthracite grains always crack to some extent after sodium vapour exposure (Figure 4.1- Figure 4.4), but the heat-treated petrol cokes rather seldom (Figure 4.9). The same ranking is observed in the commercial materials.

4.1.6 X-ray diffraction

The samples exposed to sodium (either by electrolysis or sodium vapour) were analysed by XRD as described in Chapter 3.2. All the results are given in Table 4.1. The measured distance between the graphene layers, the d_{002} – distance, is shown for at least two parallels at each condition for the commercial materials in Figure 4.15 and for the laboratory produced materials in Figure 4.16.

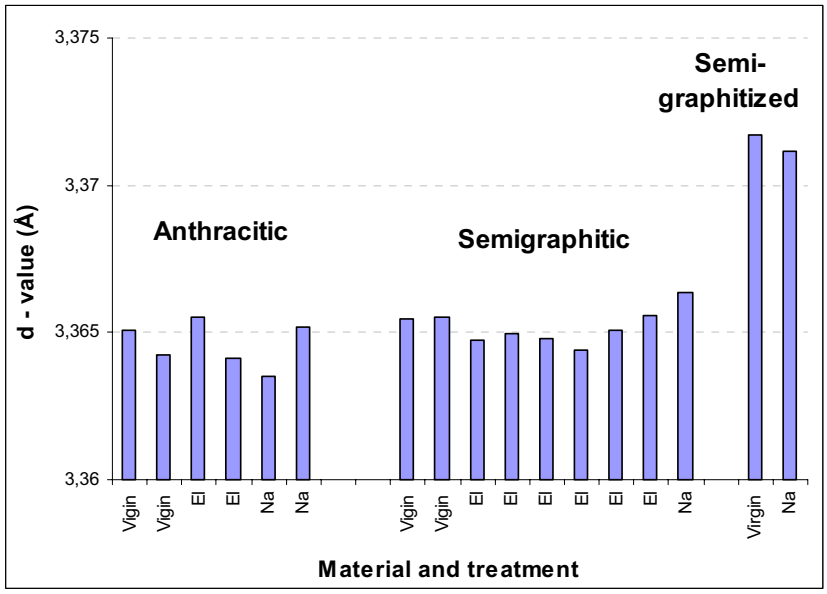

Figure 4.15. d – values for virgin, electrolysed and sodium exposured material. No difference within one material is seen. Abbreviations on absicca: Na – after Na exposure, El – after electrolysis.

The d – distance does not change after the samples are electrolysed or exposed to sodium vapour, except in one case; the laboratory produced material heat treated to 1500 °C. In this material the d-value increased from 3.44 Å to 3.49 Å or an increase of 4.3 % after both sodium vapour and electrolysis. This material has the highest sodium expansion of the measured materials (Figure 4.30).

The XRD scans of parallel samples of the laboratory produced material heat treated to 1500 °C are shown in Figure 4.18. Compared to the pattern of the anthracitic material (Figure 4.17) with the next largest sodium expansion of the tested materials, the peak is shifted to higher d – values.

The peaks of the more amorphous materials are rather broad and the effect of the Lorentz polarisation factor and the carbon atom scattering factor could influence the analysis at lower diffraction angles. These factors are not calculated, but according to Dahn et al. [71] the d_{002} peak is accepted as long as the width of the peak is below 2° 2θ and $d_{002} < 3.55$ Å. As seen from Table 4.1 all the measurements are below these limits.

The d–value for the laboratory produced material heat-treated to 2500 °C is approximately the same (slightly lower) than the value measured for the semigraphitzed material (Figure 4.15). This could be expected, as the filler and heat treatment temperature of these two materials approximately is the same. The d – distance decreases with heat treatment temperature as expected for the laboratory produced material (Figure 4.16).

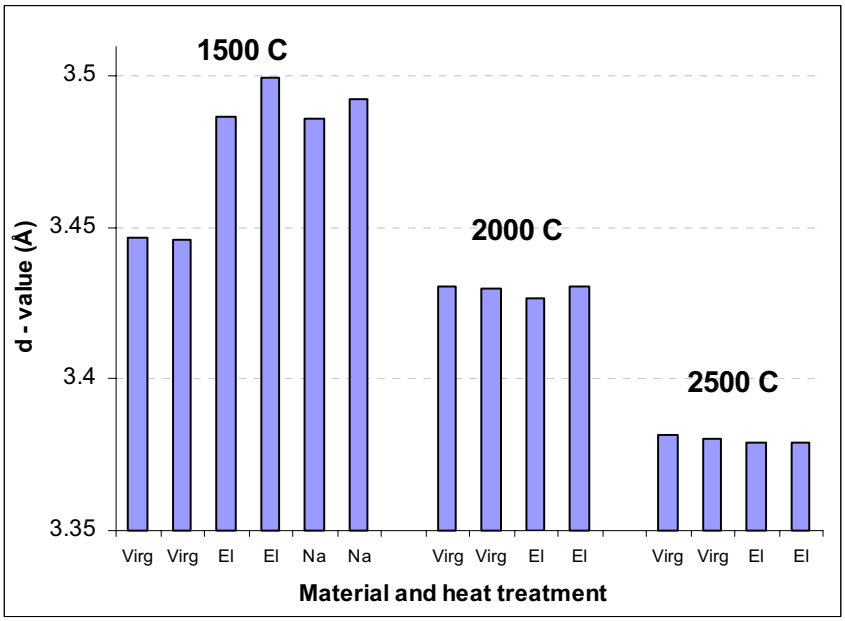

Figure 4.16. d - values for virgin, electrolysed and sodium exposured laboratory produced material. The heat treatment temperature is shown above the coloumns. The material heat – treated to 1500 °C has an increase in d – spacing the other not. Abbreviations: Na – after sodium exposure, El – after electrolysis, Virgin – virgin material.

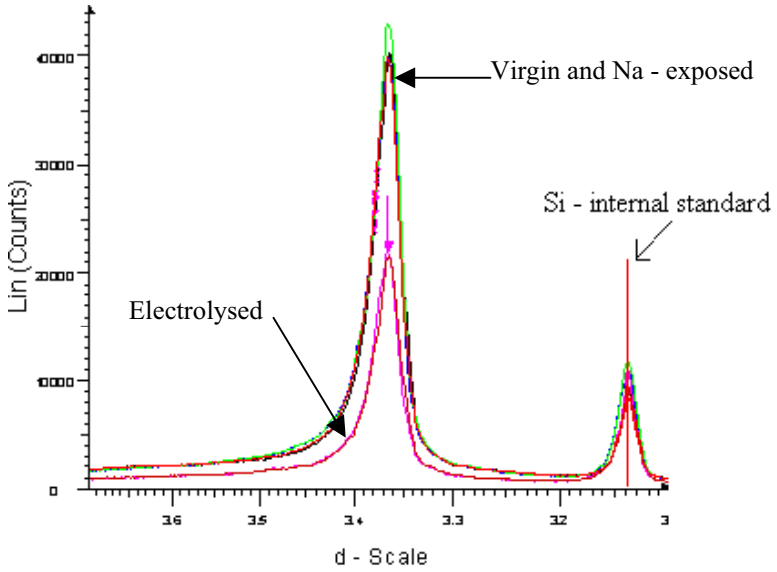

Figure 4.17. X-ray diffraction scans of anthracitic cathode after electrolysis and sodium exposure as well as virgin. No changes in the d_{002} – value are observed.

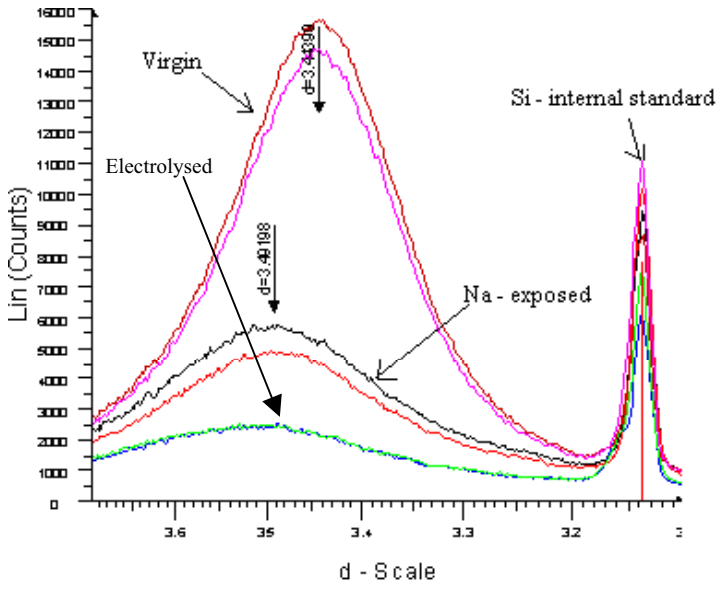

Figure 4.18. Laboratory produced cathode calcined to 1500 °C before (highest peaks) and after sodium exposure (lowest peaks). The average d – value is larger for sodium exposed and electrolysed material.

The intensity of the peaks varies between the parallels as the sample preparation influences the orientation of the crystals. The amount of powder and the density on the analysed surface was not given any special attention, as the d_{002} - distance was the wanted value.

Jouncourt et al. [12] made similar studies on pitch coke samples heat treated between 800-1900 °C in sodium vapour at 700 °C with a sodium pressure of 0.9 atm. The samples were protected from air exposure and an increase in d – values was found in all materials after sodium exposure. The d_{002} increased more with lower heat treatment temperature.

As the materials expand during electrolysis an increase in the d_{002} – spacing could be expected in all materials. The reason for not observing an increase in the other materials could be the high intensity of the peak related to the more crystalline part of the material (for example the graphite in the anthracitic material). The intensity from the layers with an increased d_{002}-spacing after sodium exposure might be too low compared to the peak from the more graphitic part of the material, and the distance increase vanishes. In the laboratory produced material heat-treated to 1500 °C where the d_{002} – spacing is measured to increase, the intensity of the d_{002} peak is rather low and the lower intensities are more visible.

The sample shrinks after the current is switched off in the electrolysis experiments and some sodium probably escapes the structure ([52], Chapter 4.4.2). A reduction of sodium content with decreasing sodium pressures is also found in the sodium vapour experiments in similar materials [19, 30]. This means probably that the measured sodium content is smaller than the content during the experiments. The d_{002} – distances should probably been measured in situ.

Table 4.1. XRD – results for the different samples. Abbreviations: A – anthracitic, SG – semigraphitic, SGZ – semigraphitized, Syn – laboratory produced, Na – after Na exposure, El – after electrolysis.

	d (Å)	FWHM (2θ)	Area (Counts x 2θ)
A Virgin I	3.365	0.267	3104
A Virgin II	3.364	0.257	3253
A El. I	3.366	0.241	1557
A El. II	3.364	0.249	1549
A Na I	3.364	0.261	2970
A Na II	3.365	0.264	3006
SG Virgin I	3.365	0.273	3650
SG Virgin II	3.365	0.292	3685
SG El. I	3.365	0.228	2785
SG El. I	3.365	0.219	3726
SG Na I	3.366	0.242	5351
SGZ Na I	3.371	0.305	5102
SGZ Na II	3.371	0.296	5457
Syn 1500 Virgin I	3.447	1.454	3978
Syn 1500 Virgin II	3.446	1.459	4270
Syn 1500 El I	3.487	1.621	447
Syn 1500 El II	3.500	1.72	462
Syn 1500 Na II	3.486	1.644	1324
Syn 1500 Na	3.493	1.646	1132
Syn 2000 Virgin I	3.430	0.472	5967
Syn 2000 Virgin II	3.430	0.476	6101
Syn 2000 El I	3.427	0.46	1894
Syn 2000 El II	3.431	0.463	1883
Syn 2500 Virgin I	3.381	0.36	4204
Syn 2500 Virgin II	3.381	0.35	4252
Syn 2500 El II	3.379	0.284	1800
Syn 2500 El I	3.379	0.283	1850

4.2 Sodium expansion

In this chapter the sodium expansion measurements from the different apparatuses shown in Chapter 3 are presented. Some of the results with radial penetration are not part of a systematic study, but results achieved during the struggle to make a satisfactory apparatus for creep measurements. The measurements have been compared to the work of Støre et al. [46] who used samples from the same block as used here and the apparatus described in Figure 3.3. All samples used in this work and in the selected work of Støre [46] were taken out parallel to the extrusion direction of the block.

Variations between parallel sodium expansion measurements will be found, as the materials not are homogenous. In the work of Støre et al. [46], 2-4 parallel experiments were performed at different current densities in several materials. In the measurements below 0.88 A/cm^2 the parallels never varied with more than ± 15 %. The variation in the absolute expansion was always within 0.1 %. This limit is also maintained for the 10 parallel measurements in four different set-ups in Figure 4.19 (even though the three highest curves could be high as a result of steel expansion).

4.2.1 Sodium expansion - apparatuses

The sodium expansion of the semi-graphitic material with a current density of 0.2 A/cm^2 is shown for the different apparatuses in Figure 4.19. It is seen that the expansion curves have some distinct differences. The two lowest curves (with the lowest and slowest expansion) are measured with the apparatus used for creep measurements (Figure 3.8). The expansion is here measured in the middle of the sample top, while the measuring rod covers the whole surface of the sample top in the other apparatuses. As sodium first penetrates the cylinder wall, the middle part will expand slower, as observed (Figure 4.19). This slower expansion was also found by numerical calculation by Zolochevsky et al. [72], which is shown in Figure 4.34.

The three upper curves in Figure 4.19 with the largest expansions are probably too large because of an experimental error. The steel tubes extending downward from the crucible and upward from the sample of the set-up described in Figure 3.5 are probably expanding during electrolysis. The lower tube was used to hold the crucible at a steady height and the upper was used as an extension to the distance-measuring device (LVDT). Both worked as current connectors and had together a total length of approximately 1 meter. These tubes were relative thin (outer diameter of 15 mm and inner 12 mm) and 10 Amperes gives a relatively high current

density of 15.8 A/cm^2. The steel could increase in temperature with a resulting expansion although the temperature under the crucible appeared constant.

In a blank experiments without the insulation disk and melt, the expansion was measured to ~ 0.03 % relative to the 60 mm sample when the temperature in the middle was constant. With 5 A this value was reduced to ~ 0.01 %.

The other curves coincide well even with small pressure differences and different sample geometry. In two of the experimental set-ups, a hole in the sample was needed for the measuring pin (Figure 3.4). The hollow cylinders have a smaller volume and will be saturated faster.

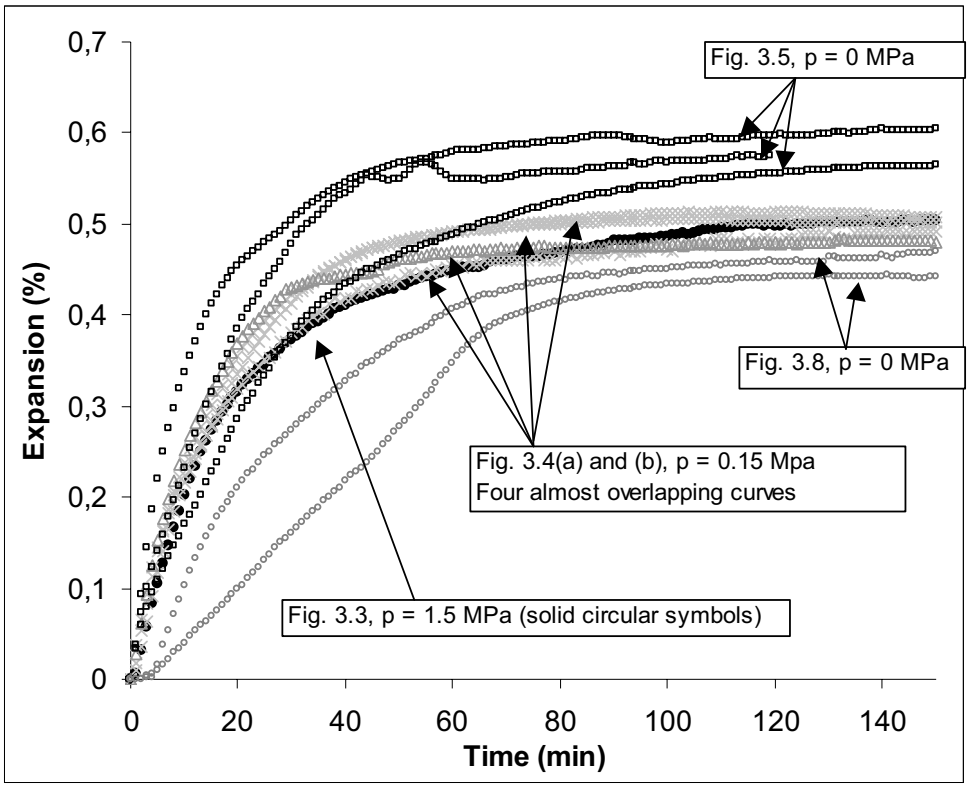

Figure 4.19. Sodium expansion of semigraphitic material in the different apparatuses with a current density of 0.2 A/cm^2. The two lowest curves with the slowest expansions are measured with the measuring rod in a small area in the middle of the sample, the others are measured on the whole sample top. The Figure references in the text boxes refer to the different apparatuses presented in the experimental part.

4.2.2 Sodium expansion – cryolite ratio (CR)

In Figure 4.20 the expansion of the semigraphitic material is shown with two different cryolite ratios with a current density of 0.2 A/cm^2. In Figure 4.21 (from Støre et al. [46]) the expansion on the same material with a current density of 0.7 A/cm^2 and a pressure of 5 MPa is shown. The expansion in Figure 4.20 is believed to be somewhat high due to steel expansion as discussed in the previous section.

The expansion is, as reported before [41, 47], higher for experiments with a more basic melt. It is seen that the time to reach saturation is longer for the experiments with a current density of 0.2 A/cm^2, but within one current density the time for saturation is the same. This means that the sodium activity does not affect the time to reach saturation around these activities. This is further discussed in Chapter 4.2.3.

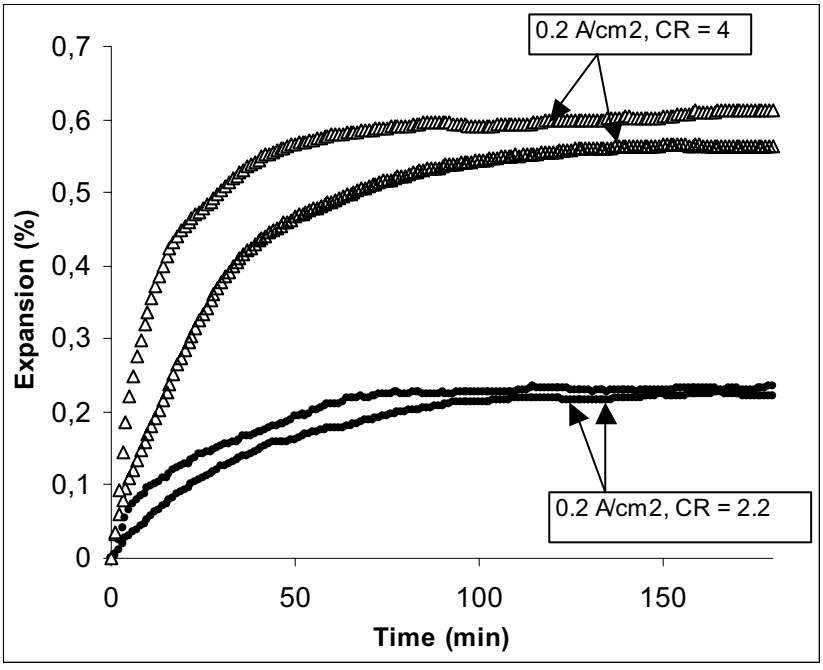

Figure 4.20. Two parallel experiments on two CR's at a current density of 0.2 A/cm^2. The apparatus in Fig. 3.5 with no pressure was used.

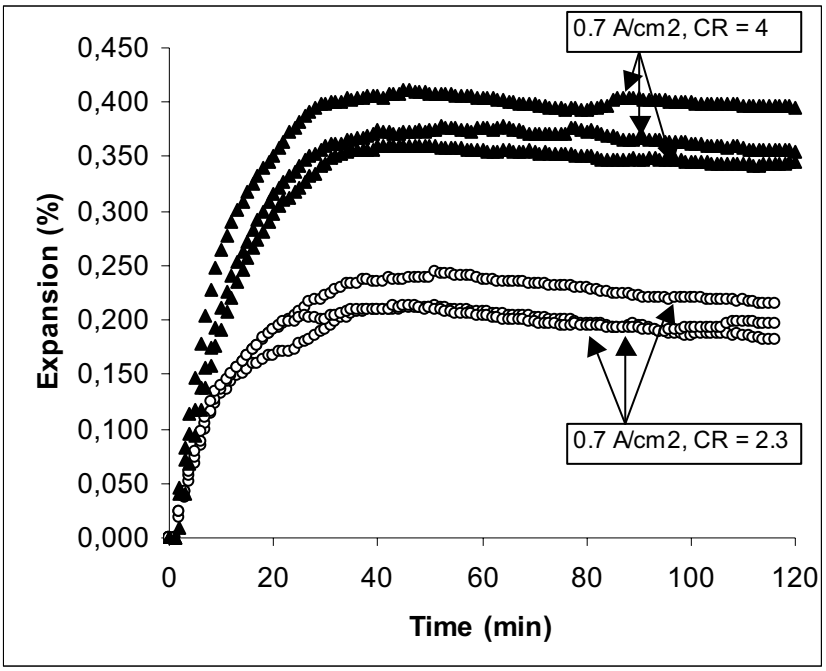

Figure 4.21. Sodium expansion at two different CR with a current density of 0.7 A/cm^2 and a pressure 5 MPa. From Støre et al. [46].

4.2.3 Sodium expansion – sample geometry and current density

A hollow sample will contain less material for sodium to penetrate and a shorter time to saturation could be expected. This is seen in Figure 4.22 where a hollow cylindrical sample (inner radius of 7 mm) and solid cylindrical samples with the same outer diameter of Ø30 mm are compared (semigraphitic material). The open lighter symbols represent the hollow cylinders at different current densities. For the same current density the hollow cylinder expands faster and reaches saturation first. The expansion of the solid and hollow cylinders was measured in the apparatus described in Figure 3.3 and Figure 3.4 respectively.

The time to reach saturation decreases when the current density is increased (Figure 4.22). It takes more than 200 minutes for the samples with a current density of 0.06 A/cm^2 to reach saturation, while the saturation time is less than 60 minutes for the samples with a current density of 0.7 A/cm^2. The total expansion is reduced with a current density of 0.06 A/cm^2 (Figure 4.22). Støre et al. [46] reproduced these results (with 5 MPa pressure). The same trends were also found for the anthracitic and semigraphitized material.

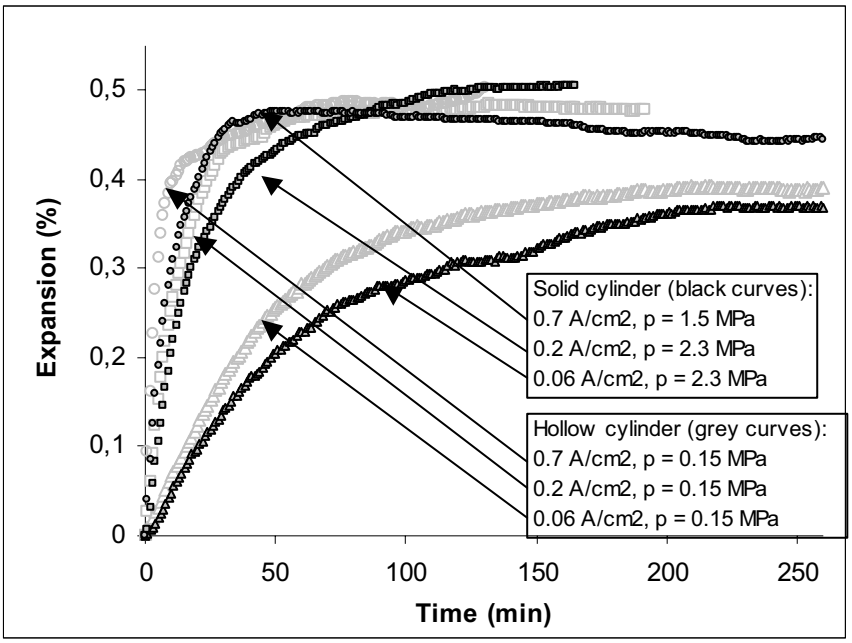

Figure 4.22. Expansion of semigraphitic solid and hollow cylinders at different current densities. The grey curves are measure on hollow cylinders and the black are measured on solid cylinders. As the current density increases the samples reaches saturation faster.

The observed expansion at the lowest measured current densities (0.06 A/cm^2 and 0.20 A/cm^2) supports the hypothesis that sodium is directly reduced in the carbon. In the measurements of Gudbrandsen et al. [13] where the electrolytic production of aluminium carbide was studied, they claimed to be below the decomposition voltage of aluminium in all their experiments lasting for 4 hours. The highest reported current density in these experiments was 0.2 A/cm^2. This gives reason to believe that aluminium was not formed in the experiments with the lower current densities (0.06 A/cm^2 and 0.20 A/cm^2) presented here. As no aluminium and sodium metal is present in the melt the equilibrium Eq. (2.1) will not take place and all the expansion could be caused by a direct reduction of sodium in carbon. At a current density of 0.20 A/cm^2 the total expansion is approximately the same as at higher current densities. This gives reason to believe that the penetrated sodium is directly reduced in carbon also at higher current densities.

The sodium activity on the cathode surface in the present experiments could be different from the experiments of Gudbrandsen et al. [13] as an acidic bath was used, and a propeller was used to stir the melt. The overvoltage increases with acidity of the melt [5] and reduces with stirring, so the overvoltage might be in the same range.

4.2.4 Sodium expansion – pressure

Some experiments with low pressures can be compared with the measurements of Støre et al. [46] who applied a pressure of 5 MPa in all the experiments. The sodium expansion for the semigraphitic material with 0.2 A/cm^2 and 0.15 MPa pressure (Figure 4.19) is replotted with the data of Støre et al.[46] (5 MPa) in Figure 4.23. A reduction of approximately 30 % in the maximum expansion can be calculated from the middle values. Two parallel measurements with a current density of 0.5 A/cm^2 is also shown to increase the credibility of the measurement with 5 MPa pressure.

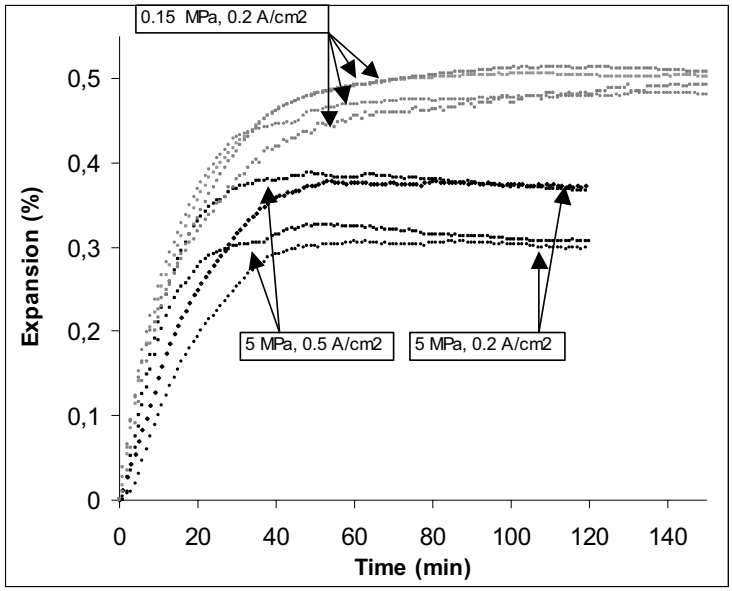

Figure 4.23. Sodium expansion in semigraphitic material with 0.15 and 5 MPa pressure and a current density of 0.2 A/cm^2. As only two parallels are measured at 0.2 A/cm^2, two parallels with 0.5 A/cm^2 is shown to increase the credibility. The distinct difference between the saturation expansions of the parallels with 5 MPa pressure is scatter in the measurements.

One measurement with a pressure of 1.5 MPa is plotted with the expansions with a pressure of 0.15 MPa in Figure 4.19. This expansion coincides with the measurements with a pressure of 0.15 MPa. One measurement gives a low credibility, but as seen from the measurements with 0.7 A/cm^2 (Figure 4.24), also here the measurement with 1.5 MPa do not seem to differ from the measurements with 0.15 MPa pressure. With a pressure of 5 MPa [46], a reduction of approximately 25 % is calculated (Figure 4.24). A pressure of 1.5 MPa gives most likely a reduced expansion, but seems to have a smaller

effect than reported from Schreiner [44, 52] who measured a 20 % reduction with 1 MPa pressure at similar electrolysis time (1.5 hours).

In the study of Schreiner [44, 52] the increase from 0 to 1 MPa had the largest effect of the studied pressures (0-10 MPa). Before the electrolysis started, a pressure of 10 MPa was applied for 30 minutes to settle the apparatus. After 30 minutes without pressure the electrolysis was started with the wanted pressure. If the data is studied [52] the sample expands after the pressure is released. Most of this expansion is probably creep recovery of the steel extension from the sample, it addition to a probable smaller creep recovery of the carbon sample. This creep recovery would be included in the measured expansion in an experiment without pressure, and a larger expansion could be the outcome. In the experiments with pressure, the creep of the steel extension was subtracted, which was measured in a blank test. But the creep recovery was not mentioned. The creep recovery would affect the smaller expansions more, as the recovery could have the same value in each experiment. This means that the reduction in expansion is smaller in the more graphitic materials.

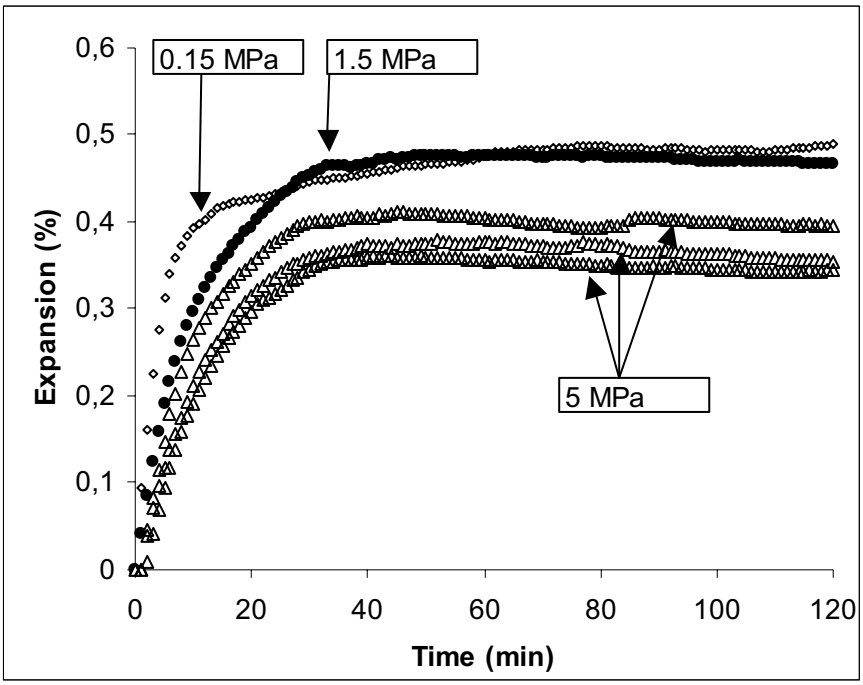

Figure 4.24. Sodium expansion in semigraphitic material with different pressures with a current density of 0.7 A/cm^2.

If the reduced expansion should be explained by the later presented creep measurements, a longer experimental time should result in a larger creep

and larger reduction in expansion. In Figure 4.24 the expansion is reduced approximately 0.1 % (from 0.45 to 0.35 %). If the creep equation (Eq. 2.32) is used with the fitted constants for the semigraphitic material (Table 4.3) a constant pressure of 15 MPa is needed to calculate a creep strain of 0.1 % after 120 minutes. This seems like a large pressure, but the calculated axial stresses in a similar sample with a pressure of 2.3 MPa during sodium expansion is between 20 MPa in compression and 5 MPa in tension, dependent of the radial coordinate and time (Appendix D, [29]).

If previous sodium expansion measurements with pressure are studied (Figure 2.12), the data from Dewing [34] and Peyneau [43] approximately overlap. These electrolysis experiments lasted for approximately 10 hours and a larger creep should be expected than measured after 1-2 hours like Schreiner [52] and Guilliatt and Chandler [51]. The reduction in expansion in the measurements from Guilliat below 5 MPa is less, and if the creep recovery of the apparatus of Schreiner existed and is subtracted, this would also be the outcome here.

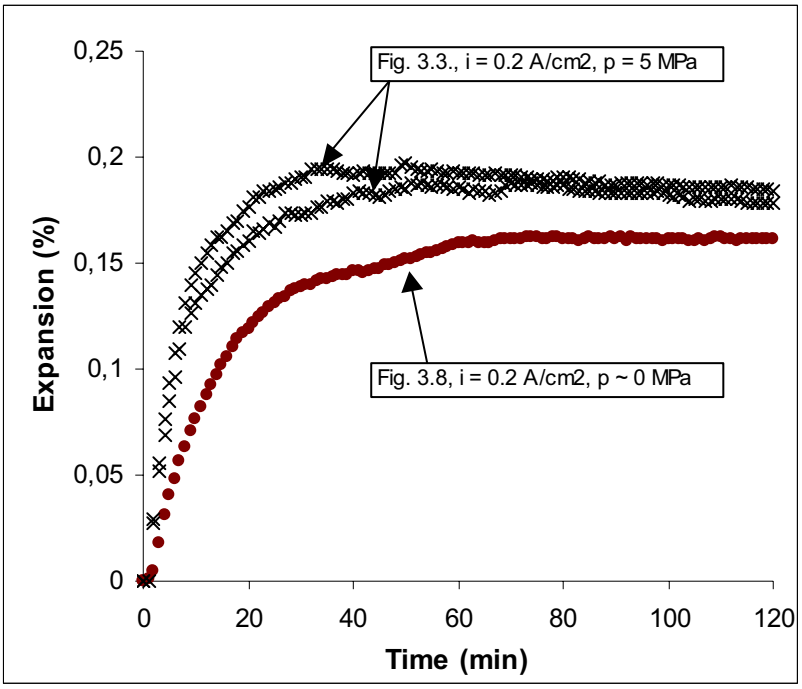

Figure 4.25. Sodium expansion of the semigraphitized material with current density 0.2 A/cm^2 with different pressures. The Figure referred to in the text box is the set-up of the apparatus used in the experiment.

In Figure 4.25 one experiment with the semigraphitized material at a current density of 0.20 A/cm^2 is presented. The expansion curves with a pressure of

5 MPa are redrawn from Støre et al. [46]. The expansion is slightly larger in the samples with 5 MPa pressure, which probably is wrong, but concerning scatter because of an inhomogeneous material, the reduction in expansion seems smaller than in the semigraphitic material. The pressure might have less influence in a material with lower expansion. This is also seen in Figure 4.29 where the expansion of graphite under different experimental conditions is presented. The experiment with a pressure of 5 MPa seems not to have a lower expansion.

4.2.5 Sodium expansion – materials

Sodium expansion for samples from two cathode producers is shown for anthracitic (Figure 4.26) and semigraphitic material (Figure 4.27). In Figure 4.28 the expansion of semigraphitized material from the same producer at from two different production periods is shown (the material with the highest expansion was produced approximately 5 years after the other). The experimental set-up is equal under all conditions (Figure 3.3) with CD = 0.7 A/cm^2 and a pressure of 5 MPa. The ranking of the materials is, is as reported before [3], with the anthracitic material expanding the most and the semigraphitzed material the least. The time for saturation is in the same sequence, with the anthracitic material expanding slowest.

A tempting explanation for longer saturation times for increasing expansion could be that a larger sodium volume needs a longer time to saturate the structure. But this is not straight forward as explained in Chapter 4.2.2. The sodium expansion at CR = 2.3 is about half the expansion at CR = 4 but the saturation time is the same. This probably means that the material (not concentration) determines the saturation time and the diffusion coefficient as calculated in Chapter 4.2.7.

The shape of the curves shows some distinct differences between the materials. The semigraphitic material seems to creep more after saturation (Figure 4.27). This trend is also measured in the creep measurements in Chapter 4.4. The measurements for the materials A1, SG1 and SGZ-time-2, are taken from Støre et al. [46]

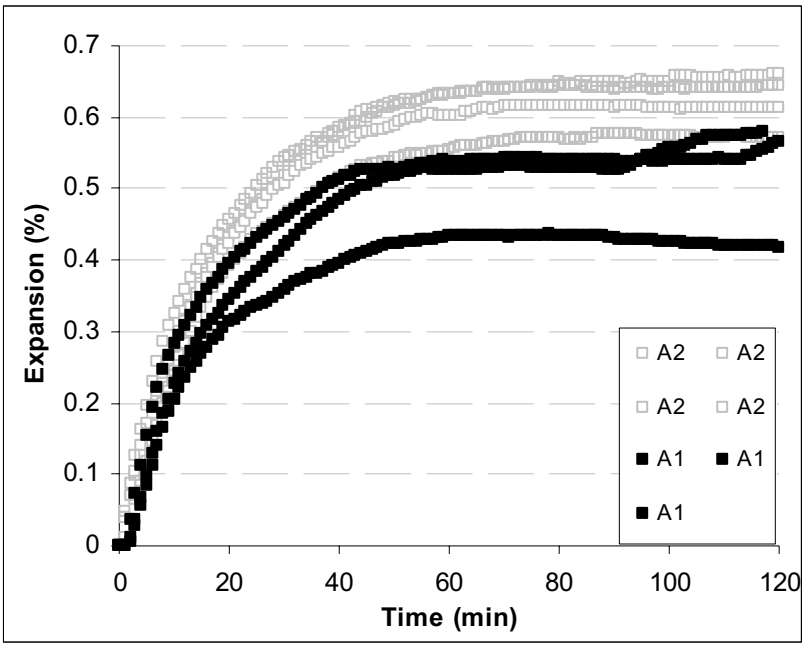

Figure 4.26. Sodium expansion of anthracitic material from two producers.

The change in sodium expansion for the semigraphitized material from one cathode supplier at two production periods is shown in Figure 4.28. The material with the lowest expansion was produced approximately 5 years before the other. The total expansion is different, but the time to saturation is approximately the same.

In Figure 4.29 the expansion of graphite in the different apparatuses is shown under different experimental conditions. The different pressures and current densities do not have large effect the expansion. The filled triangle's shows the expansion under the same experimental conditions as in the three Figures above. It is seen that graphite and the semigraphitized material expands fastest and reaches saturation at the shortest time.

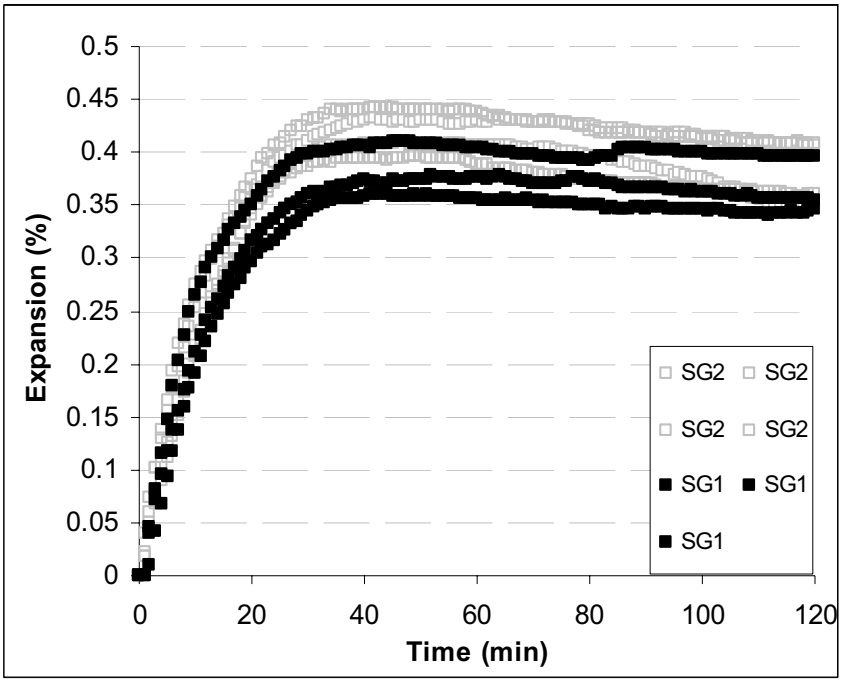

Figure 4.27. Sodium expansion of semigraphitc material from two producers.

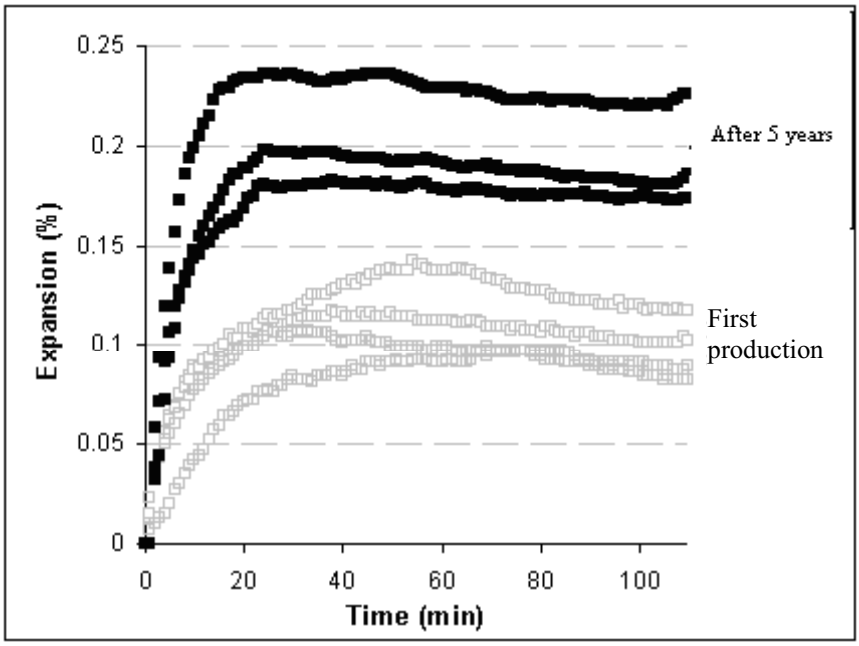

Figure 4.28. Sodium expansion of semigraphitized material from one producer. The time of production is different by approximately 5 years.

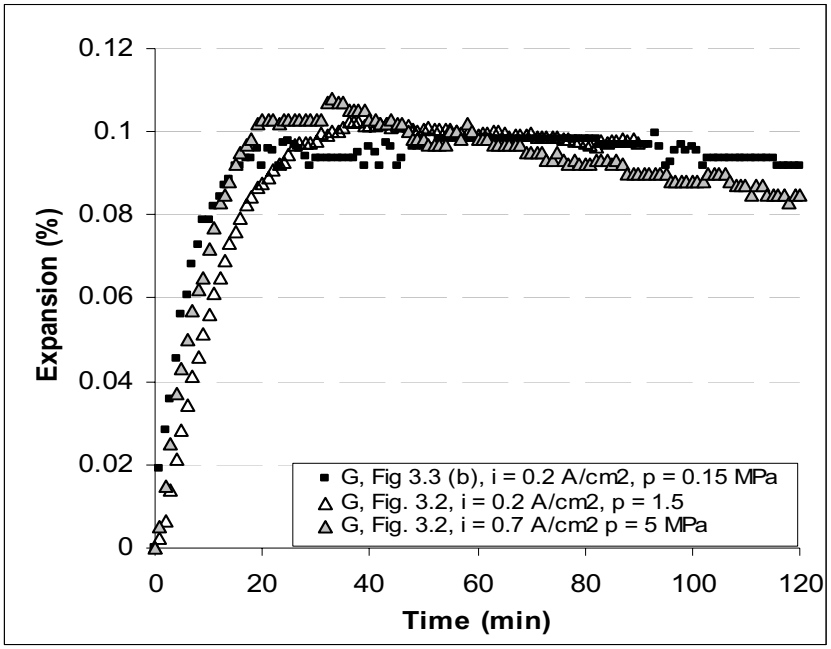

Figure 4.29. Sodium expansion in graphite with different pressures and current densities. The apparatus used in each case is referred to in the symbol box.

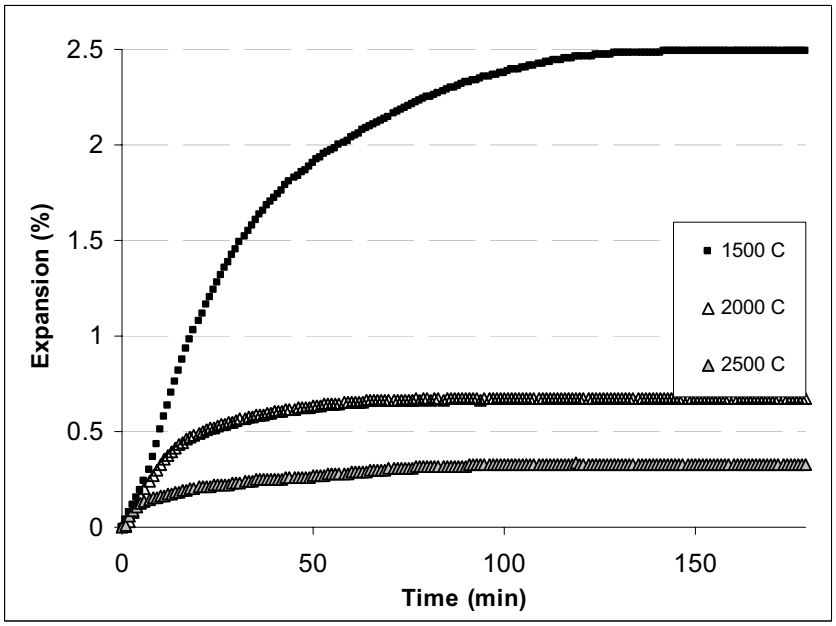

Figure 4.30. Sodium expansion of the laboratory produced materials heat treated to different temperatures with a pressure of 2.3 MPa.

In Figure 4.30 the sodium expansion of the laboratory produced material is presented. Only one sample for each heat treatment temperature is measured, but the trend is very clear. The material heat treated to 1500 °C have at least 3 times larger expansion compared to the materials heat treated to 2000 °C and 2500 °C. This is the same trend as seen in the commercial materials and is reported before [41, 42, 43]. The time to saturation is also decreased as the heat treatment is increased.

In the presented sodium expansion results special attention is given to the saturation time. A summary of the time to saturation could be expressed as shown in Figure 4.31 where the relative expansion is plotted versus time. The time to saturation increases with graphite content, current density and sample radius. The time is not affected by the tested cryolite ratios (CR = 4 and CR = 2.2). The total expansion increases with decreasing graphite content and inreasing CR as reported before [3]. At some current density below 0.20 A/cm^2 the total sodium expansion seems to decrease (Figure 4.22).

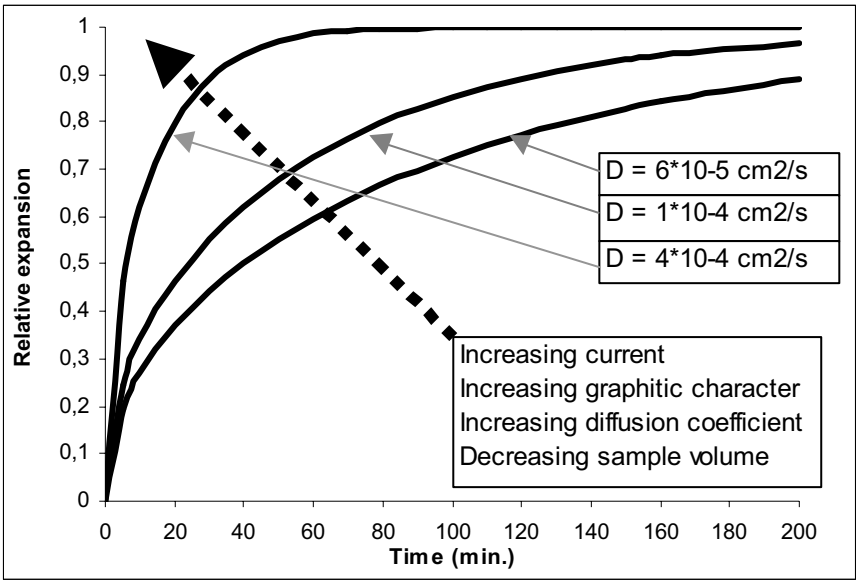

Figure 4.31. Summary sketch of relative sodium expansion with respect to time. The speed of the relative expansion is in this chapter shown to increase with current density, decreasing sample volume and graphite content.

4.2.6 Sodium expansion - penetration from bottom

The set-up shown in Figure 3.6 was used to measure the sodium expansion with sodium penetrating from the bottom of the sample. The current density was between 0.4 – 0.5 A/cm^2 and the only load was the thin steel rod resting on top of the sample. These samples were later sawed in slices and analysed for sodium (Chapter 4.3.2). As in the test for radial penetration (Rapoport – type apparatuses) the anthracitic material has the highest expansion and the semigraphitized material the lowest (Figure 4.32). It is also seen that the expansion rate of the semigraphitized material cease fast after approximately 10 minutes of electrolysis.

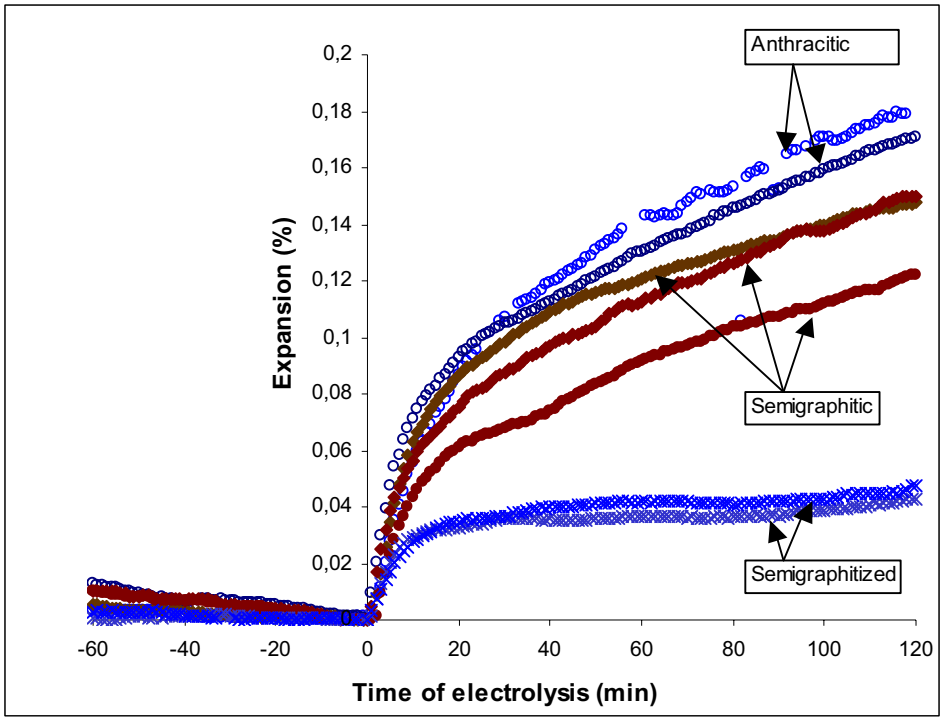

Figure 4.32. Sixty minutes of stabilisation and sodium expansions of the samples used for sodium concentration studies. The electrolysis starts at time = 0 minutes.

The expansion for the different materials is slower than measured with the Rapoport – type apparatuses. The surface exposed to the melt is smaller and the sodium penetration rate is reduced.

4.2.7 Sodium expansion - modelling

If the penetration of sodium in carbon is assumed to be a diffusion process and the concentration of sodium is proportional to the sodium expansion the measured expansions could be fitted to Fick's 2nd law as described in Chapter 2.2.3. Some assumptions in addition to grain boundaries and electric field are explained:

Homogenous, isotropic material:
As seen from the pictures of the structures (Chapter 4.1) the materials contain large pores and cracks. The materials consist of at least two different materials. The anthracitic material contains three materials; anthracite (70 %), graphite (30 %) and binder. The grains have sizes from dust to one centimetre and large parts of the material consist of grain boundaries. As the basic structure of the carbon materials is based on graphene layers the materials exhibit anisotropy.

Constant start concentration on the surface:
As sodium enters the sample some sodium will be lost from the electrolyte and the activity of sodium could be reduced during an experiment. The electrolyte volume in the experiments is from 450-760 grams and contains at least 150 grams sodium ions. In the sodium absorption experiments of Mikhalev and Øye [19] the material absorbing most sodium had a weight increase of approximately 5 %, which gives a sodium content of only 3.25 g in the sample, so the loss of sodium from the electrolyte is a minor error. The sodium concentration on the surface is probably constant and determined by the current density on the cathode (Eq. 2.4).

Sodium expansion proportional to sodium concentration:
Liao and Øye [49] measured the sodium content in samples exposed to electrolysis in a Rapoport test like used here. They found a linear relation between sodium expansion and sodium content in an anthracitic cathode material. The melt was sometimes over-saturated with alumina (which could influence the sodium content analysis, see Appendix A).

Mikhalev and Øye [19] compared sodium absorption measurements with sodium expansion data from Schreiner and Øye [44] and found a non- linear relation. This comparison was made between different materials and as explained in Chapter 2.1, sodium may be absorbed by different mechanisms and the amount of sodium causing expansion might be different in different materials.

Diffusion mechanism:
As discussed in Chapter 2.2.1, the diffusion mechanisms might be gas diffusion, grain boundary diffusion or lattice diffusion. The diffusion coefficient and ability to absorb sodium is probably different in the grains (anthracitic, graphitic and petrol coke), binder and grain boundaries. The reflections of the hydrodynamic-like mechanism proposed by Herold [26] could also be regarded.

But despite the different carbons with their different grain and pore structure the expansion curves look similar. The heat treatment temperature of the material will be shown to affect the diffusion coefficient more than the difference in grains and pores. This is particularly seen in the laboratory produced material, which looks similar on the macro level (Figure 4.12) but are different on the crystal level (different d_{002} - values, Figure 4.16). The composition is the same, the only difference is the heat treatment temperature and an increased degree of ordering on the nano-level.

The calculated diffusion coefficient represents the major diffusion mechanism or an average of more than one mechanism and are based on similar assumptions as the before reported diffusion coefficients summarised in Table 1.1.

The solutions for Fick's 2nd law for diffusion into a semi – infinite medium (Eq. 2.15) and diffusion into a cylinder (Eq. 2.19) are shown in Chapter 2.2.3. Only relative mass, total mass and the size of the sample are needed in these solutions. The value for the diffusion coefficient determines how fast the curve increases.

Measuring point on top of the cylinder
The dependence of the measuring points on the cylinder influences the expansion curve (Figure 4.19). The measured expansion at different measuring places is compared with numerical solutions [72] of the expansions in Figure 4.34. With some scatter it is seen that the experimental and numerical results show as expected that the middle part of the sample expands slower. The numerical results [72] are calculated with $D = 1.86 \cdot 10^{-4}$ cm^2/s. The solution for Fick's law used here (Eq. 2.19) is plotted with the solution for the two extreme conditions (centre and periphery) in Figure 4.33. The plot of Eq. (2.19) is closer to the calculated periphery expansion, which is the measuring point in most of the modelled data.

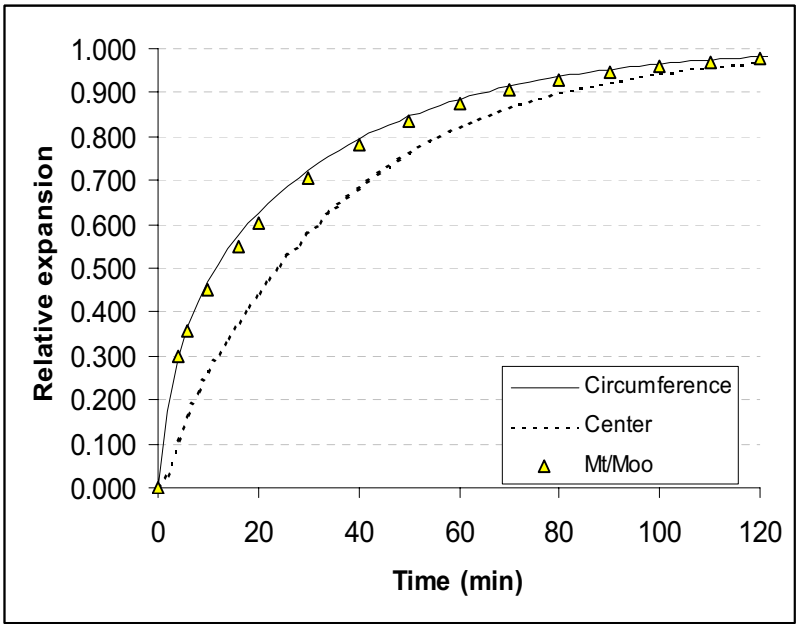

Figure 4.33. Numerical results for the expansion of the circumference and centre points of a Ø3 cm cylinder (replotted from [72]). The solution for Fick's law for relative mass (M_t/M_∞, Eq. 2.19) is shown for comparison. A diffusion coefficient of $1.86 \cdot 10^{-4}$ cm^2/s is used in the calculations.

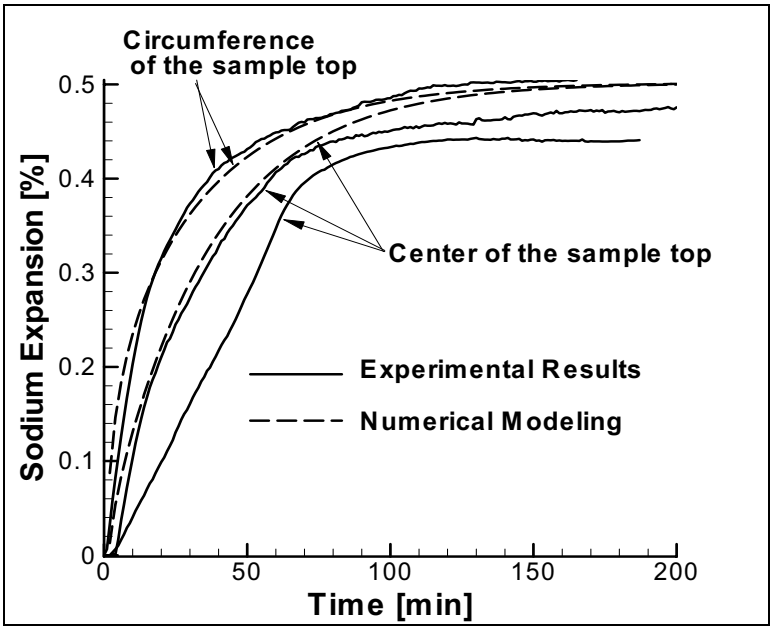

Figure 4.34. Numerical results for the difference in expansion in the middle and circumference position of the sample. Within some scatter it is seen that the centre of the sample expands slower ($D = 1.86 \cdot 10^{-4}$ cm^2/s, [72]).

The expansion of the semigraphitic material at small pressures (Figure 4.22) is plotted as relative expansion in Figure 4.35 (solid cylinder, 2.3 MPa) and in Figure 4.36 (hollow cylinder, 0.15 MPa). The respective solutions of Fick's 2nd law (Eq. 2.19 and 2.21) are plotted and it is seen that the diffusion coefficient increases with increasing current density. The diffusion coefficient increases from approximately $0.4 \cdot 10^{-4}$ cm^2/s to $5 \cdot 10^{-4}$ cm^2/s at current densities from 0.06 to 0.7 A/cm^2.

From Eq. (2.21) a hollow cylinder should saturate faster than a solid cylinder, which was found (Figure 4.22). The diffusion coefficients should be independent of the sample geometry but the D is slightly higher for the solid cylinder (Figure 4.35) than for the hollow (Figure 4.36). This is probably due to the creep of the sample (as measured in Chapter 4.4):

When the sample is exposed to 2.3 MPa pressure (which the solid cylinders are) a given creep strain will work in the opposite direction of the sodium expansion. When the two strains (sodium expansion and creep) has the same strain per time unit, the sample will appear not to expand anymore, when in reality the sample expands because of sodium, and shrinks because of compressive creep. The magnitude of this error will increase with (in experiments with pressure):

-Increasing pressure
-Longer time to saturation (low current density)
-Lower total sodium expansion (more graphitic material)

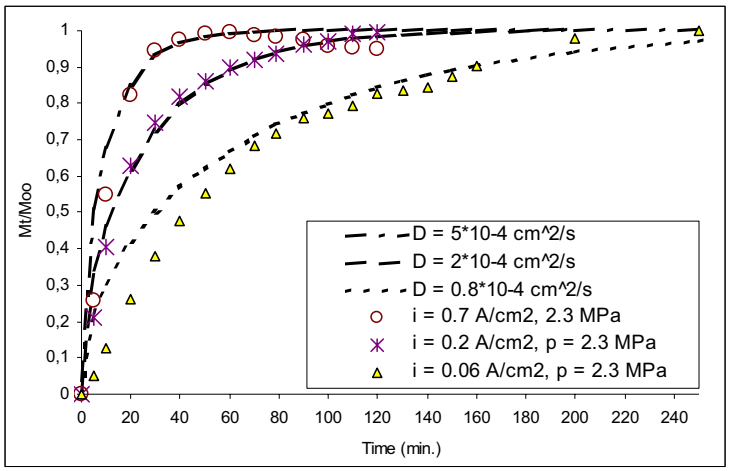

Figure 4.35. Relative expansion in semigraphitic solid cylinder at different current densities.

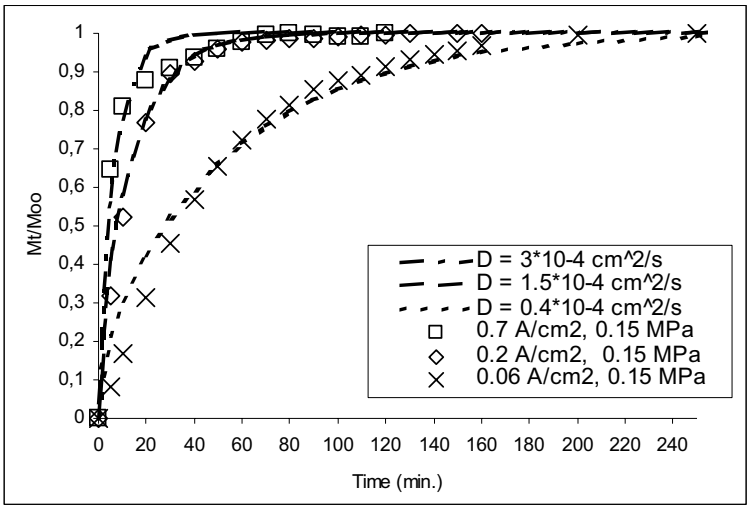

Figure 4.36. Relative expansion in semigraphitic hollow cylinders at different current densities.

Støre et al. [46] measured the sodium expansion at current densities from 0.05 to 0.88 A/cm^2 in the same cathode blocks as used here. The experimental set-up and conditions were the same as described in Figure 3.3 with a pressure of 5 MPa in all experiments. It is seen from Figure 4.37 (anthracitic material), Figure 4.38 (semigraphitic material) and Figure 4.39 (semigraphitized material) that the experiments with a higher pressure give a poorer fit to the solution for Fick's law. In the creep measurements (Chapter 4.4) the creep rate is largest in the beginning of the experiments and this is the part that gives a poor fit here. For the lowest current densities (0.2 A/cm^2 and 0.05 A/cm^2) the creep strain will influence more as the experiments are longer.

In the Figures presented below, three diffusion coefficients are plotted in each graph: $1 \cdot 10^{-4}$, $2 \cdot 10^{-4}$ and $5 \cdot 10^{-4}$ cm^2/s. The higher the diffusion coefficient is, the faster the curve increase. All curves within one material at current densities above 0.2 A/cm^2 coincides and are shown with lighter symbols. Only the measurements at 0.05 and 0.2 A/cm^2 separates and are plotted in darker, more visible symbols.

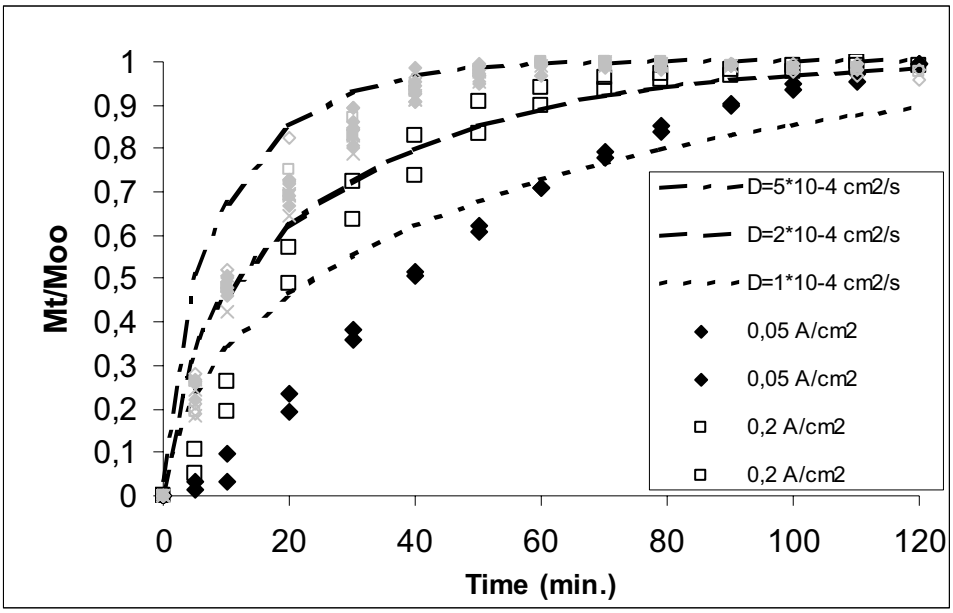

Figure 4.37. Relative expansion in anthracitic material at different current densities.

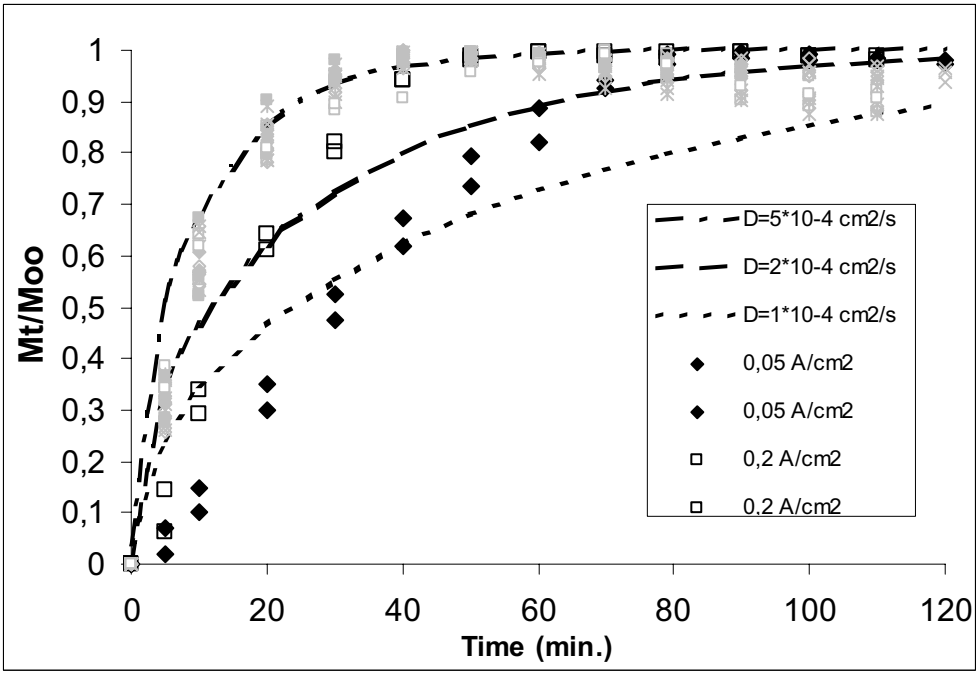

Figure 4.38. Relative expansion in semigraphitic material at different current densities.

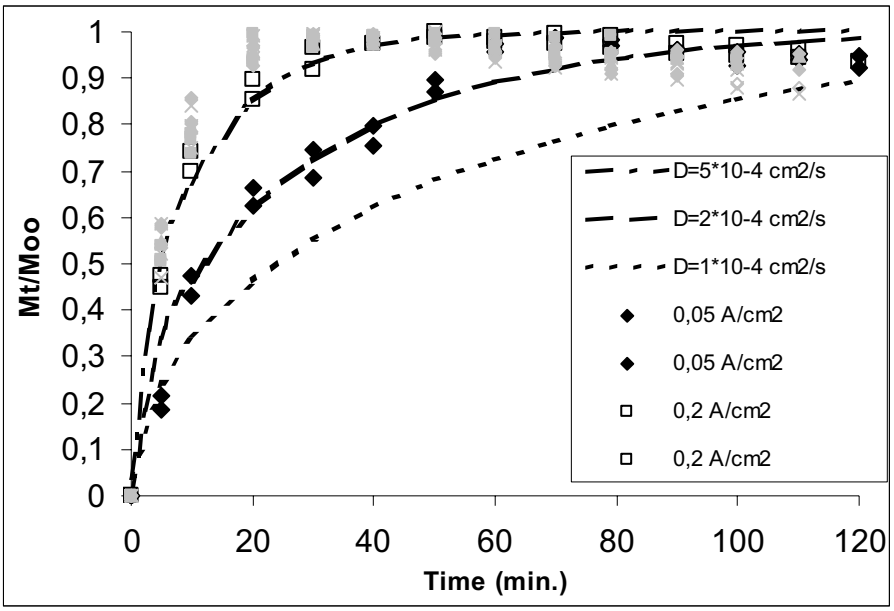

Figure 4.39. Relative expansion in semigraphitized material at different current densities.

Despite the poor fit in the experiments with 5 MPa pressure, some important trends are observed. In anthracitic (Figure 4.37) and semigraphitic material (Figure 4.38) the relative expansions overlap at current densities between 0.5 – 0.88 A/cm^2. This means that the diffusion coefficient is not dependent of the current density in this interval. For the semigraphitized material this limit seems to be at a lower current density as the measurements at 0.2 A/cm^2 overlap with the higher current densities (Figure 4.39).

In Figure 4.40 the relative expansion in semigraphitic material is shown at two cryolite ratios. As discussed in section 4.3.2 the relative expansion overlap for the two different CR's, and the diffusion coefficient is independent of the sodium concentration on the surface in this concentration interval.

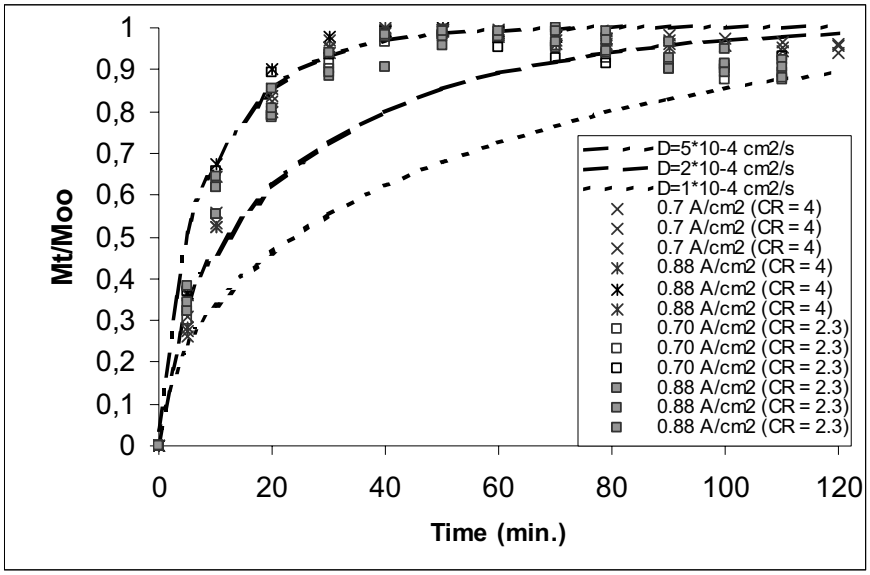

Figure 4.40. Relative expansion for semigraphitic material at two different CR's. The diffusion coefficient does not change within the measured cryolite ratio and current densities.

A summary of the all the measured diffusion coefficients (D) is presented in Figure 4.41 and Figure 4.42. The coefficients are for simplicity calculated by using the time to half expansion (Eq. 2.20). The calculated D's versus current density are shown in Figure 4.41. D is probably constant above a current density between 0.2 – 0.5 A/cm^2. Within this interval (0.2 A/cm^2 – 0.5 A/cm^2) the more graphitic material seems to reach a constant D closer to 0.2 A/cm^2 than the less graphitic materials. In Figure 4.42 the diffusion coefficients are compared with the laboratory produced material heat treated to different temperatures at a current density of 0.2 A/cm^2. It is seen that the more graphitic materials and materials with higher heat treatment temperature have higher diffusion coefficients. The semigraphitic material consists of 80-90 % graphite. This seems to be of less importance for the diffusion coefficient as this material has only a slightly larger D than the anthracitic material. The bottleneck seems to be the binder phase which only has seen temperatures of approximately 1200 °C. Similar trends are observed for the laboratory produced material where the diffusion coefficient increases from a heat treatment of 1500 °C to 2000 °C.

The diffusion coefficient of sodium in semigraphitic material is as discussed before not dependent of concentration at $2.2 \leq CR \leq 4$. This corresponds to expansions of approximately 0.2 and 0.4 % respectively. The low D and

high expansion of the laboratory produced material heat treated to 1500 °C (2.5 %) could however be a result of concentration dependence, since much more sodium (higher concentration) has to enter this sample.

The diffusion coefficient of sodium in semigraphitized material (Figure 4.42) is larger than calculated in graphite with the same pressure. As graphite is more graphitic than the semigraphitized material a higher diffusion coefficient could be expected in graphite. The creep in the semigraphitized material might be larger and this, in combination with a small expansion could result in a too high calculated diffusion coefficient.

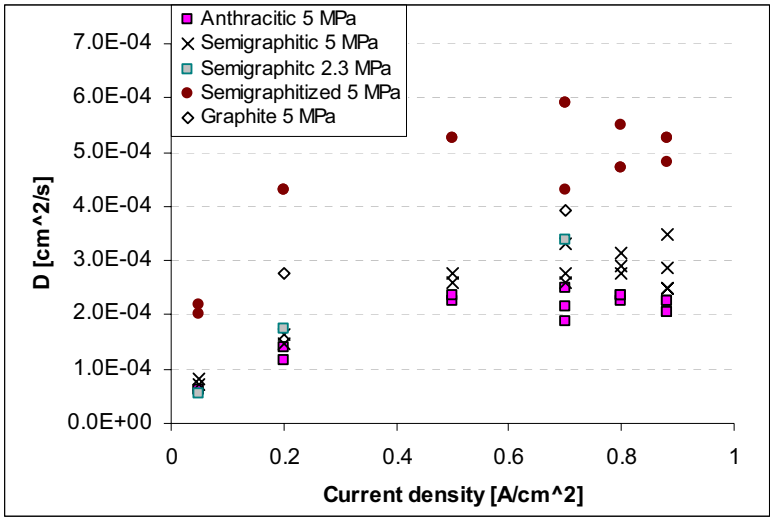

Figure 4.41. Diffusion coefficients calculated from the time to half expansion, Eq. (2.20).

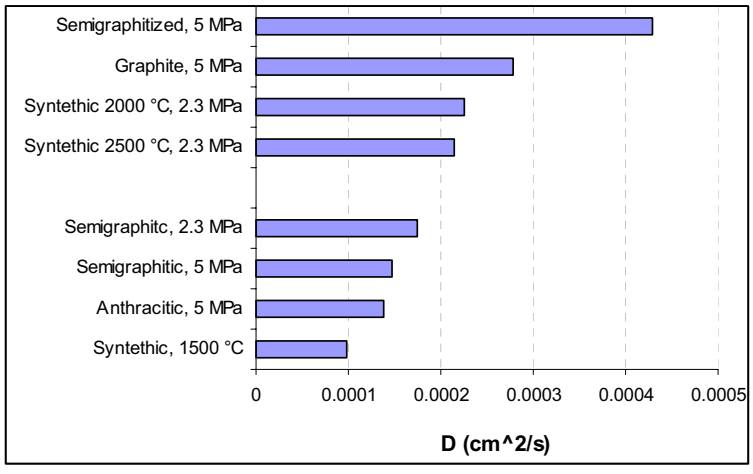

Figure 4.42. Comparison of calculated diffusion coefficients at with a current density of 0.2 A/cm^2 for all materials.

Possible explanation for the current density dependence

Graphite will in the following example be considered in an experiment with a current density of 0.2 A/cm^2. Sodium absorption in carbon is assumed to be determined by the current (electrochemically reduced). If the current efficiency for sodium reduction is assumed to be 100 %, a sodium concentration of approximately 3 % (in a 65 gram sample) would be produced after 12 minutes of electrolysis (Appendix E). From sodium concentration measurements in semigraphitized material exposed to sodium (Figure 4.46), and from measurements of sodium absorption at high temperature [19], the sodium content is below 0.5 % for a saturated sample, so another electrochemical reaction has to consume some of the current.

Aluminium and aluminium carbide in addition to impurities will also be reduced on the cathode. At lower current densities the formation of aluminium carbide (Al_4C_3) probably consumes the majority of the current. Gudbrandsen et al. [13] measured the formation of aluminium carbide up to 0.2 A/cm^2 in graphite. Above a current density of 0.10 A/cm^2 the aluminium carbide production did not increase and below 0.10 A/cm^2 the current efficiency for aluminium carbide was about 80 %. The additional current was explained as reduction of sodium and impurities.

This probably means that at lower current densities the formation of aluminium carbide will compete with the reduction of sodium. At higher current densities there will be current in excess and sodium can diffuse with high speed as with current densities above 0.2 A/cm^2 (for graphite).

If aluminium carbide consumes 0.10 A/cm^2 of the conducted 0.20 A/cm^2, this leaves 0.10 A/cm^2 for formation of sodium in carbon. In Figure 4.43 the calculated sodium production at 0.10 A/cm^2 is shown as a straight line.

If the sodium concentration at saturation in graphite is 0.5 % (Figure 4.46**,** from sodium vapour test) and the sodium concentration increases proportional with the expansion, the sodium production will increase as shown in Figure 4.43. The sodium expansion curve in Figure 4.29 is simply made relative to 0.5 %.

The assumed sodium production coincides with the uptake in the sample in the beginning of the electrolysis. After 5 minutes the diffusion coefficient of sodium in graphite controls the absorption rate and aluminium production might take place. At a current density lower than 0.2 A/cm^2, more of the

current is consumed by aluminium carbide and a slower expansion would be achieved.

In the paper of Gudbrandsen et al. [13] graphite was the only studied material. In more amorphous materials the reduction to aluminium carbide could go faster and the production of aluminium carbide could consume more current. This will give less current left for the production of sodium and a resulting slower expansion.

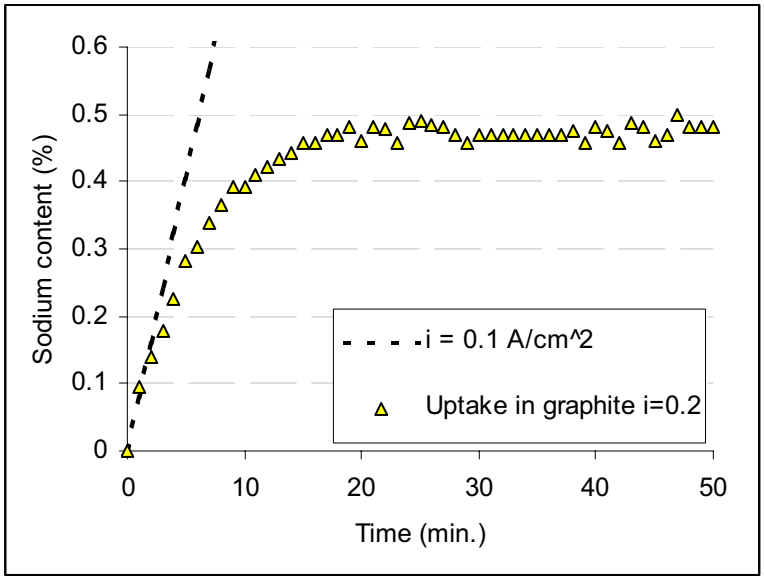

Figure 4.43. The theoretically sodium production with 0.1 A/cm^2 is shown with a straight line. The triangles are based on the sodium expansion curve of graphite with 0.2 A/cm^2 in Figure 4.29. The concentration is assumed proportional with the expansion and made relative to 0.5 %. Aluminium carbide is assumed to consume 0.1 A/cm^2 of the 0.2 A/cm^2.

Another way to explain the increasing D for increasing current density could be the electrical field formed in the cathode when the current is conducted through the sample as discussed in Chapter 2.2.1. Electric fields are reported to increase the diffusion coefficient [27, 36, 37] and could directly explain the current dependency of the D.

The connection between the current dependency and the diffusion coefficient is not certain. Similar experiments in a NaCl melt (only sodium can be reduced on/in the cathode) at different current densities could probably give valuable information for the diffusion coefficient.

Modelling of penetration from the bottom

The penetrated mass should be linear with the square root of time for diffusion into a semi-infinite medium (Eq. 2.15). To regard the sample as semi – infinite, the sample has to be longer than the penetration distance of sodium. The time for sodium to penetrate the sample is between 30 – 60 minutes for the semigraphitic material (Chapter 4.3). The accepted time must therefore be below 60 minutes for this material to be regarded as semi-infinite. As shown in the previous section, the semigraphitized material has an even faster penetration and a shorter accepted time must be used.

In the expansion measurements for the semigraphitized material (Figure 4.32) the expansion rate is markedly reduced after 10 minutes of electrolysis and continues at a smaller rate. This indicates that sodium reached the other end of the sample in a shorter time, and 20 minutes are used as maximum time for the semigraphitzed material.

All the expansions are too low in the start, and too high at some intermediate time compared to the model (Figure 4.44). In the beginning of the experiments it may take some time before sodium reach a steady start concentration and the first measurement will be low. The reason for the decreasing slope after some intermediate time could be that sodium has penetrated the sample and the material can not be considered as semi – infinite any more. The poor fit could also be caused by a systematic experimental error. The expansions measured here are small and small disturbances will influence the measurements. The temperature effect explained in section 4.2.1 will also contribute. However, as will be shown the modelled D's are comparable to the calculations for the radial penetration.

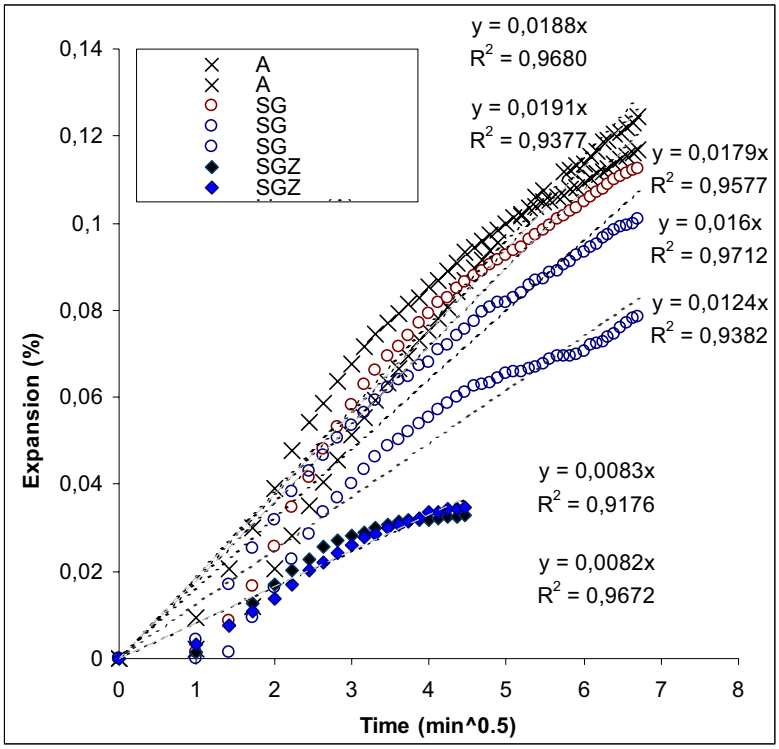

Figure 4.44. Fitting straight lines with the square root of time to Eq (2.15) for the data presented in Figure 4.32. Abbreviations: A:Anthracitic, SG – semigraphitic, SGZ – semigraphitized.

The diffusion coefficient can be calculated if the penetrated mass and the start concentration is known (Eq. 2.15). The sodium expansion at $t = \infty$, ε_s^{∞}, is proportional with the start concentration C_0 with the proportional constant A (Eq. 4.1). The values for saturation expansion (ε_s^{∞}) are average expansions taken from the creep experiments in Chapter 4.4 (CD = 0.2 A/cm^2, without pressure).

$$\varepsilon^{\infty}_s = C_0 \cdot A \qquad (4.1)$$

The total penetrated sodium concentration at a given time is the product of the average sodium concentration and the total length of the sample, (l = 6 cm):

$$M(t) = C \cdot x = \varepsilon_s \cdot (1/A) \cdot l \qquad (4.2)$$

If these equations are put into Eq. (2.15) and rearranged the expression in Eq. (4.3) is achieved. The expression in front of the square root of time is equal to the slopes from Figure 4.44 and is termed *k*.

$$\varepsilon_s = \frac{\varepsilon_s^{\infty} \cdot 2}{l}\sqrt{\frac{D}{\pi}} \cdot \sqrt{t} = k \cdot \sqrt{t} \qquad (4.3)$$

The slopes of the curves, *k*, in Figure 4.44 and the calculated diffusion coefficients are presented in Table 4.2. The diffusion coefficient is calculated by Eq (4.4).

$$D = \left(\frac{k \cdot l}{\varepsilon_s^{\infty} \cdot 2} \right)^2 \cdot \pi \qquad (4.4)$$

Table 4.2. Diffusion coefficients calculated from Eq (4.4).

	k [%/min$^{0.5}$]	k [%/s$^{0.5}$]	ε_s^{∞} [%]	Calculated D [cm^2/s]
A	$1.88 \cdot 10^{-2}$	$2.43 \cdot 10^{-3}$	0.58	$4.95 \cdot 10^{-4}$
A	$1.91 \cdot 10^{-2}$	$2.47 \cdot 10^{-3}$	0.58	$5.11 \cdot 10^{-4}$
SG	$1.79 \cdot 10^{-2}$	$2.31 \cdot 10^{-3}$	0.46	$7.13 \cdot 10^{-4}$
SG	$1.60 \cdot 10^{-2}$	$2.07 \cdot 10^{-3}$	0.46	$5.70 \cdot 10^{-4}$
SG	$1.24 \cdot 10^{-2}$	$1.60 \cdot 10^{-3}$	0.46	$3.42 \cdot 10^{-4}$
SGZ	$8.30 \cdot 10^{-2}$	$1.07 \cdot 10^{-3}$	0.16	$1.27 \cdot 10^{-3}$
SGZ	$8.30 \cdot 10^{-2}$	$1.07 \cdot 10^{-3}$	0.16	$1.27 \cdot 10^{-3}$

The calculated diffusion coefficients are 2 – 2.5 times larger than calculated from radial diffusion. The explanation for this could be the orientation of the sample (all samples are taken out in the extrusion direction of the block). When sodium penetrates from bottom this is perpendicular to the penetration direction of the Rapoport - like apparatuses. The diffusion coefficient is probably different in these two directions and sodium probably penetrates easier parallel to the extrusion direction. The carbon sheets (on atom level) have a larger degree of orientation in the extrusion direction than perpendicular to this (Figure 1.3).

Comparison with other diffusion coefficients (Table 1.1)

Naas [30] measured sodium expansion of cathode materials with different additions of alkali in the electrolyte and calculated diffusion coefficients in the range 0.4-1.2·10^{-5} cm^2/s. The expansion was assumed to be proportional to the sodium concentration, the same assumption as here, but the expansion - time curve was fitted to the solution of Fick's law for diffusion into a semi – infinite slab, and not radial diffusion which is the case for the Rapoport specimen. The distance (*x*) and diffusion coefficient (*D*) was multiplied with

a value k_d. The distance x was chosen as a constant, so-called effective penetration depth and the equation for fitting was found to be:

$$\varepsilon(x,t) = A' c_{sat}\left(1 - erf(\frac{x}{2\sqrt{Dt}})\right) = A' c_{sat}\left(1 - erf(k_d)\right) \qquad (4.5)$$

It seems more likely that this model predicts the concentration at the given distance x during time. If the expansion data of Naas [30] is studied in detail, the samples saturate at similar time as measured here, and the D is in the same range.

Øye et al. [35] calculated D = $6.3*10^{-5}$ cm^2/s based on the sodium consumption of the cathode (addition of soda to the bath) in full-scale industrial cells. The solution for Fick's 2nd law for diffusion into a semi – infinite material was used. When the addition of aluminium fluoride was constant with time, the cathode was assumed to be saturated with sodium. At this time the concentration on the cathode bottom was assumed to be 10 % of the concentration on the top of the block. If a concentration of 50 % sodium is assumed in the bottom at this time, a diffusion coefficient of $4\cdot10^{-4}$ cm^2/s is calculated.

The diffusion coefficient calculated from data from Houston et al. [31] was based on the penetration depth of the observed sodium front. An estimate of the apparent diffusion coefficient was evaluated using approximations to the diffusion equation and coefficients around $0.9\text{-}2.9\cdot10^{-5}$ cm^2/s were calculated. The calculations were not reported here, as is the case when other D's are reported (Table 1.1), but some assumptions for the concentrations must be made.

Peyneau [43] studied the expansion with and without pressure in larger samples with diameters of 4 cm (without pressure) and 6 cm (with 3 MPa pressure). In Figure 4.45 the solution of Eq. (2.19) with Ø4 and Ø6 are plotted (D = $1\cdot10^{-4}$ cm^2/s) together with the measurements. The samples (ECA) were studied in a slightly acidic melt with a current density of 0.6 A/cm^2. It is seen that the curve for the pressurised Ø6 cm samples has a poor fit. In the measurements the measuring pins in the Ø4 cm sample were 0.9 cm from the melt, and in the Ø6 cm experiment 1.9 cm from the melt. This means that the response of the Ø6 sample will be more delayed and a slower expansion measured.

A larger sample will need a longer time before saturation. This means that the sample is exposed to stresses for a longer time and a larger creep strain

is achieved. The rather large reduction of expansion with a pressure of 3 MPa (compared to Schreiner [44], Guilliat [51] and here) might be the longer experimental time and a resulting larger creep strain.

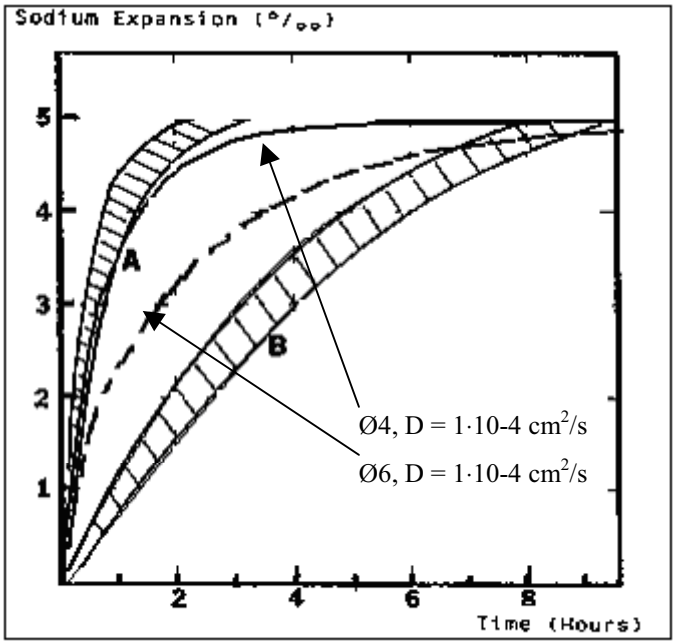

Figure 4.45. Fitting a diffusion coefficient of $1 \cdot 10^{-4}$ cm^2/s to the expansion curves of Peyneau [43]. The hatched areas A shows parallels with a sample diameter of Ø4 cm and B with samples with Ø6 cm (3 MPa pressure).

4.3 Sodium content

As described in the experimental part, the samples for sodium analysis were crushed in a swing mill and treated in 0.1 M HCl. After some reaction time 25 ml samples were backtitrated with 0.1 M NaOH. The amount of sodium was determined by the increase in alkalinity due to the reaction between sodium metal and water.

$$Na(s) + H_2O\,(aq) = Na^+(aq) + OH^-(aq) + \tfrac{1}{2}\,H_2(g) \qquad (4.6)$$

In the electrolysis experiments sodium will change the wetting conditions in the carbon and melt species will penetrate and react with the carbon cathode [3]. Species like Na_3AlF_6, NaF, CaF_2, α- and β-alumina ($Na_2O{\cdot}11Al_2O_3$) are found using X – ray diffraction in laboratory scale carbon cathodes [24, 30]. Unfortunately, most of the above mentioned species are soluble in either acidic or basic solutions and aluminium fluoride – complexes will form. Dissolved alumina was wanted to react back to $Al(OH)_3$ at the titration end point, and the amount of OH^- related to aluminium should be the same before and after the reaction with sodium. But as seen from the calculations in Appendix A, an unknown part of the aluminium is bound as AlF_4^- and AlF_3 complexes. At a given pH $Al(OH)_3$ do not necessarily dominate and the value of the pH where $Al(OH)_3$ is dominant depends on fluorine concentration (Appendix A). As a result, only samples without melt species are reported for the electrolysed samples.

4.3.1 Sodium content, sodium vapour test

Samples from the sodium vapour test contain only sodium and carbon and the above-described disturbance is not a problem and the titration end point is at pH = 7. The long reaction time reported earlier [52] was not measured in the samples exposed to sodium vapour. The reason for the long observed reaction time reported before might be the slow dissolution of alumina (Appendix A) and a wrong titration end point. Another reason could be that the sodium absorbed in the sodium vapour test is easier to extract.

The sodium content in the three commercial cathode materials after the sodium vapour test is plotted as a function of reaction time in acid in Figure 4.46. Sleepy [39] reported a reaction time of 12-18 hours before hydrogen evolution ceased in crushed samples that had been exposed to sodium vapour. As the first reaction time measured here was after 11 hours, the time for sodium in carbon to react with acid can only be stated to be below 11 hours.

The content of sodium in carbon found by weighing was larger than the amount found by backtitration. As the samples were weighed in air, some of the sodium metal will react to the heavier NaOH and/or Na_2CO_3 and a larger weight increase will be measured. Some of the difference could also be due to a part of the sodium that is more stable in carbon. Sleepy [39] found 30-50 % of sodium as non-reactive in acid after his sodium vapour experiments. The non-reactive sodium was found by ash analysis.

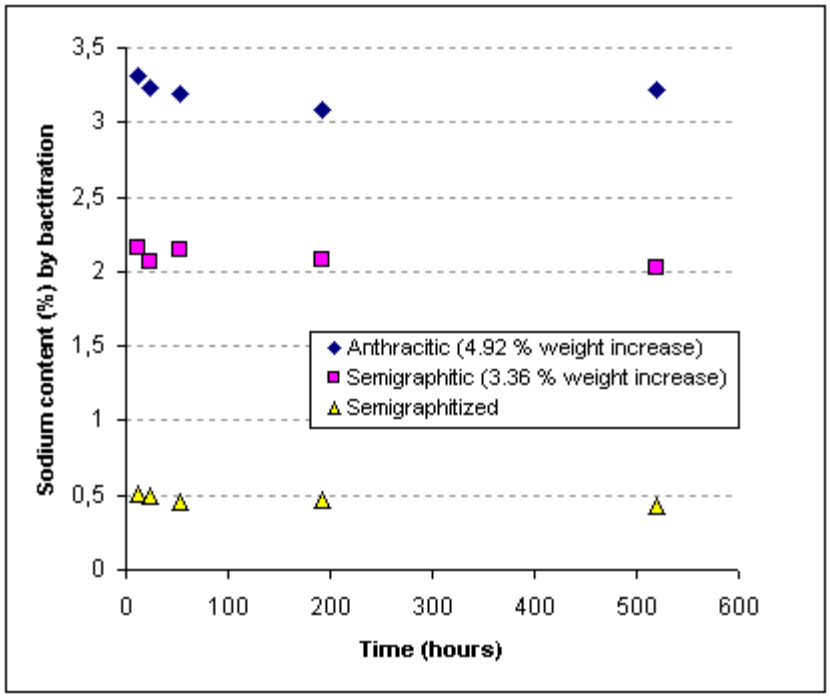

Figure 4.46. Sodium content versus reaction time in acid determined with backtitration.

4.3.2 Sodium content, cathode above electrolyte

All the samples electrolysed for 2 hours presented in Chapter 4.2.6 contained bath constituents and the sodium content measurements had to be rejected. But in some preliminary experiments with shorter electrolysis times some slices of samples taken a long distance above the melt did not contain melt species.

A cross section of a sample electrolysed for 30 minutes with the lower end dipped into the melt is shown in Figure 4.47. Next to the sample a filter

paper soaked in phenoftalein is shown. This paper had first been pressed against the sample surface. On top of the sample lies a universal indicator paper, which first has been wetted in water. The graph to the right shows the accepted sodium measurements in the upper part of the sample. It is seen that just above the observed sodium front the sodium content is 0.15 wt %. The negative value in the upper part of the sample is due to the experimental error during titration. One droplet of titrated 0.1 M NaOH corresponds approximately to 0.02 % in sodium concentration.

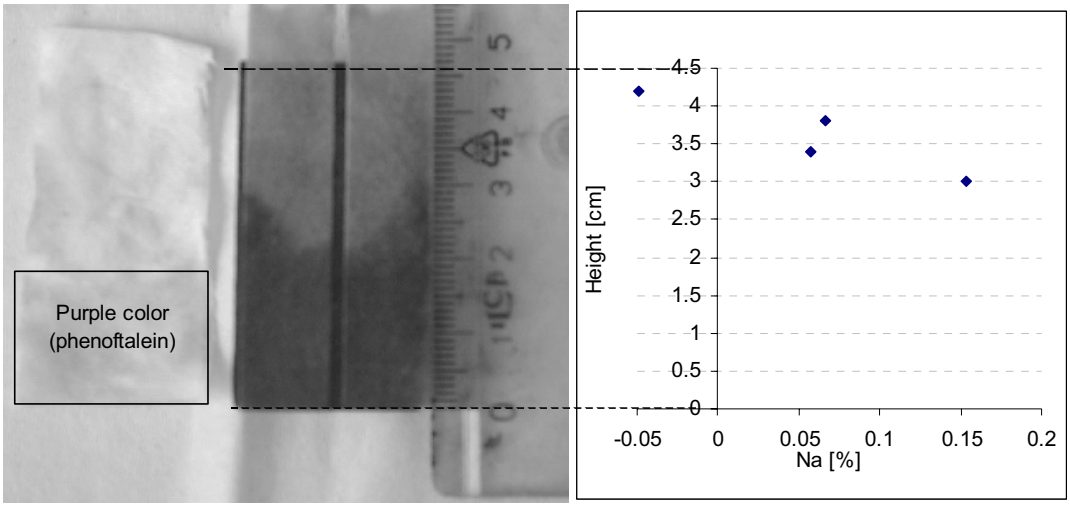

Figure 4.47. Filter paper soaked in phenoftalein (left), universal indicator (middle, on top of the sample) and measured concentrations (diagram to the right).

Eq. (2.13) is plotted together with the measured concentrations with a diffusion coefficient of $2.5 \cdot 10^{-4}$ cm^2/s in Figure 4.48(b). Only one point was accepted (sample without melt) in the sample electrolysed for 60 minutes. Four measurements in two parallel samples electrolysed for 30 minutes were accepted. The start concentration on the cathode surface is based on the concentration found after the sodium vapour test in semigraphitic material (2 %, Figure 4.46).

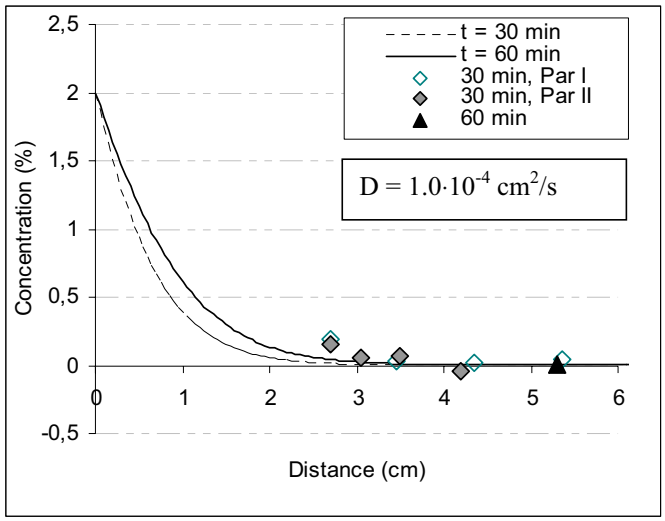

(a)

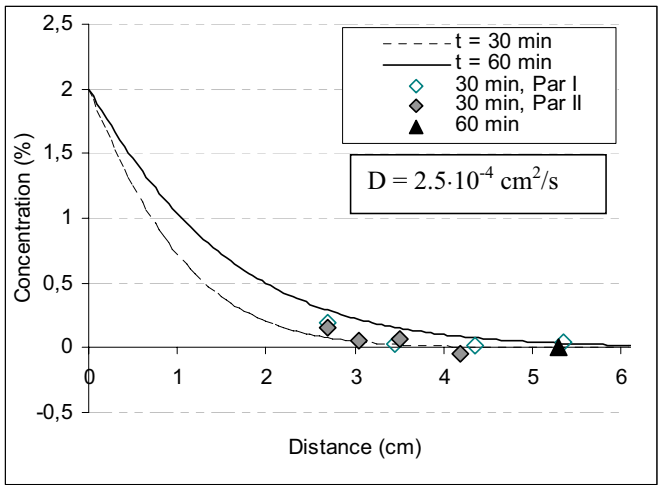

(b)

Figure 4.48. Sodium concentration profile in semigraphitic material with a current density of 0.5 A/cm^2 after 30 and 60 minutes of electrolysis. Only one concentration is measured at 60 minutes. Figure (a) shows calculated concentration profiles with $D = 1.0 \cdot 10^{-4}$ cm^2/s and Figure (b) shows calculated concentration profiles with $D = 2.5 \cdot 10^{-4}$ cm^2/s.

The data points to fit a concentration gradient are rather few, but as seen from Figure 4.48(a) D = $1.0 \cdot 10^{-4}$ cm^2/s is too small for the measured data as the concentration profiles goes too fast to zero.

4.3.3 Sodium content, cathode under electrolyte

The apparatus where the melt was located above the cathode with the sodium penetrating downwards is shown Figure 3.7. The accepted results are shown in Figure 4.49. The fitted lines are concentration profiles

calculated with a diffusion coefficient of $2.5 \cdot 10^{-4}$ cm^2/s and a start concentration of 2 % (same values as in the previous section). It is seen that for the two electrolysis periods the plotted concentration profile go through the measured points.

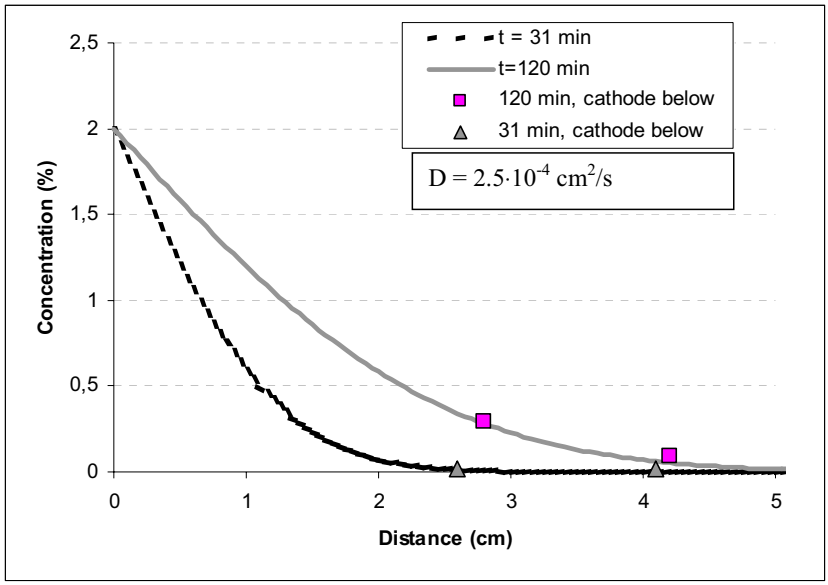

Figure 4.49. Measured sodium concentration in cathode samples located below the electrolyte (4 points). The sodium concentration is calculated with a D $=2.5 \cdot 10^{-4}$ cm^2/s and a start concentration of 2 % at the two times (t = 31 and t = 120).

The concentration profiles were not achieved due to the melt compounds in the samples. The fitting of the diffusion coefficient is based on rather few points but a value around $2.5 \cdot 10^{-4}$ cm^2/s seems in good agreement with the values found in Chapter 4.2.7. The location of the cathode does not seem to influence the measurements. When the cathode is located below the melt, reduced aluminium is on top of the sample, possibly reducing the sodium start concentration. But from the experiments up to 2 hours, the penetration seems to have the same speed.

4.4 Creep and E – modulus

The set-up described in Figure 3.8 was used to measure creep, E – modulus and in some instances the crushing strength at 25 °C, 980 °C and during electrolysis at 980 °C. Under each experimental condition, in most cases, two experiments were performed on the three commercial cathode materials.

The results are presented in similar graphs for the different materials. The total strain (elastic-, inelastic- and creep - strain) and the stress strain diagrams are presented as explained in the experimental part (Figure 3.9 and Figure 3.10 respectively). The creep curves can sometimes be hard to distinguish so an explanation of the presented creep strain graphs is shown in Figure 4.50. The negative strains are measured with a loaded sample (creep strain), and are increased with 5 MPa as one moves down the diagram. In some cases only one load is applied.

The positive strains are creep recovery and show the expansion of the sample after the pressure is relieved. The creep recovery is larger with increased load. The creep recovery is only shown for the electrolysis experiments as the small recovery in the other experiments was highly influenced by the creep recovery of the apparatus (Figure 3.15).

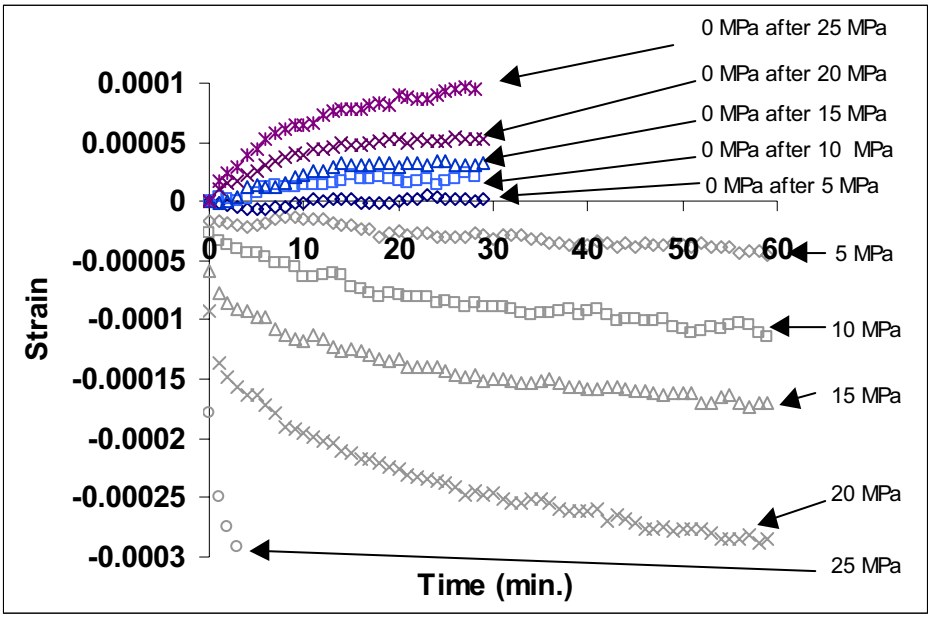

Figure 4.50. Explanation for the presented creep strain curves.

The stress – strain diagrams are not corrected for the elasticity of the boron nitride disk (Figure 3.14). The corrected E – modulus is presented in Figure 4.82 where the observed E - modulus of the loading to 10 MPa in each stress – strain diagram is used to calculate the real modulus (Eq. 3.1 and Eq. 3.2).

The reported values are not corrected for the creep of the boron nitride disk below the sample. The creep strain and creep recovery of this disk was ± 0.00003 at 20 MPa (Figure 3.15), so in the worst case the smallest creep strains at 25 °C is up to 30 % wrong for the smallest creep strains. In all experiments at 980 °C and during electrolysis, this value is in the worst case 1/10 of the measured creep strain.

The scatter was in general large as is expected from rather inhomogeneous materials and the creep strains at 10 and 15 MPa were of the same magnitude in the worst cases. But nevertheless, differences and trends are found between the materials and experimental conditions.

4.4.1 Creep and E - modulus, anthracitic material

The creep strain at 25 °C during the loading sequence is shown in Figure 4.51 (a) with the corresponding stress – strain diagram in Figure 4.51 (b). The last applied pressure during the loading sequence (20 MPa) was held for approximately 900 minutes (Figure 4.52). The graphs for a parallel measurement, where the first applied pressure was 20 MPa, are also shown in Figure 4.52. In these Figures the creep strain and stress-strain from the loading sequence (at 20 MPa) are replotted for comparison. The curves coincide with some scatter and the creep strain is probably independent of the loading sequence, as the creep strain is the same whether 20 MPa is applied for the first time or not. It is seen that most of the creep strain of the measured 900 minutes occurs during the first 30 minutes.

Later it will be shown that the stress – strain diagram change for the other materials after the loading sequence. In the anthracitic material the curves do not seem to change and an almost linear relation between stress and strain is measured (Figure 4.52 (b)).

The creep strain and the corresponding stress – strain diagrams for two parallel anthracitic samples at 980 °C is shown in Figure 4.54 and Figure 4.55. The problem with the load cell described in the experimental is here

seen in the first loading (5 MPa) where a positive strain was measured the 10 first minutes. The total creep strain is approximately the same at 25 °C (Figure 4.51a) and 980 °C, but the creep rate seems larger at 980 °C. This is the only material with a lower E – modulus at 25 °C (Figure 4.54b at 25 °C and Figure 4.55b at 980 °C). This is also opposite of what is found by resonance frequency measurements in anthracitic material [53]. As seen from the total strain for the two parallels at 980 °C (Figure 4.53) a pressure of 20 MPa was held for a longer time for parallel 1.

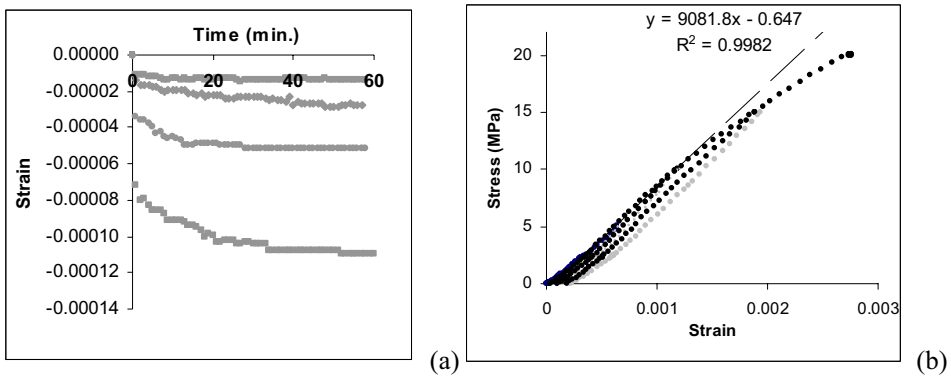

(a) (b)

Figure 4.51. Short time creep strain (a) and stress – strain diagram (b) for anthracitic material at 25 °C. The creep strain curves (a) show from top to bottom 5, 10, 15, and 20 MPa pressure.

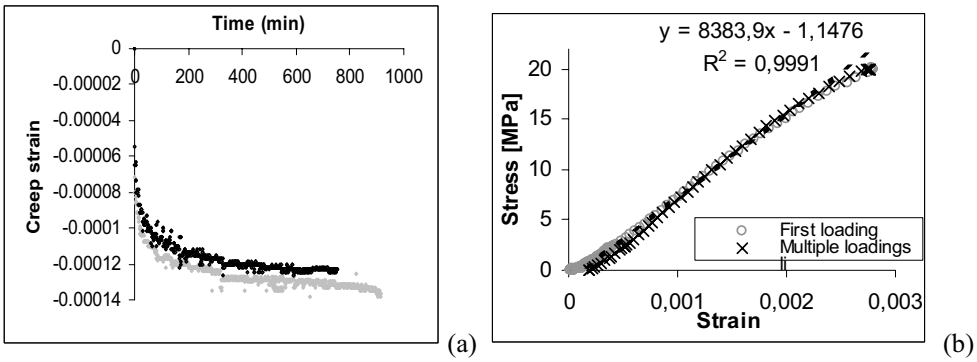

(a) (b)

Figure 4.52. Long time creep strain at 20 MPa (a) and stress – strain diagram (b) in anthracitic material at 25 °C. The darker symbols are re-plotted from Figure 4.51 for comparison and the curves in (b) overlap.

In Figure 4.56, Figure 4.57 and Figure 4.58 similar experiments are shown during electrolysis. The creep strain is several times larger (the scale of the creep strain axis is 5 times larger). The stress–strain diagram looks similar at 980 °C and during electrolysis. In the stress-strain diagram of the second parallel for the electrolysed anthracitic material (Figure 4.58) a large strain is measured at small loads. This could be due to the before discussed

uncertainties below 2.5 MPa or the sodium expansion could give a less flat surface. The pressure on the part of the surface that sticks out would be higher than on the rest of the surface, and the sample will be easier compressed at small stresses.

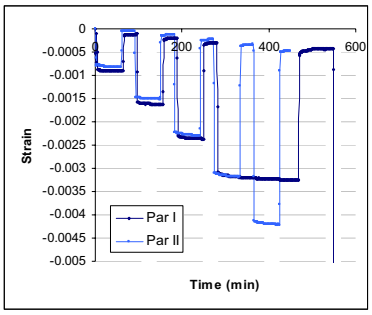

Figure 4.53. Total strain as a function of time in anthracitic material at 980 °C.

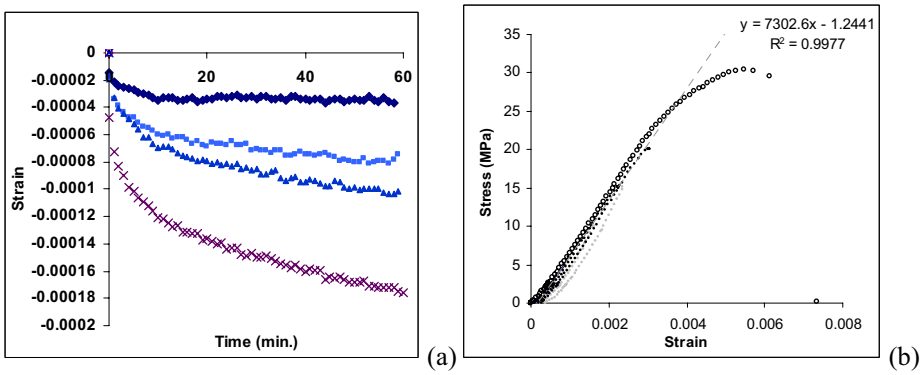

(a) (b)

Figure 4.54. Creep strain (a) and stress – strain diagram (b) for parallel 1 for anthracitic material at 980 °C. The creep strain curves show from top to bottom 5, 10, 15, and 20 MPa pressure.

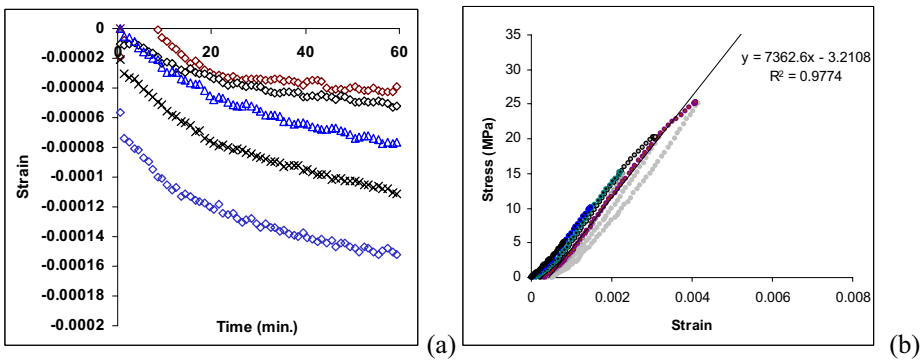

(a) (b)

Figure 4.55. Creep strain (a) and stress – strain diagram (b) for parallel 2 for anthracitic material at 980 °C. The creep strain curves from top to bottom: 5, 10, 15, 20 and 25 MPa pressure. The load cell as described in Chapter 3.7 influenced the loading to 5 MPa.

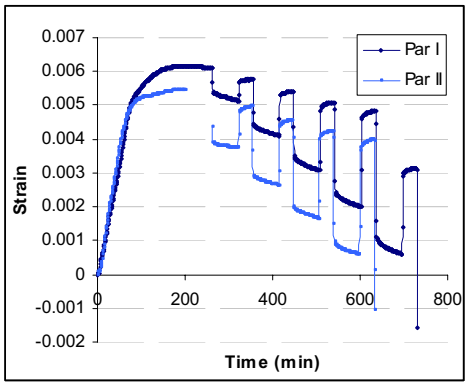

Figure 4.56. Total strain for the anthracitic material during electrolysis. The electrolysis starts at time zero. At ~250 minutes the loading cycle begins.

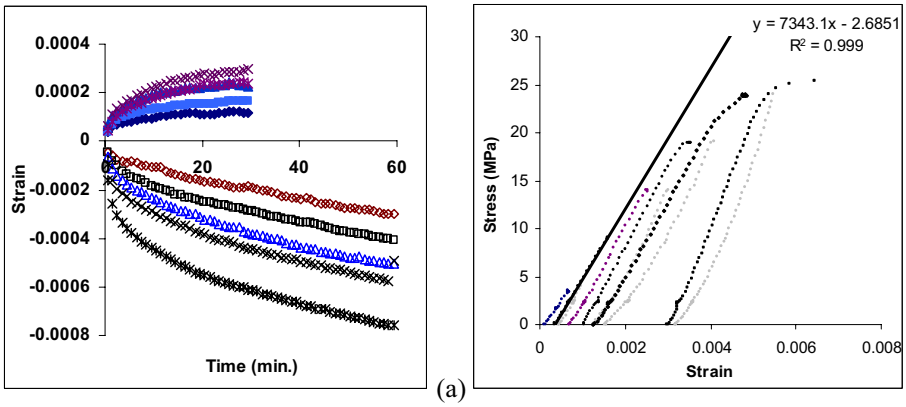

(a) (b)

Figure 4.57. Creep strain and recovery (a) and stress – strain diagram (b) for parallel 1 for anthracitic material at 980 °C during electrolysis. The curves in (a) show from top to bottom: Creep recovery after 25, 20, 15, 10 and 5MPa pressure and creep strain after 5, 10, 15, 20 and 25 MPa pressure.

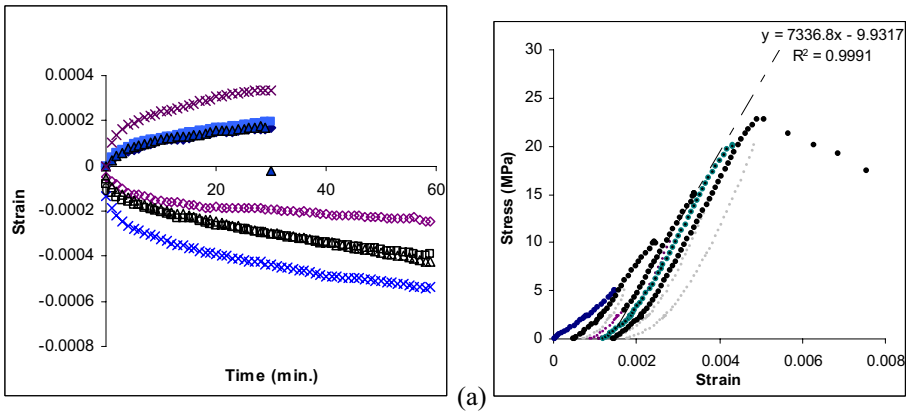

(a) (b)

Figure 4.58. Creep and creep recovery (a) and stress – strain diagram (b) for parallel 2 for anthracitic material at 980 °C during electrolysis. The curves in (a) show from top to bottom: Creep recover after 20, 15, 10 and 5MPa pressure and creep strain after 5, 10, 15 and 20 MPa pressure.

4.4.2 Creep and E - modulus, semigraphitic material

The creep strain at 25 °C during the loading sequence is shown in Figure 4.59 (a) with the corresponding stress – strain diagram in Figure 4.59(b). One sample crushed at 18.5 MPa in an attempt to reproduce the 20 MPa creep. In the next attempt the sample held and the creep is shown in Figure 4.60 (a). The stress – strain diagram for the crushed sample is plotted together with the sample that withstood the pressure in Figure 4.60 (b).

The creep strain at 20 MPa from the loading sequence (Figure 4.59 (a)) is plotted together with the creep measured with 20 MPa as the first pressure in Figure 4.60 (a). It is seen that the scatter is large, probably because the pressure was close to the crushing strength. The E – modulus of the sample exposed to loading sequence was larger (5.9 GPa) than measured in the other two samples (4.1 GPa).

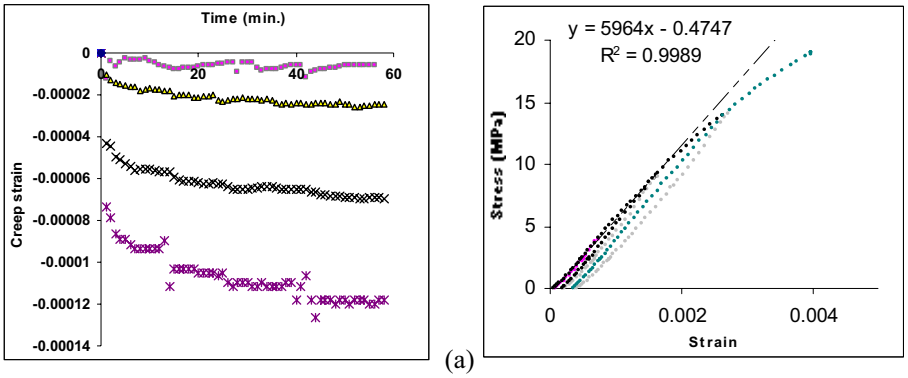

(a) (b)

Figure 4.59. Creep strain (a) and stress – strain diagram (b) for semigraphitic material at 25 °C. The creep strain curves (a) show from top to bottom: 5, 10, 15 and 20 MPa pressure.

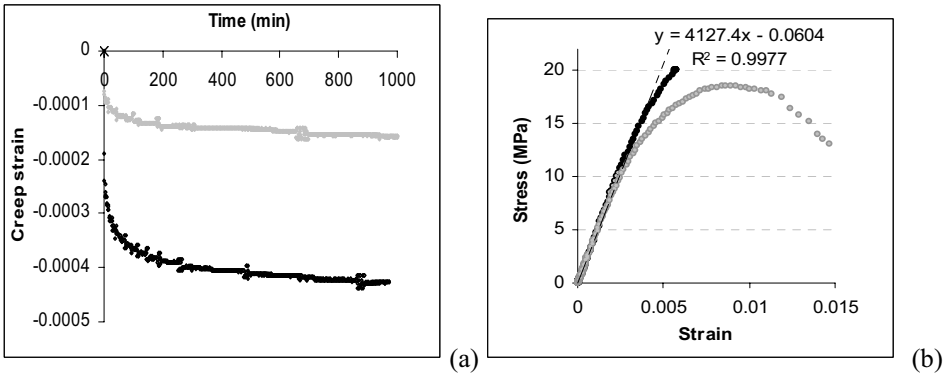

(a) (b)

Figure 4.60. Creep strain (a) and stress – strain diagram in semigraphitic material at 25 °C. The lighter dots for in Figure (a) are re-plotted from Figure 4.59 (a) for comparison. The lighter dots in (b) show the sample that crushed at 18.5 MPa.

The total strain, creep strain and stress – strain diagrams at high temperature are shown in Figure 4.61, Figure 4.62 and Figure 4.63 respectively. The similar measurements during electrolysis are shown in Figure 4.64, Figure 4.65, and Figure 4.66.

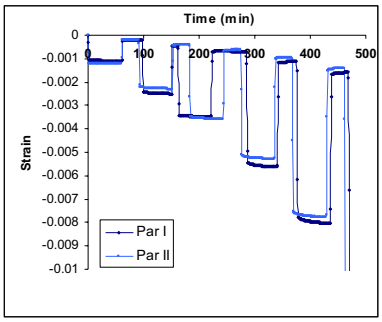

Figure 4.61. Total strain of 2 parallels in semigraphitic virgin materials at 980 °C.

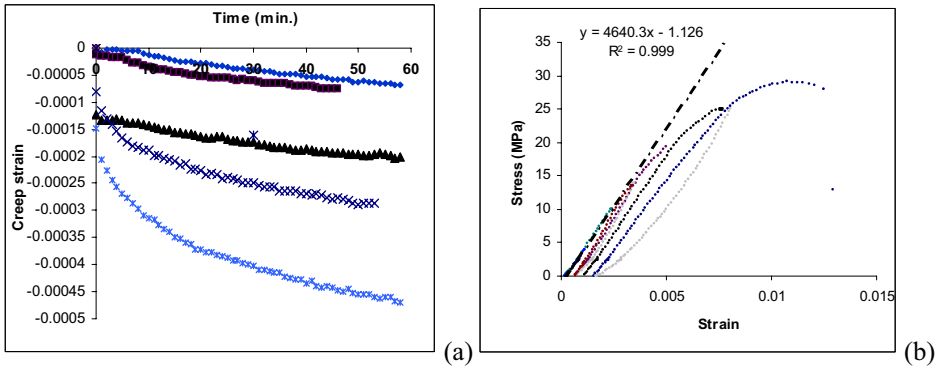

(a) (b)

Figure 4.62. Creep strain (a) and stress – strain diagram (b) for semigraphitic material at 980 °C. The creep strain curves (a) show from top to bottom: 5, 10, 15, 20 and 25 MPa pressure. The load cell as described in Chapter 3.7 influenced the loading to 5 and 15 MPa.

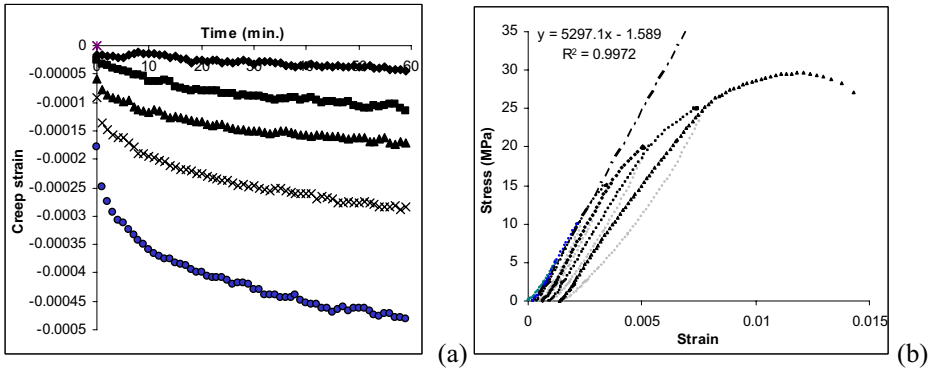

(a) (b)

Figure 4.63. Creep strain (a) and stress – strain diagram (b) for parallel 2 for semigraphitic material at 980 °C. The creep strain curves (a) show from top to bottom:5, 10, 15, 20 and 25 MPa pressure.

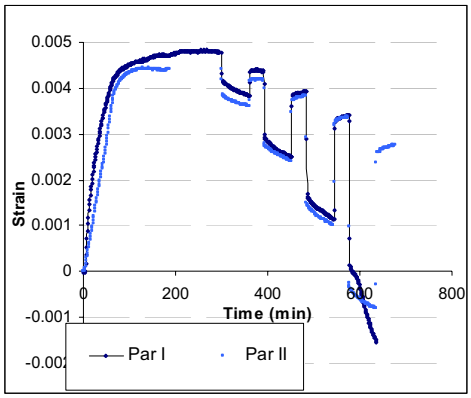

Figure 4.64. Total strain in the semigraphitic material at 980 °C during electrolysis.

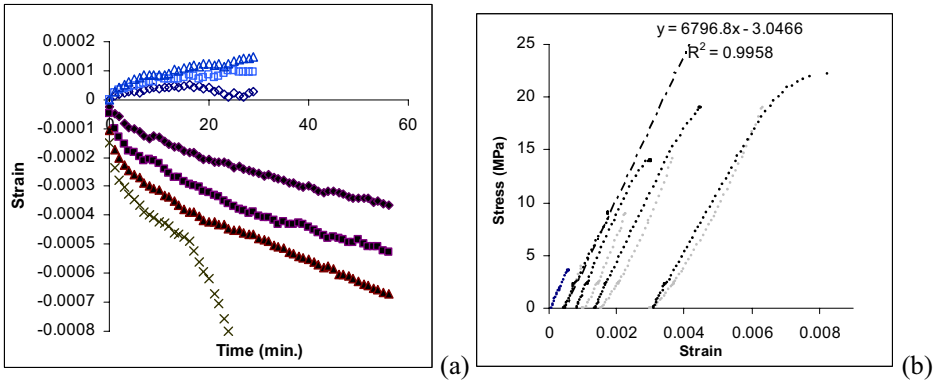

(a) (b)

Figure 4.65. Creep strain and recovery (a) and stress – strain diagram (b) for parallel 1 in semigraphitic material during electrolysis. The creep strain curves in (a) show from top to bottom: Creep recovery after 15, 10 and 5MPa and creep strain after 5, 10, 15, 20 and 25 MPa pressure. The load cell as described in Chapter 3.7 influenced the loading to 5 MPa.

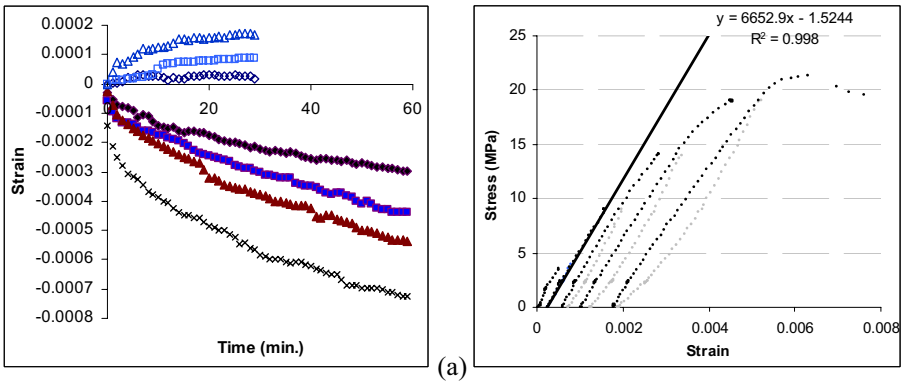

(a) (b)

Figure 4.66. Creep strain and recovery (a) and stress – strain diagram (b) for parallel 2 in semigraphitic material during electrolysis. The creep strain curves in (a) show from top to bottom: Creep recovery after 15, 10 and 5MPa and creep strain after 5, 10, 15 and 20 MPa pressure. The load cell as described in Chapter 3.7 influenced the loading to 5 MPa

The creep strain of the loading to 15 MPa in Figure 4.62 (a) is disturbed due to the problems with the load cell described in the experimental part.

The creep strain in the semigraphitic material, both at 980 °C and during electrolysis, is larger than the respective experiment in the anthracitic material. The creep at 25 °C is smaller than in the anthracitic material if the first parallel is accepted. The crushing strength of the samples exposed to creep at 25 °C had about the same crushing strength (23.4 MPa and 25.5 MPa (Figure 4.81)), but the difference in creep strain between the two parallels at 20 MPa was large. The applied pressure was high relative to the crushing strength and some crushing was probably introduced in the parallel with the large creep strain (Figure 4.60a).

As for the anthracitic material (Figure 4.52 (a)), the creep curves for the semigraphitic material are also independent of the loading history. This failed to be shown at 25 °C but is measured at 980 °C. In Figure 4.67 the creep curves from the reported experiments at 980 °C (Figure 4.62 (a) and Figure 4.63 (a)) are re-plotted with a long-term experiment where 20 MPa was the first applied pressure. It is seen that the curves coincide for both 20 and 25 MPa. For the 25 MPa curve the strain was only logged once a minute while in the other experiments the strain was logged once a second. Some creep strain will be lost if the strain is logged once a minute (see experimental) and the curve is therefore lowered to fit the parallel measurement in the strain direction (vertical direction). The experiment presented in Figure 4.67 extended to 700 minutes and the whole experiment is shown in Figure 4.68.

In Figure 4.69 the creep curves of the short time experiments at 15 MPa during electrolysis (Figure 4.65 (a) and Figure 4.66 (a)) are plotted with a long-term experiment with 15 MPa as the first pressure. It is seen that the curves coincide during the first 60 minutes, which means that the creep is independent of the loading history during electrolysis. In Figure 4.70 the same experiments are re-plotted with an experiment with a lower current density ($i = 0.06$ A/cm^2) and a longer time scale. Although this is only one measured parallel it is not unlikely that a sample with a smaller and slower sodium expansion (Figure 4.22) has a lower creep strain.

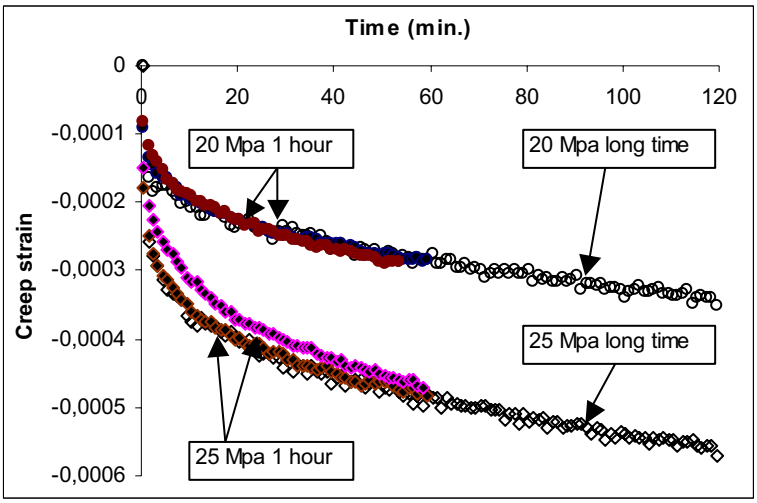

Figure 4.67. Creep strain of two parallel short time experiments (60 minutes) and a long time experiment in semigraphitic material at 980 °C.

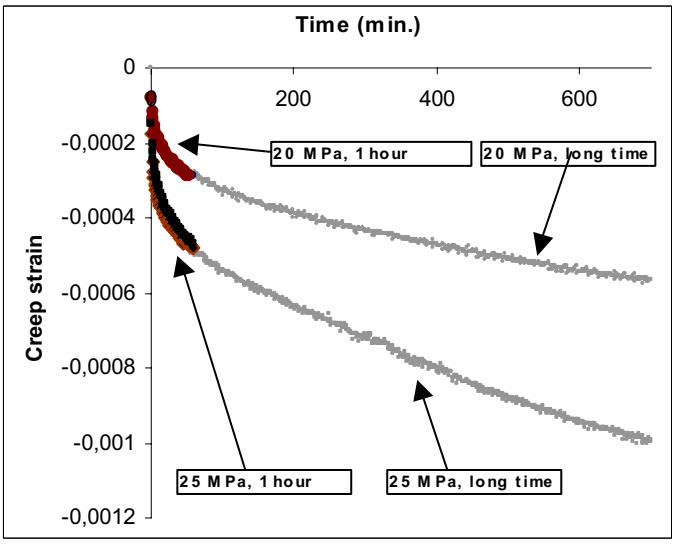

Figure 4.68. Expanded view of Figure 4.67 up to 700 minutes.

As discussed before, the sample shrinks if the electrolysis current is disconnected. This is seen in the long time electrolysis experiments (0.2 A/cm^2) in Figure 4.70 where a break on the curve is seen after 1200 minutes of electrolysis.

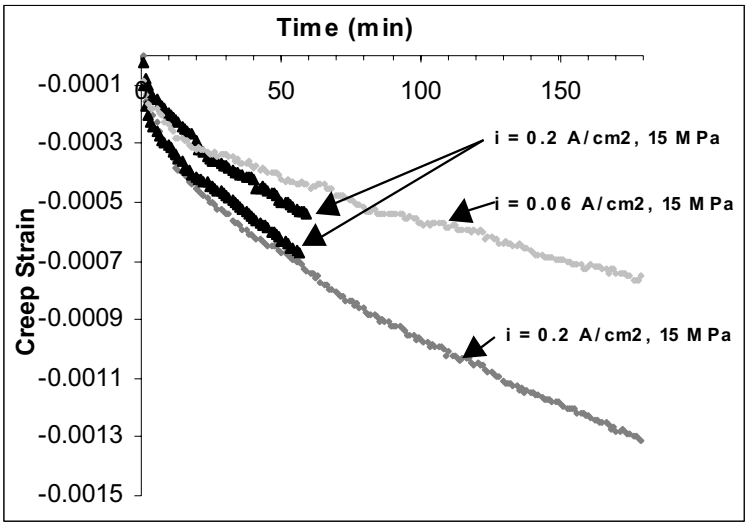

Figure 4.69. Comparison of short-time (60 minutes from Figure 4.65 (a) and Figure 4.66(a)) and long-term experiments during electrolysis in semigraphitic material during electrolysis.

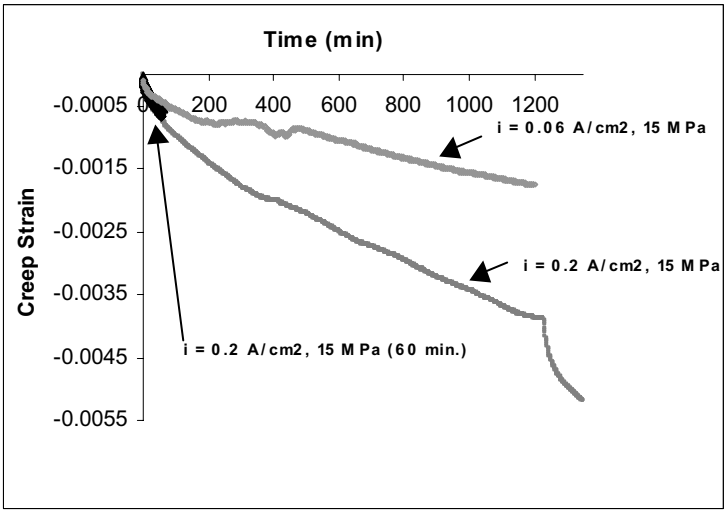

Figure 4.70. Expanded view of Figure 4.69. In the long time experiment with i = 0.2 A/cm^2 the current was disconnected after 1200 minutes and the sample shrunk as sodium probably diffused out of the material.

4.4.3 Creep and E - modulus, semigraphitized material

The experiments at 25 °C for the semigraphitized material are shown in Figure 4.71 and Figure 4.72. The creep strain at 20 MPa from the loading sequence (Figure 4.71 (a)) is re-plotted in the Figure 4.72 (a) for longer times. It is again seen that the creep strain seems independent of loading history. A change in the stress strain diagram after the loading sequence is seen in Figure 4.72 (b). When the load is applied to 20 MPa for the first time, the curve has a smooth convex shape. When the loading sequence 5, 10 and 15 MPa is applied before 20 MPa, the curve is approximately linear up to the stress for the previous loading (15 MPa). Above this stress (15 MPa) the curve coincide with the 20 MPa curve.

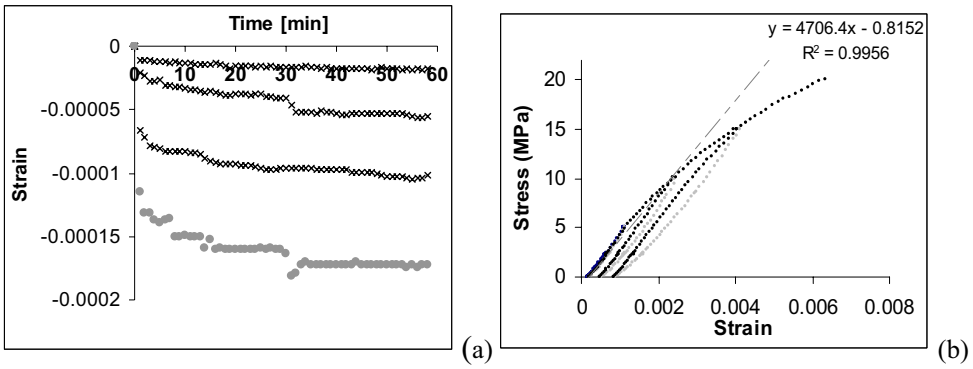

Figure 4.71. Creep strain (a) and stress – strain diagram (b) for the semigraphitized material at 25 °C. The creep strain curves from top to bottom: 5, 10, 15 and 20 MPa.

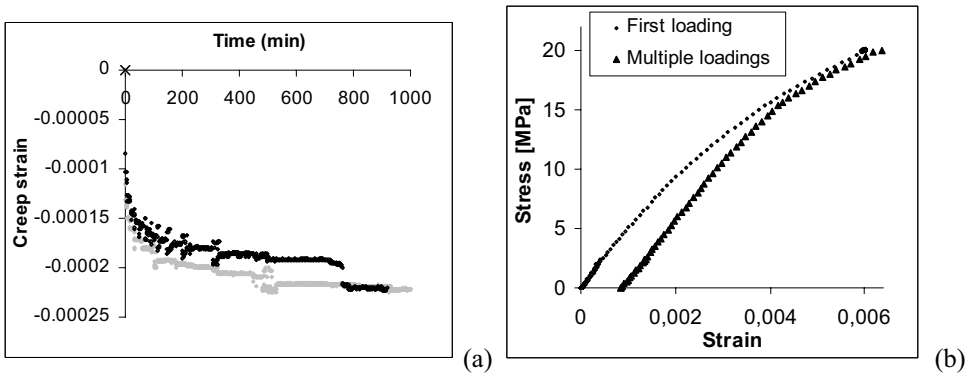

Figure 4.72. Long time creep strain at 20 MPa (a) and stress – strain diagram in semigraphitized material at 25 °C. The darker dots in (a) shows the extended time of the load to 20 MPa from Figure 4.71 (a). The darker dots in (b) are replotted from the 20 MPa loading in Figure 4.71.

The total strain, creep strain and stress – strain diagrams in semigraphitized material at 980 °C are shown in Figure 4.73, Figure 4.74 and Figure 4.75 respectively. The similar results at 980 °C during electrolysis are shown in Figure 4.76, Figure 4.77 and Figure 4.78.

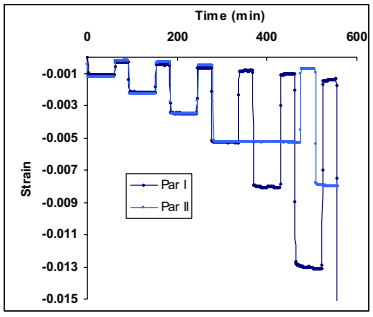

Figure 4.73 Total strain of virgin semigraphitized material.

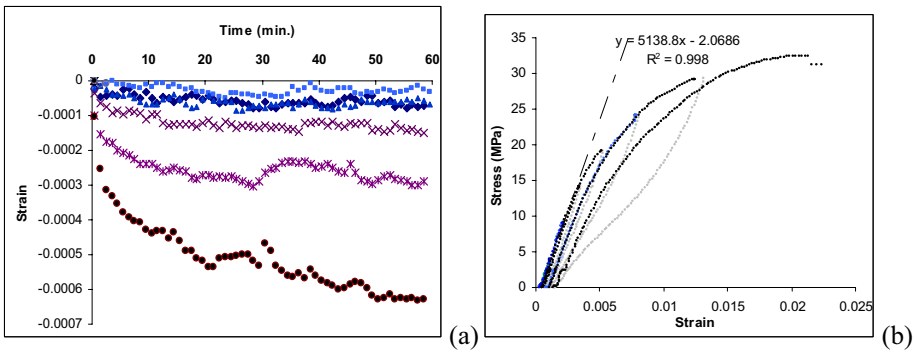

Figure 4.74. Creep strain and recovery (a) and stress – strain diagram (b) for parallel 1 in semigraphitized material at 980 °C. The creep strain curves (a) are from top to bottom: 5, 10, 15, 20, 25 and 30 MPa. The load cell as described in Chapter 3.7 influenced the loading to 5 MPa.

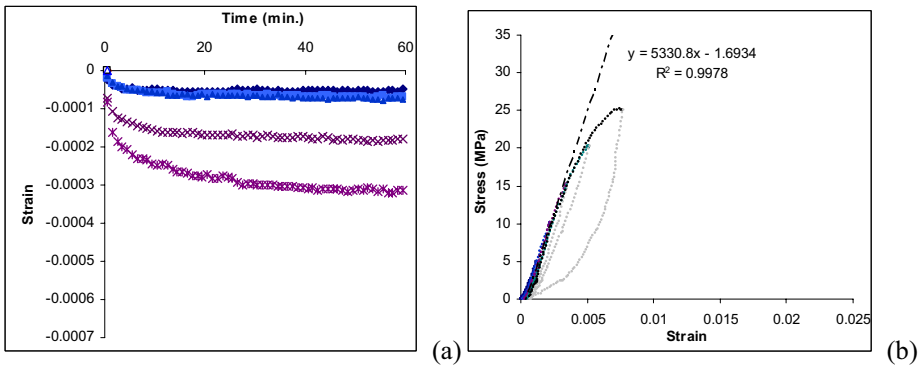

Figure 4.75. Creep strain and recovery (a) and stress – strain diagram (b) for parallel 2 in semigraphitized material at 980 °C. The creep strain curves (a) are from top to bottom: 5, 10, 15, 20 and 25 MPa.

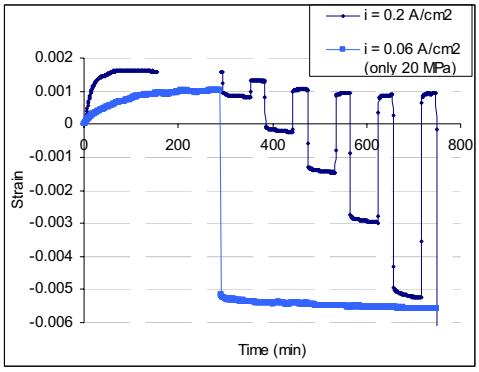

Figure 4.76. Total strain for electrolysed semigraphitized material at 980 °C during electrolysis.

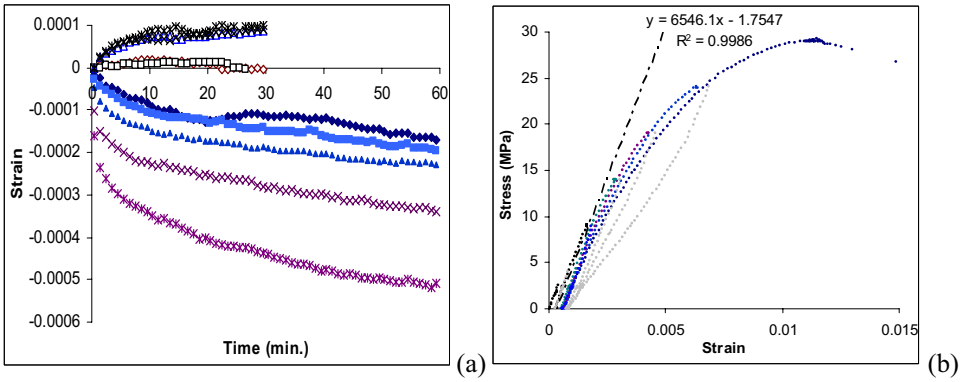

Figure 4.77. Creep strain and recovery (a) and stress – strain diagram (b) for parallel 1 in semigraphitized material during electrolysis. The creep strain curves in (a) show from top to bottom: Creep recovery after 25, 20, 15, 10 and 5MPa, and creep strain after 5, 10, 15, 20 and 25 MPa pressure. The load cell as described in Chapter 3.7 influenced the loading to 5 MPa.

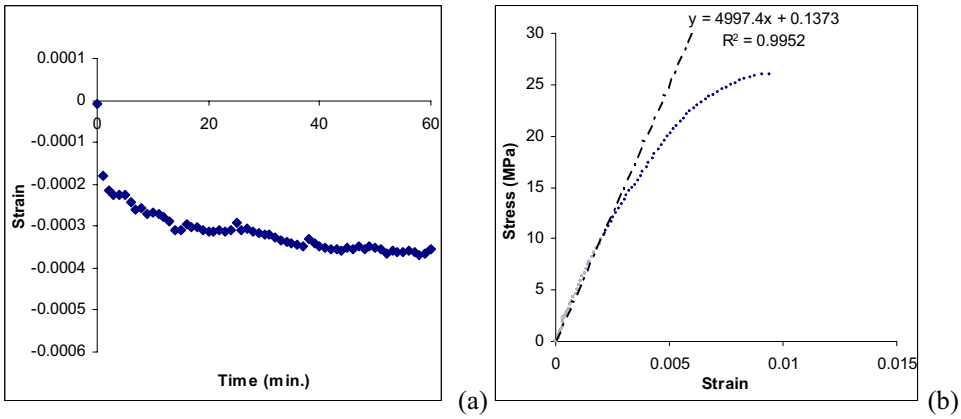

Figure 4.78. Creep strain at 20 MPa at a current density of 0.06 A/cm^2 (a) and stress strain diagram (b) for crushing of the sample after 48 hours of electrolysis at 20 MPa pressure.

The first parallel at 980 °C (Figure 4.74 (a)) was exposed to the highest pressure of all experiments (30 MPa). The creep strain at this stress is large probably because the stress is close to crushing strength (32.5 MPa (Figure 4.74(b))). It is seen that at the previous loading to 25 MPa the creep strain was of the same magnitude as for the second parallel (Figure 4.75 (a)).

The apparatus failed for the second parallel for the semigraphitized material during electrolysis with a current density of 0.2 A/cm^2. An electrolysis experiment with a current density of 0.06 A/cm^2 with only one loading to 20 MPa (Figure 4.78) is instead used for comparison. The creep strain at 20 MPa with the current density of 0.06 A/cm^2 is of the same magnitude as the experiment with 0.2 A/cm^2.

The different experimental conditions affect the semigraphitized material less than observed in the other materials. The creep is relative large at 25 °C but this creep does not change at 980 °C (comparison shown in Figure 4.79). During electrolysis the creep is a little higher than at 980 °C.

Some long time experiments for the semigraphitzed material 980 °C with and without electrolysis at 20 MPa are shown in Figure 4.79. The same experiments are replotted in Figure 4.80 with a extended time scale. The creep strain is not very different after 60 minutes between the parallels, but at longer times the creep rate of virgin material decrease faster.

The measurement pins were observed to stick to the loading piston after the longest experiment with a current density of 0.06 A/cm^2 (Figure 4.80). At what time the measuring rods did not move independent is unknown, but it seems like it could have been around 1200 minutes as the curve before looks smooth.

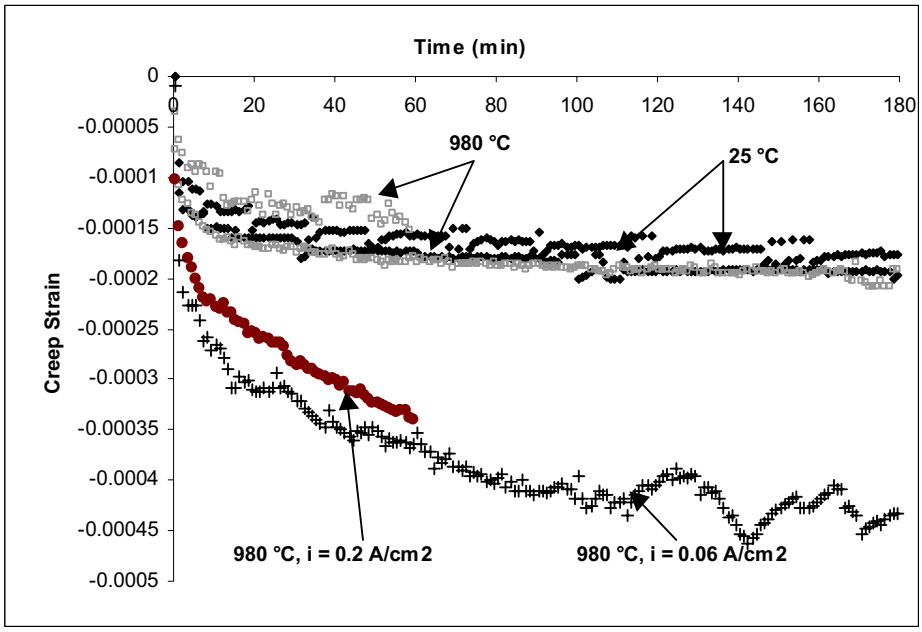

Figure 4.79. Longer time experiments on semigraphitized material with different experimental condition with a pressure of 20 MPa. The experiment with i = 0.06 A/cm^2 is subjected to the first loading.

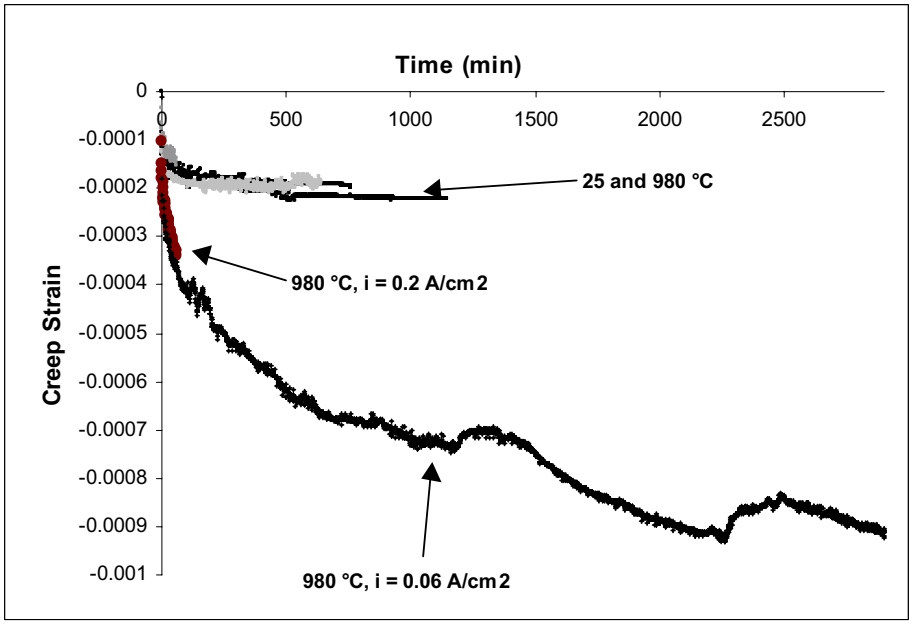

Figure 4.80. Expanded view of Figure 4.79.

4.4.4 Crushing strength and corrected E – modulus

In the end of the loading sequences, the load was sometimes held for a longer time, or the stress was increased to collapse and the compressive strength was determined (Figure 4.81). The number of parallels is few, but the crushing strength seems to increase in all materials from 25 °C to 980 °C [3, 53] and decrease after electrolysis [30, 58, 59] as reported before. Støre et al. [46] measured the compressive strength in the same materials as here (same cathode blocks) in 10 samples with a diameter of 50 mm and a height of 50 mm. The average crushing strength for the semigraphitic and semigraphitized materials was 23.3 MPa and 27.0 MPa respectively and is in good agreement with the crushing strength measured here (on Ø30, length 60 mm samples). The crushing strength for the anthracitic samples was lower than the measurements of Støre (27 MPa versus 31.3 MPa). The length – diameter ratio could influence the anthracitic material more than the other materials, but the two lowest strength measurements of Støre were 28 MPa, only 1 MPa above the ones measured here.

The dynamic E – modulus was also measured by Støre et al. [46] at 25 °C and was in general approximately 20 % higher than the corrected static E-modulus measured here. The E – modulus shown in Figure 4.82 are corrected for the elasticity of the apparatus (Eq. (3.1) at 25 °C and Eq. (3.2) at 980 °C)).

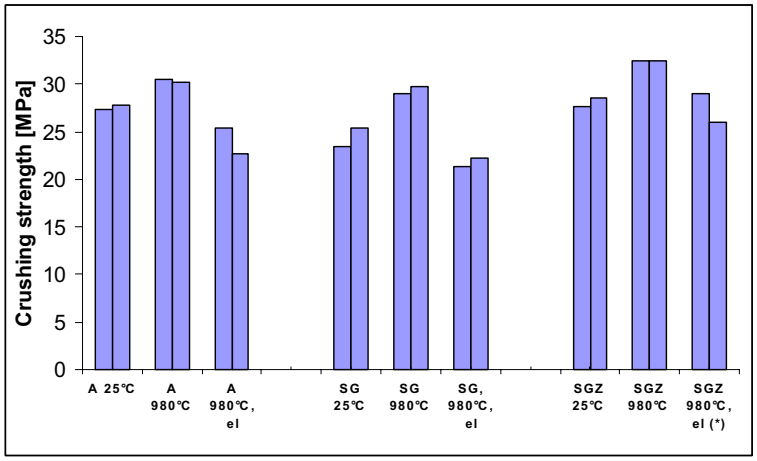

Figure 4.81. Crushing strength in the end of the experiments. Abbreviations: A – anthracitic, SG – semigraphitic, SGZ – semigraphitized, el – electrolysis. (*) - The second parallel on the semigraphitized material during electrolysis was with a current density of 0.06 A/cm^2 (the other with 0.2 A/cm^2) and an electrolysis time of 3000 minutes.

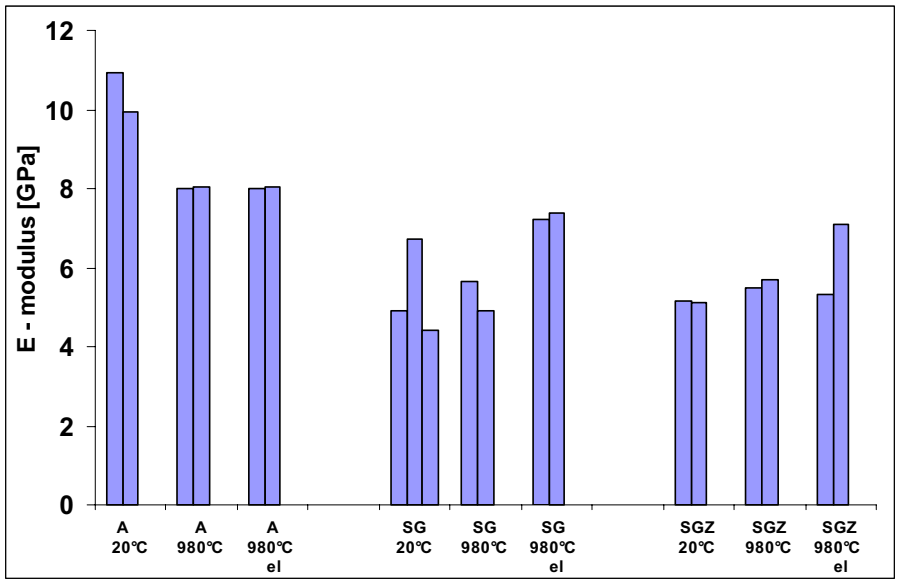

Figure 4.82. Corrected E – modulus for all the experiments (Eq. 3.1 and Eq. 3.2) Abbreviations: A – anthracitic, SG – semigraphitic, SGZ – semigraphitized, el – electrolysis.

4.4.5 Creep - permanent deformation

After the load is removed, the sample is free to expand and a creep recovery is achieved. The creep recovery curves are only reported for the electrolysis experiments, as the creep of the apparatus influenced the small strains in the other experimental conditions too much. The permanent deformation (reduction of length in %) in the end of the creep recovery period is given in Figure 4.83, Figure 4.84 and Figure 4.85 for anthracitic, semigraphitic and semigraphitized material, respectively. The results are here not affected by the problems with the load cell and the trends are easier to see.

The permanent deformations give the same ranking as the creep strain measurements where the semigraphitized material has the smallest deformation in all cases except at 25 °C. The semigraphitic material deforms most, except at 25 °C (based on one experiment only), and a larger deformation at 980 °C and at 980 °C during electrolysis is seen.

At 25 °C a pressure of 20 MPa was held around 18 hours compared to 1 hour in the other experiments. In the experiments with the semigraphitized and anthracitic material at 980 °C the load at 20 MPa was held for 3 hours instead of 1 hour. The increase in time does not seem to affect the reduction of the sample length after creep recovery as the parallel experiment with the

same pressure applied for only 1 hour shows approximately the same length reduction (Figure 4.83 and Figure 4.84). It seems like much of the deformation is related to the first hour in the experiments without electrolysis.

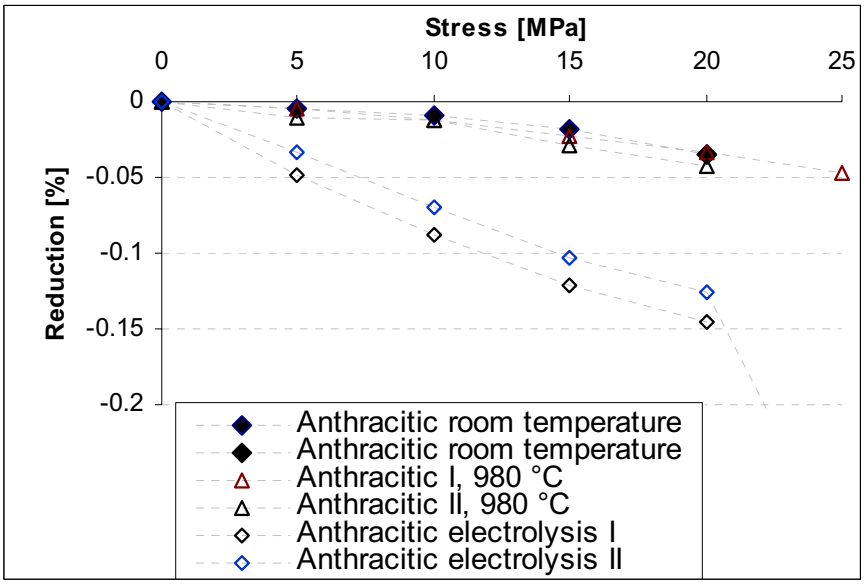

Figure 4.83. Length reduction in the anthracitic material (%) after the 0.5 hour recovery period. At 980 °C one parallel was held at 20 MPa for 3 hours. The room temperature recovery at 20 MPa was measured after holding the pressure for 18 hours and 6 hours recovery.

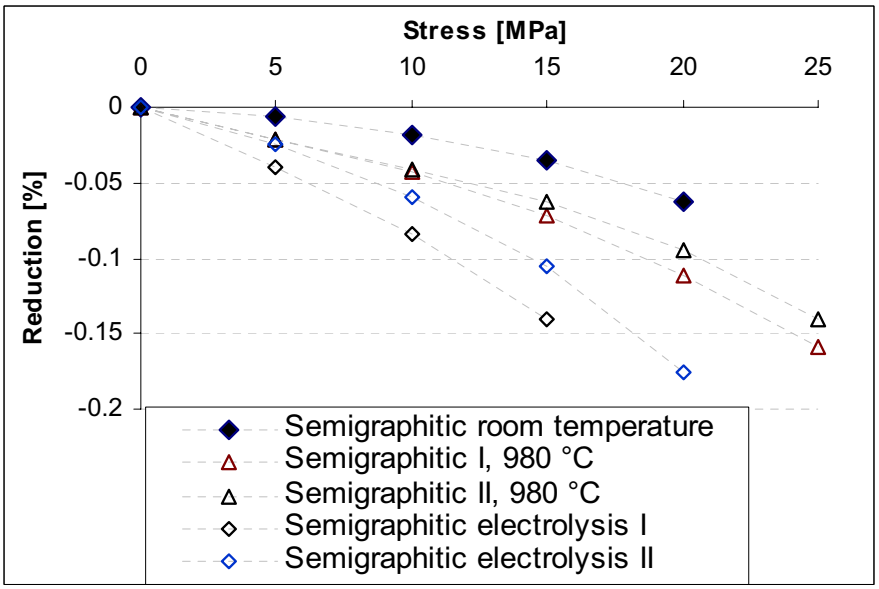

Figure 4.84. Length reduction in the semigraphitic material (%) after the 0.5 hour recovery period. At 980 °C one parallel was held at 20 MPa for 3 hours. The room temperature recovery at 20 MPa was measured after holding the pressure for 18 hours and 6 hours recovery.

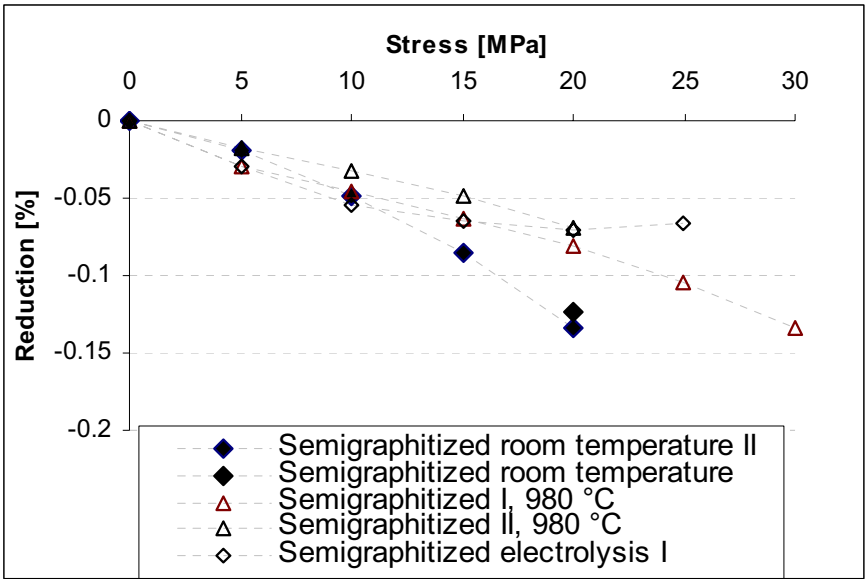

Figure 4.85. Length reduction in the semigraphitized materials (%) after the 0.5 hour recovery period. The room temperature recovery at 20 MPa was measured after holding the pressure for 18 hours and 6 hours recovery.

4.4.6 Creep - modelling

The creep behaviour for a number of materials could be described by Eq. (2.32). The logarithm of the creep strain in is given by Eq. (4.7). A plot of log $|\varepsilon^{(c)}|$ versus log(t) should yield a straight line with a slope n independent of the stress.

$$\log\left|\varepsilon^{(c)}\right| = \log K + n\log t \qquad (4.7)$$

The creep measurements for the semigraphitic virgin material at 980 °C (Figure 4.68) are re-plotted with logarithmic axes in Figure 4.86. The logarithm of the absolute value of the creep strain is plotted, so the upper curves show measurements for 25 MPa pressure and the lower curves show results for 20 MPa. The fitted straight lines for the experiments lasting for 60 minutes are extrapolated up to 700 minutes. It is seen that the extrapolated curves interpret both smaller and larger creep than the measured strain to 700 minutes. The first minute is deleted in the fitting as short times have large influence on the curve fit. The exact point when the strain turns from elastic to creep strain is as before discussed a difficult task.

The model fits poorer for the 25 MPa pressure experiment (Figure 4.86). At this stress the crushing strength of the material is approached and the creep strain often shows a different behaviour [62, 68].

The repeated measurements on the semigraphitic material during electrolysis at 15 MPa are plotted with logarithmic axes in Figure 4.70. The data are collected from Figure 4.65 (a) and Figure 4.66 (a) for the short time experiments and from Figure 4.69 for the long time experiment. It is seen that the short time experiments predict the longer time experiment also during electrolysis.

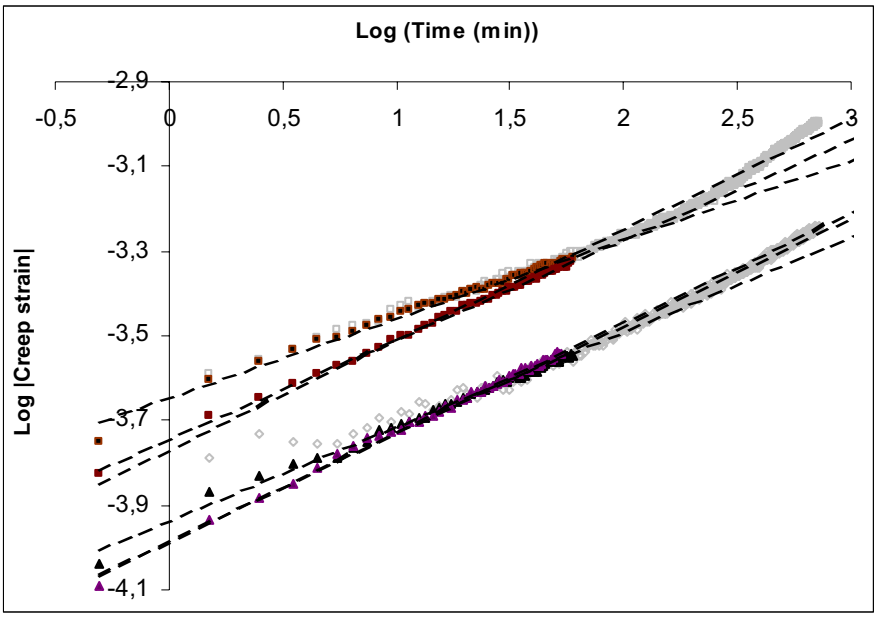

Figure 4.86. Log (time) – Log (|creep strain|) diagram for virgin semigraphitic material at 20 MPa (lower curves) and 25 MPa (upper curves). The darker symbols represent two parallels at each pressure in the short time experiments.

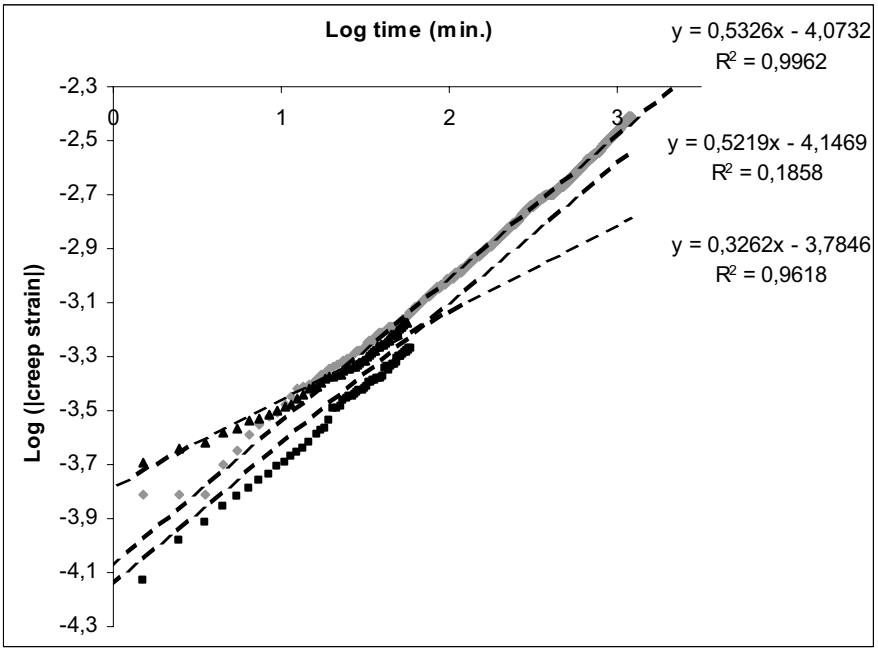

Figure 4.87. Longer time experiments on electrolysed semigraphitic material at 15 MPa pressure.

An example of a log(time)–log(creep strain) plot of the measurements achieved in the load sequence experiments is shown in Figure 4.88 (anthracitic, i = 0.2 A/cm^2, Figure 4.57 (a)). It is seen that the strains at 5 MPa have a poorer fit. This is probably due to the problems with the load cell as described in the experimental part. The curves for the different pressures should be parallel if Eq. (4.1) describes the creep behaviour, and the calculated n should be independent of pressure. The constant K includes an expression for the pressure.

All the measurements at each stress were fitted to straight lines as shown in Figure 4.88 and the calculated constants are presented in Figure 4.89 (anthracitic), Figure 4.90 (semigraphitic) and Figure 4.91 (semigraphitized).

The log K – member of Eq. (4.7) is sometimes a function of stress raised in some exponent ($log(K) = \sigma^k$) but for all the presented data, the stress dependence fit better with a linear fit ($log(K) = k\sigma$), except for the semigraphitic electrolysed material. In this material the fit was $R^2 = 0.9443$ for a raised case ($log(K) = \sigma^k$) and 0.9178 in the linear case. The calculated K – value seems independent of pressure for the electrolysis experiments and for the anthracitic material in general, but in the other experiments the constant tends to increase with pressure. The average of the calculated constants is presented in Table 4.3.

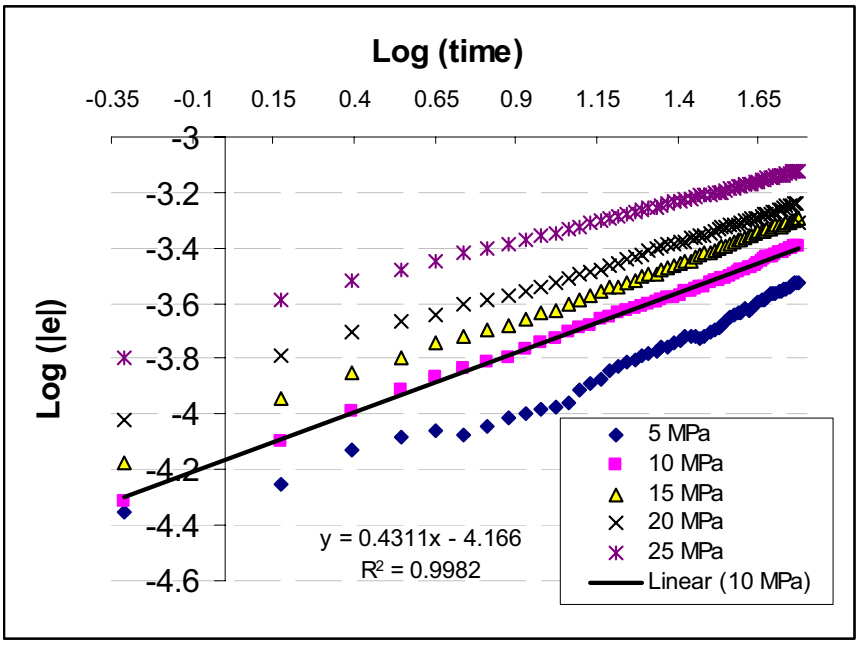

Figure 4.88. Example of log (time/min) – log(strain) diagram. The presented material is anthracitic with electrolysis.

The 5 MPa measurement for the virgin anthracitic material (Figure 4.89) had some positive values (unstable load) and the 10 MPa had relatively rapid creep for the first minute. The same two measurements have the two highest values for K in Figure 4.89 (b). If these measurements are disregarded it is seen that the fitted slope n is larger for the electrolysed material than for the virgin material. This means that these curves decrease faster with time.

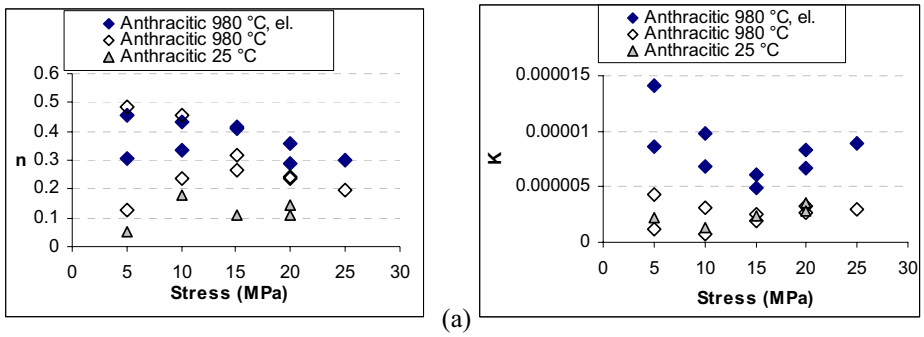

(a) (b)

Figure 4.89. Calculated constants in Eq. (4.1) for anthracitic material (n in Figure (a) and log K in Figure (b)).

In Figure 4.90 the constants for the semigraphitic material are shown. The high n and low log(K) for 5 and 10 MPa pressure for one virgin parallel is observed. When these creep-strain data are studied (Figure 4.62) it is seen that the material expands at some points, instead of shrink, giving reason to believe that the load cell probably is the problem. Disregarding these points it is seen that n again is higher for the semigraphitic material and the electrolysed material has a higher log K value.

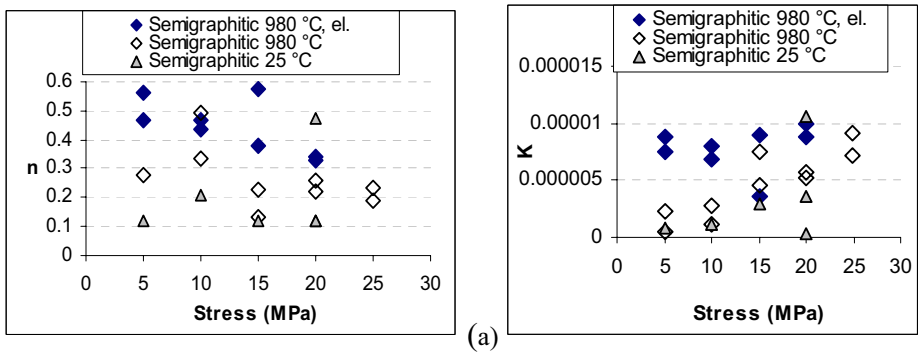

(a) (b)

Figure 4.90. Calculated constants for the semigraphitic material.

The semigraphitized material (Figure 4.91) exhibits a smaller difference in creep strain for the various experimental conditions. However, with some scatter n seems higher for the electrolysed material while log K seems more independent of experimental condition.

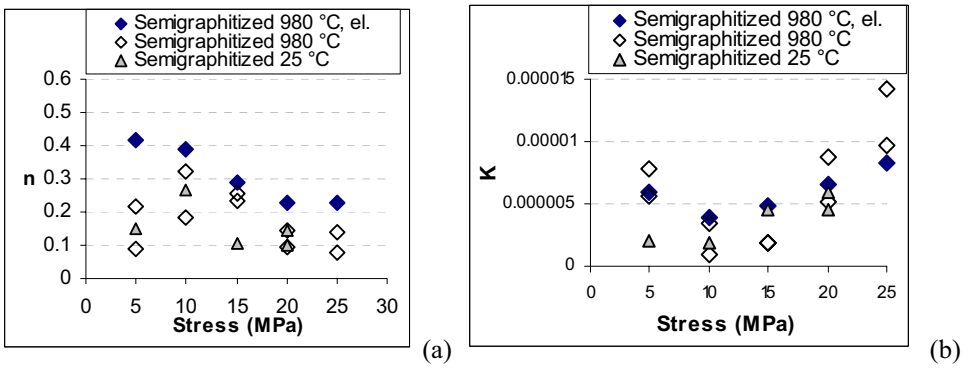

(a) (b)

Figure 4.91. Calculated constants for the semigraphitzed material.

In Figure 4.92 Eq (2.32) is plotted with the fitted constants for the two parallel measurements of the semigraphitic material during electrolysis. It is seen that the fitting overshoots at low pressure. The stress dependence of the constant K could been expressed in other ways, but this is not done here. The expression, t^n, seems to give a good fit.

The slopes (n) vary within parallels and also within one experiment. The variations are larger at lower stresses. At lower stresses, smaller distances are measured and the noise/signal ratio is larger. The semigraphitized material is before shown to have the same creep strain at 20 MPa at 25 °C and at 980 °C but this is not clear in the calculated constants. When smaller, less accurate strains (at lower pressures) are included in the calculation the fitting is poorer. But it is seen that, in general, the virgin materials have a smaller time dependency than the electrolysed. It is also seen that the semigraphitized material has less time dependency than the other materials, both in virgin and in electrolysed condition. Most of the n - values are between 0.2 and 0.5. Zukas and Green [63] reported that a number of graphites have this constant around 0.5.

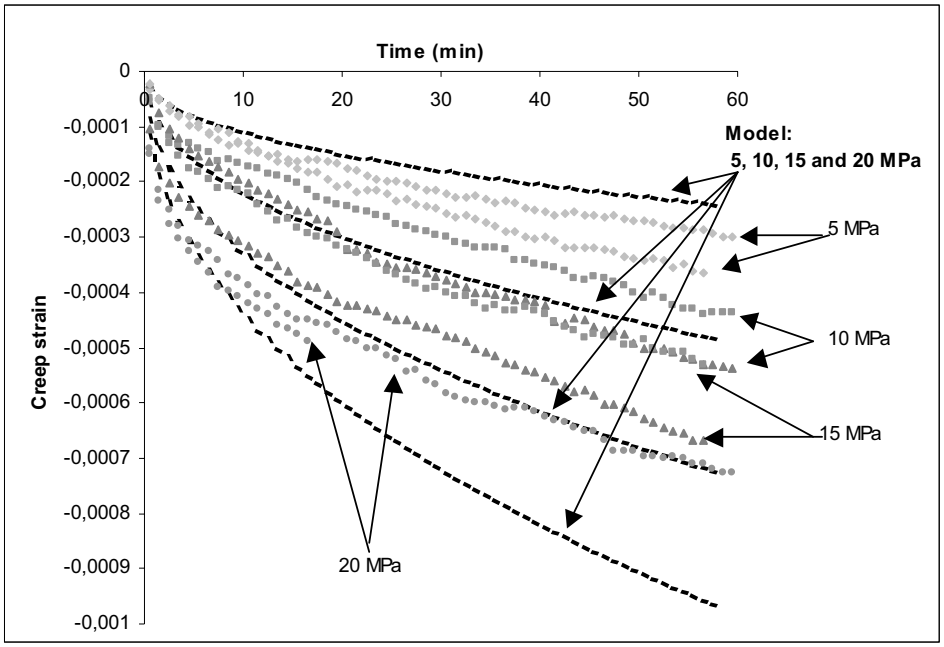

Figure 4.92. Eq. (4.7) with the calculated constants (dotted smooth lines) plotted with the two parallel measurements of the semigraphitic material during electrolysis. ($K = 7.79 \cdot 10^{-6}$, $n = 0.45$).

Table 4.3. Average of calculated constants to Eq. (4.7).

	K	n
Anthracitic 980 °C, electrolysis	8.26E-06	0.37
Anthracitic 980 °C	2.54E-06	0.29
Anthracitic 25 °C	2.46E-06	0.12
Semigraphitic 980 °C, electrolysis	7.79E-06	0.45
Semigraphitic 980 °C	4.60E-06	0.32
Semigraphitic 25 °C	3.23E-06	0.19
Semigraphitized 980 °C, electrolysis	5.90E-06	0.31
Semigraphitized 980 °C	4.19E-06	0.20
Semigraphitized 25 °C	3.76E-06	0.15

4.4.7 Creep – summary

A graph to summarise the creep strain of the materials is given in Figure 4.93 where all parallels at 20 MPa are shown during electrolysis. Only one pressure is shown to make the graph simple. The ranking with increasing creep was:

Semigraphitized < Anthracitic < Semigraphitic

This was the typical trend between the materials at 980 °C and 980 °C during electrolysis. At 25 °C the semigraphitized crept the most if the last parallel of the semigraphitic material with the high creep is disregarded (Figure 4.60a).

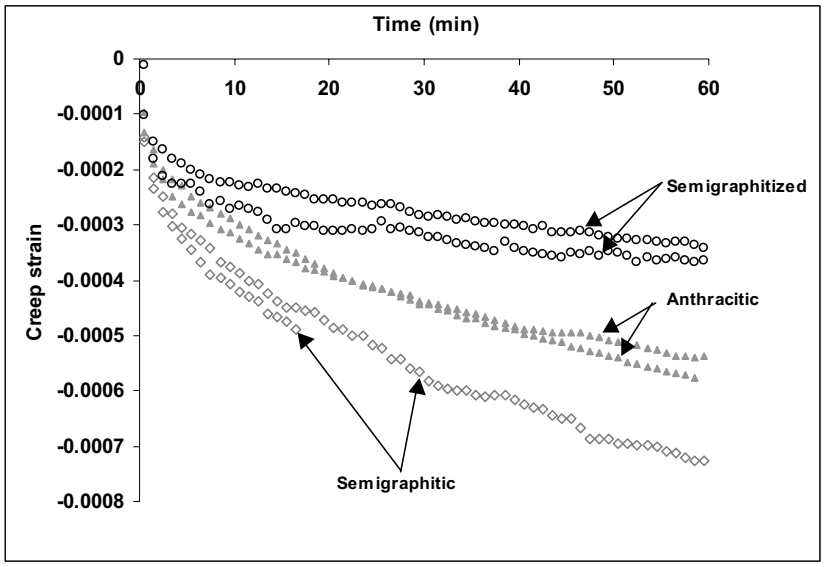

Figure 4.93. Comparison of two parallels for each material during electrolysis with a pressure of 20 MPa. If the creep strain axis is divided by a value between 2 and 3, the same ranking is achieved at 980 °C without electrolysis (meaning that the creep strain is higher during electrolysis).

The typical trend within one material at the different experimental conditions is shown in Figure 4.94 (anthracitic material). The creep increased when the temperature was increased from 25 °C to 980 °C, except for the semigraphitized material where no difference between the temperatures was measured (Figure 4.79). The largest creep was in all materials measured during electrolysis. The upper curve in Figure 4.94 shows the creep of the apparatus (see Chapter 3.7.1) that not is subtracted from the measurements, as the parallels often are more scattered than this

almost negligible value. The electrolysis had largest effect on the anthracitic material, as this material had the highest increase in creep from virgin to the electrolysed state.

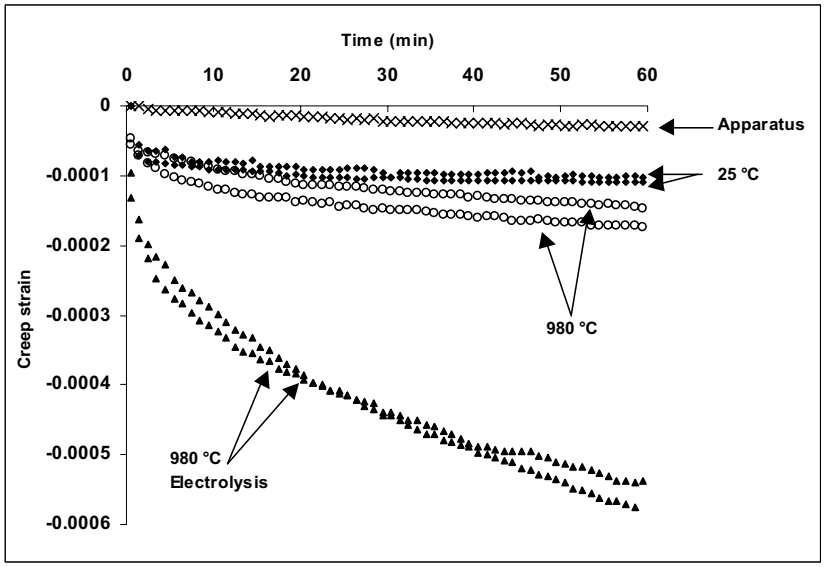

Figure 4.94. Creep strain of two paralells for the anthracitic material at all experimental conditions with a pressure of 15 MPa. The difference is typical for the other materials as well. The smaller creep of the apparatus is shown in the upper curve.

At room temperature the crushing strength of the material is lower (Figure 4.81) and relative to the crushing strength the load is larger at 25 °C than at 980 °C. The stress is sometimes expressed relative to crushing strength [54], but this is not done here.

The stress – strain diagrams show some distinct futures. There is a difference between the experiments where the 20 MPa pressure was applied after the loading sequence (5, 10, 15 MPa) compared with when this pressure was applied for the first time. This difference is not observed in the anthracitic material (Figure 4.52 (b)) which in general shows a more linear behaviour. But as seen from the semigraphitic (Figure 4.62 (b)) and semigraphitized (Figure 4.72 (b)) the stress – strain diagrams depend of the loading history. When the pressure is 5 MPa higher than the subsequent pressure, the curves are linear up to the stress for the previous loading, to further coincide with the non-linear behaviour achieved when the load is applied for the first time. This effect was also observed by Allard et al. [53] who measured the fracture energy. They explained the effect as an hardening effect.

The creep curves do not reach a constant creep rate (secondary creep) as observed in graphite at higher temperatures. The behaviour looks more like what is observed for concrete (Chapter 2.4).

In general, the shape of the creep curves sometimes change after repeated loading [62]. The creep curves is not found to change shape after repeated loadings.

The creep curves fit the time term in t^n well in the proposed equation, but the scatter was too large to determine the pressure dependence.

Creep mechanism

Allard et al. [53] measured E – modulus, crushing strength and fracture toughness for materials ranging from anthracitic to fully graphitized. An increase in all mechanical properties was found with increasing temperature. The crack growth resistance was not related to the graphite content in these experiments. The increased values for the mechanical properties were explained by closing of cracks and voids formed during cooling of the manufactured material. This has also been explained to be the reason for strength increase of graphite [28].

If the creep mechanism is related to the same cracks and voids causing a strength increase, one should expect fewer cracks at high temperature and less creep. But, except for the semigraphitized material, the creep is larger at high temperature. The cracks/voids that close at 980 °C causing strength increase could be of another size and/or geometry than the ones causing creep. Allard et al. [53] could not distinguish between the fracture energy from microcracks and from the machined main crack. The crack evolution for the strength increase and creep properties might be two different mechanisms and growth of microcracks can still hold as an explanation.

The anthracitic material, which could be expected to have the largest creep during electrolysis, was the ranked as the medium among the three studied materials. This material should have the highest stress history as this material has the highest sodium expansion and the highest E – modulus. This was the only material were new cracks were observed during electrolysis (Figure 4.13) and it also had the highest creep increase from virgin material at 980 °C to 980 °C during electrolysis. Some of the increase in creep might be attributed to these cracks. The microscope magnification in the structure studies might be too low to reveal the microcracks which determine the creep properties.

The expansion of the materials could be an important parameter affecting the creep. The macro - structure of the materials is set at around 500 °C when the binder carbonises. Above this temperature the structure is changed on the micro – level by decreasing distance between the graphene layers and building of larger stacks of layers (graphitisation). The semigraphitic material, which has the highest creep at 980 °C, might have the largest difference between its constituents. The material contain an aggregate which have been treated at temperatures above 2500 °C and the binder only to ~1200 °C. The difference in thermal - and sodium- expansion between its constituents is probably large. And as the temperature differs from the temperature when the structure is set (~500 °C), stresses will occur in the zone between the two different materials and cracks might form. If this is the case, there should be a minimum in creep at a temperature between 25 °C and 980 °C where the structure is more relaxed.

In the semigraphitized material, the binder and aggregate have both been at temperatures of 2200~2800 °C and in the microscope the material appears more homogenous (Figure 4.14). When this material expands or shrinks, less internal stresses probably occur between its constituents as no difference in creep is observed between 25 °C and 980 °C. After an electrolysis period some micro cracks could form giving a larger creep.

4.5 Technological implications

Small creep strains are not necessarily the best choice when it comes to choice of creep properties for cathode block materials. A material with small creep strain properties will deform slower if a stress of some magnitude is introduced. When strain is introduced (sodium expansion, thermal expansion) a longer time is needed for stress relaxation for a material with small creep strain properties. This means that the stresses will reduce fastest in the semigraphitic material if the same strain is introduced to the three materials, both in virgin and electrolysed condition.

During preheating the E - modulus and the thermal expansion will determine the stress in the cathode. The thermal conductivity and diffusivity of the more graphitic materials is in general higher and a low temperature gradient will introduce smaller stresses. The anthracitic material with a low thermal conductivity and low creep in virgin state will, in combination with its high E – modulus, get the highest stresses in a preheating period if the thermal expansion in the materials is the same. The semigraphitic material could have the lowest stresses because of a large creep, but would deform the most.

The semigraphitized material could introduce the smallest stresses of during sodium expansion because of the small sodium expansion combined with a relative low E - modulus. But if the induced stresses for some reason should be high, the material will have the worst creep properties to relax stresses.

Comparing the anthracitic and semigraphitic materials during electrolysis, the anthracitic material has higher sodium expansion and E – modulus, resulting in higher stresses. As the diffusion coefficient is lower, the sodium induced stresses will remain for a longer time and will be relaxed slower because of the lower creep properties.

To reduce the sodium induced stresses during start-up a lower and slower expansion could be obtained by using a low current density (in the range 0.05 A/cm^2). The maximum stresses will probably be smaller and because of a longer time for stress relaxation (creep), the largest stresses would be reduced.

The time for sodium saturation in the cathodes is independent of the measured cryolite ratios (CR=4 and CR=2.2) for the semigraphitic material. This gives another argument for acidic startup, at least for the semigraphitic material.

In the presented experiments, only compressive stresses are measured to make the experiments easier to handle. A more critical stress, tension stresses, may arise during sodium penetration in the cathode because of the cathode bending [3]. Knowing that carbon materials are much weaker in tension than compression, the tension properties should be determined.

References

[1] Grjotheim, K. and Kvande, H., ”Introduction to Aluminium Electrolysis”, 2nd ed., Aluminium – Verlag, Düsseldorf, 1993.

[2] Marsh, H. (ed.), ”Introduction to Carbon Science”, Butterworths, London, 1989.

[3] Sørlie, M. and Øye, H.A., ”Cathodes in Aluminium Electrolysis”, 2nd ed., Aluminium – Verlag, Düsseldorf, 1994.

[4] Thonstad, J., Fellner, P., Haarberg, G.M., Hives, J., Kvande, H. and Sterten, Å., “Aluminium Electrolysis, Fundamentals of the Hall-Heroult Process”, 3rd ed., Aluminium-Verlag, Düsseldorf, Germany, 2001.

[5] Thonstad, J. and Rolseth, S., “On the Cathodic Overvoltage on Aluminium in NaF - AlF_3 - Al_2O_3 Melts – II.”, Electrochim. Acta 23 (1978), 233-241.

[6] Rolseth, S., Personal communication, unpublished results.

[7] Xu, Q., Schwandt, C., Chen, G.Z. and Fray, D., “Electrochemical Investigation of Lithium Intercalation into Graphite from Molten Lithium Chloride.”, Journal of Electroanalytic Chemistry 530, 2002, 16-22.

[8] Chen, G.Z., Fan, X., Luget, A., Shaffer, M.S.P., Fray, D. J. and Windle, A.H., “Electrolytic Conversion of Graphite to Carbon Nanotubes in Fused Salts.”, J. Electroanalytical Chemistry 446, 1998, 1-6.

[9] Doeff, M. M., Ma, Y., Visco, S.J. and De Jonghe, L.C, “Electrochemical Insertion of Sodium into Carbon.”, J. Electrochem. Soc., Vol. 140, No. 12, Dec. 1993, L169-L170.

[10] Thomas, P. and Billaud, D., “Electrochemical Insertion of Sodium Into Hard Carbons.”, Electrochim Acta, Vol. 47, 2002, 3303 – 3307.

[11] Thomas, P. and Billaud, D., “Sodium Electrochemical Insertion Mechanisms in Various Carbon Fibres.”, Electrochemica Acta, Vol. 46, 2001, 3359-3366.

[12] Joncourt, L., Mermoux, M, Touzain, Ph, Bonnetain, L., Dumas, D. and Allard, B. “Sodium Reactivity with Carbons.”, J, Phys. Chem Solids, Vol. 57, No. 6-8, 1996, 877-882.

[13] Gudbrandsen, H., Sterten, Å. and Ødegård, R., "Cathodic Dissolution of Carbon in Cryolitic Melts.", Light Metals, 1992, 521-528.

[14] Grjotheim, K., Krohn, C., Malinovsky, M., Matiasovsky, K. and Thonstad, J., “Aluminium Electrolysis, Fundamentals of the Hall-Heroult Process”, 2nd ed., Aluminium-Verlag, Düsseldorf, Germany, 1982.

[15] Metrot, A. and Herold, A., “Insertion et Adsorption du Sodium par les Carbones.”, J. Chim.-Phys., 1969, 71-79.

[16] Asher, R.C., ”A Lamellar Compound of Sodium and Graphite.”, J.Inorg. Nucl. Chem., Vol. 10, 1959, 238-249.

[17] Metrot, A., Guerard, D., Billaud, D. and Herold, A., “New Results about the Sodium-Graphite System.”, Synth. Met., Vol. 1, 1979, 363-369.

[18] Herold, A., Mareche, J.F. and Lelaurain, M., “Intercalation of Sodium with its Halides into Graphite.”, Carbon, Vol. 38, 2000, 1955-1963.

[19] Mikhalev, Y. and Øye, H.A., “Absorption of Metallic Sodium in Carbon Cathode Materials.”, Carbon 34. Vol. 1, 1996, 37 – 41.

[20] Sechet, C., Sarmeo, D., Mermoux, M., Touzain, Ph., Bonnetain, L., Dumas, D., Allard, B. and Paulus, R., “Sodium Reactivity with Anthracitic Carbons at 700 °C.”, Mol. Cryst. Liq. Cryst., Vol. 245, 1994, 153-158.

[21] Robert, M.C., Oberlin, M. and Mering, J., “Lamellar Reaction in Graphitizable Carbons.”, In Chemistry and Physics of Carbon, Vol. 10, Walker, P.L. and Thrower, P.A.(eds.), Marcel Dekker Inc., New York, 1973, 141-211.

[22] Dell, M.B., “Reaction between Carbon Lining and Hall Bath.”, In Extractive Metallurgy of Aluminium. vol. 2 Gerard, G. (ed.), Wiley Interscience publishers, New York, 1963, 403-416.

[23] Dewing E. W., “The Reaction of Sodium with Nongraphitic Carbon : Reaction Occurring in the Linings of Aluminium Reduction Cells.”, Trans. Met. Soc. AIME Vol. 227, 1963, 1328-1333.

[24] Brilloit, P., Lossius, L. P. and Øye, H. A., “Penetration and Chemical Reactions in Carbon Cathodes during Aluminium Electrolysis: Part I. Laboratory Experiments.”, Metallurgical Transactions B, Vol. 24 B, February 1993, 75-89.

[25] Krohn, C., Sørlie, M. and Øye, H.A., “Penetration of Sodium and Bath Constituents into Cathode Carbon Materials Used in Industrial Cells.”, Light Metals, 1982, 311-324.

[26] Herold, A., “Reflections on Matter Transfer in Graphite Intercalation Chemistry.”, Synth. Met., Vol. 23, No. 1-4, 1988, 27-35.

[27] Kingery, W.D., “Introduction to Ceramics”, fourth printing, April 1967.

[28] Rice, W.R., “Mechanical Properties of Ceramics and Composites”, Marcel Dekker, New York, 2000.

[29] Zolochevsky, A., Hop, J.G., Servant, G., Foosnæs, T. and Øye, H.A., “Rapoport-Samoilenko Test for Cathode Carbon Materials, I. Experimental Results and Constitutive Modelling.”, Carbon, Vol. 41, 2003, 497-505

[30] Naas T., “Interactions of Alkali Metals and Electrolyte with Cathode Carbons”, Thesis, Norwegian Inst. Technol., Trondheim, 1997.

[31] Houston G.J., Welch B.J. and Young D.J. “Uptake of Electrochemically Generated Forms of Sodium by Various Carbons”, Light Metals, 1981, 529-540.

[32] Panebianco B. and Bacchiega R., “Deformation Phenomena caused by Electrolytic Al Baths.”, Allumino, Vol. 35, No. 2, 1966, 67-78.

[33] Waddington J., “The investigation of the movements and temperatures in the cathode of an aluminium reduction furnace.”, Journal of Metals, September 1969, 27-31.

[34] Dewing, E.W., “Longitudinal Stresses in Carbon Lining Blocks.”, Light Metals, Vol. 3, 1974, 879-887.

[35] Øye H.A., Thonstand J., Dahlqvist K., Handå S. and de Nora V., “Reduction of Sodium Induced Stresses in Hall-Heroult Cells.”, Aluminium, December 1996, 918-924.

[36] Jean, M., Desnoyer, C., Tranchant, A. and Messina, R., ”Electrochemical and Structural Studies of Petroleum Coke in Carbonate-Based Electrolytes.”, J. Electrochem. Soc., Vol. 142, No. 7, July 1995, 2122-2125.

[37] Weppner, W. and Huggins, R.A., ”Determination of the Kinetic Parameters of Mixed-conducting Electrodes and Application to the System Li_3Sb.”, J. Electrochem. Soc. 1997, 1569 – 1578.

[38] Funabiki, A., Inaba, M., Abe, T. and Ogumi, Z.,”Influence of Defects on the Phase-Boundary Movement in a Stage Transformation of Lithium-Graphite Intercalation Compounds.”, Cabon, Vol. 37, 1999, 1591-1598.

[39] Sleepy, W.C., “Reaction of Sodium with Graphite at 400 °C.”, Inorg. Chem. Vol. 5, No. 11, 1996, 2021-2023.

[40] Crank, J., “The Mathematics of Diffusion”, 2nd edition, 1973.

[41] Rapoport, M.S. and Samoilenko, V.N., “Deformation of the Carthode Blocks of Aluminium Electrolysis Cells during the Electrolysis Process.”, Tsvetn. Met. Vol. 30, No. 2, 1957, 44-51.

[42] Wilkening, S. and Busse, G., “Evaluation and Production of Carbon Cathode Blocks.”, Light Metals, 1981, 653-674.

[43] Peyneau, J.M., “Laboratory Testing of the Expansion under Pressure due to Sodium Intercalation in Carbon Cathode Materials for Aluminium Smelters.”, Light Metals, 1992, 801-808.

[44] Schreiner, H. and Øye, H.A., “Sodium Expansion of Cathode Materials under Pressure.”, Light Metals, 1995, 463-472.

[45] Liao, X. and Øye, H.A., “Effects of Carbon Bonded Coatings on Sodium Expansion of the Cathode in Aluminium Electrolysis.”, Light Metals 1999, 629-636.

[46] Støre, A., Foosnæs, T. and Øye, H.A., ”Sodium Expansion Results.”, to be published.

[47] Newman, D.S., Dahl, O., Justnes, H., Kopperstad, S. and Øye, H.A., "A Technique for Measuring In Situ Cathode Expansion (Rapoport Test) During Aluminum Electrolysis.", Light metals, 1986, 685-688.

[48] Richards, N.E., “Aspects of Interaction of LiF – Modified Bath with Cathodes.”, Int. Harald A. Øye Symp. Proceedings, Sørlie, M., Østvold, T., and Huglen, R (eds.), Trondheim, 1995, 143-157.

[49] Liao X. and Øye H.A., ”Increased Sodium Expansion in Cryolite-Based Alumina Slurries.”, Light Metals, 1998, 659-666.

[50] Liao, X., Naas, T. and Øye, H.A., “Enhanced Sodium Expansion in Alumina Oversaturated Melts.”, Aluminium, Vol. 73, 1997, 528-531.

[51] Guilliatt, I.F. and Chandler, H.W., “Stress Analysis in Carbon Cathode Beams During Electrolysis.”, Light Metals, Vol. 1, 1977, 437-451.

[52] Schreiner, H., “Sodium Expansion of Carbon Cathodes for Aluminium Electrolysis”, Thesis, Norwegian Inst. Technol., Trondheim, 1994.

[53] Allard, B. and Dumas, D., “High Temperature Mechanical Behaviour of Carbon Materials used in Aluminium Smelters.”, Light Metals, 1995, 783-790.

[54] Dergunov, N.N., Krotov A.I., Barabanov V.N. and Anufriev, U.P., “Tensile and Creep Behaviour of Polycrystalline Graphites.”, Carbon, Vol 10, 1972, 19-27.

[55] Patrick, J.W. and Walker, A., “Introduction to Carbon Science”, Ed. H. Marsh, Butterworths, London, Chapter 7, 1989, 229-258.

[56] Anderson, T.L., ”Fracture Mechanics, Fundamentals and Applications.”, 2nd ed., CRC-press, Florida, 1995.

[57] Patrick, J.W., “Microscopy of Porosity in Metallurgical Cokes.”, J. Microsc., Vol. 132, 1983, 333-343.

[58] Welch, B.J., Hyland, M.M., Utley, M., and Tricklebank, S.B., “Interrelationship of Cathode Mechanical Properties and Carbon/Electrolyte Reaction During Start-Up.”, Light Metals, 1991, 727-733.

[59] Sørgård, W. and Øye, H. A., Eurocarbon, Strasbourg, France, Supplementary references, 1998, X.7.

[60] Hop, J.G. and Øye, H. A., “In-Situ Strength Reduction of Anthracitic Cathode Carbon and Crack Quantifying by the Use of Image Analysis.”, Light Metals, 2001, 717-722.

[61] Slavin, V.V. and Blyushtein, M.L., “Determination of the Effect of Pre-Heating and Initial Electrolysis Conditions on the Service life of Carbon Cathodes.”, Izv. Tsvetn. Met, Vol. 1, 1981, 47-50.

[62] Hult, J.A.H., “Creep in Engineering Structures”, Blaisdell Publishing Company, USA, 1966.

[63] Zukas, E.G. and Green, W.V., “High Temperature Creep of a Poco Graphite.”, Carbon, Vol. 10, 1972, 519-524.

[64] Wagner, W. and Driesner, A.R., “High Temperature Mechanical Properties of Graphite. I. Creep in Compression.”, Journal of applied physics, Vol 30, No. 2, Feb, 1959, 148-151.

[65] Mrozowski, S., “Proceedings of the Conferences on Carbon.”, Waverly Press, Baltimore, Maryland, Vol. 156, 31-45, 195-215.

[66] Kotlensky, W.V., “Analysis of High Temperature Creep in Pyrolytic Carbon.”, Carbon, Vol. 4, 1966, 209-214.

[67] Mehta, K.P., Monteiro, P.J.M., “Concrete. Structure, Properties, and Materials”, Prentice-Hall, Inc., New Jersey, 1986.

[68] Findley, W.N., “Creep and Relaxation of Nonlinear Viscoelastic Materials”, North-Holland Publishing Company, Hungary, 1976.

[69] Rørvik, S. and Øye, H.A., “A method for Characterization of Anode Pore Structure by Image Analysis.”, Light Metals, 1996, 561-568.

[70] ISO/DIS 15379-1, “Carbonaceous Materials for the Production of Aluminium – Cathode blocks – Part 1: Determination of the Expansion due to Sodium Penetration with Application of Pressure”, to be standardided.

[71] Dahn, J.R., Sleigh, A.K, Shi, H., Reimers, J.N, Zhong, Q. and Way, B. M., “Dependence of the Electrochemical Intercalation of Lithium in Carbons on the Crystal Structure of the Carbon.”, Electrochim. Acta, Vol. 38, No. 9, 1993, 1179-1191

[72] Zolochevsky, A., Servant, G., Hop, J.G., Foosnæs, T. and Øye, H.A., “Creep and Sodium Expansion in a Semigraphitic Cathode Material.”, Light Metals, 2003, 595-602.

[73] Handbook of Chemistry and Physics, 62nd edition, CRC-press, Boca Raton, Florida, 1981-1982.

[74] Mardilovich, P.,P., Govyadinov, A., N., Mazurenko, N., I. and Paterson, R., ”New and Modified Anodic Alumina Membranes Part II. Comparison of Solubility of Amophous (normal) and Polycrystalline Anodic Alumina Membranes.”, Journal of Membrane Science, Vol. 98, 1995, 143 – 155.

[75] Panias, D., Asimidis, P. and Paspaliaris, I., ”Solubility of Boehmite in Concentrated Sodium Hydroxide Solutions: Model Development and Assessment.”, Hydrometallurgy, Vol 59, Issue 1, January 2001, 15-29.

Appendix A. $Al(OH)_x$ - AlF_y - pH system

The method to analyse the sodium content in carbon by backtitration will here be shown to be poor if the sample contains electrolyte (fluoride compounds). The crushed carbon samples containing electrolyte and sodium were left to react with 0.1 M HCl for several weeks. The solubility of the different melt species found in carbon cathodes after electrolysis [24, 30] is shown in Table A.1.

Table A.1. Solubility of the different species [73].

	Na_3AlF_6	**NaF**	**CaF_2**	**α - alumina**
Solubility in acid	insoluble	soluble	slightly soluble	slightly soluble
Solubility in alkali	soluble	soluble		

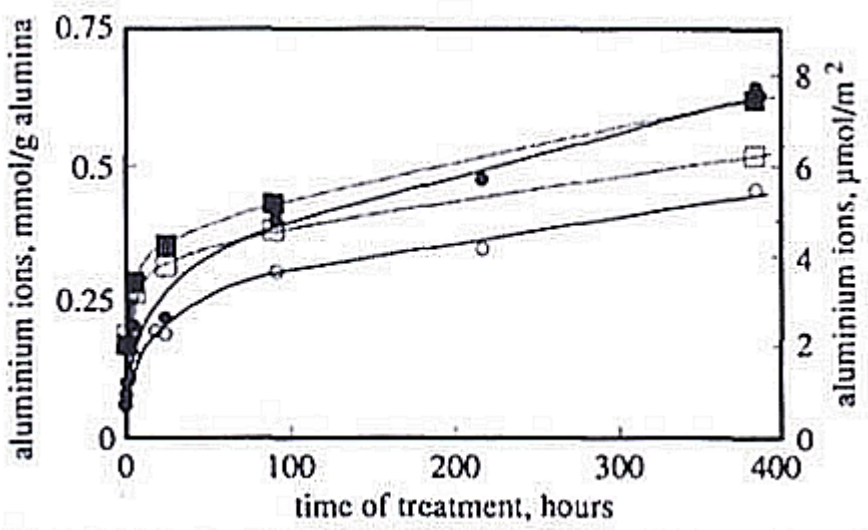

Figure A.1. Variation of the amount of the aluminium ion released into solution from γ-Al_2O_3 samples with time of treatment. 0.1 M HCl with stirring (•); 0.1 M HCl without stirring (0); 0.1 M NaOH with stirring (■); 0.1 M NaOH without stirring (□) [74].

Except for cryolite, which only is soluble in basic solution, all species are soluble to some extent in acid. Mardilovich et al. [74] studied solubility of amorphous and crystalline alumina powder. Between pH < 4.7 and pH > 9.0 crystalline alumina was found to dissolve slowly in 0.1 M HCl. After 2200 hours in 0.10 M HCl a solubility of 11.8 % was measured in a container with stirring, without stirring the solubility was 4.8 %. In the pH range 4.7 – 9.0 no solubility was measured. The time versus alumina solubility is shown in Figure A.1. The dissolution time looks suspiciously like the reaction time of sodium content with backtitration method of electrolysis samples [52].

The Al^{3+} - ions will be present as $Al(OH)_x$ or AlF_y – complexes. The equilibrium constants are shown in Table A.2.

Table A.2. Equilibrium constants for aluminium hydroxide [75] and aluminium fluorine and hydrofluoric acid [73].

Aluminium hydroxides:

Reaction	$-\log K$
$AlOOH_{(s)}+H_2O=Al^{3+}+3OH^-$	34.50
$Al^{3+}+H_2O=AlOH^{2+}+H^+$	5.01
$Al^{3+}+2H_2O=Al(OH)_2^{+}+2H^+$	9.30
$Al^{3+}+3H_2O=Al(OH)_3^{0}+3H^+$	15.0
$Al^{3+}+4H_2O=Al(OH)_4^{-}+4H^+$	22.82
$2Al^{3+}+2H_2O=Al_2(OH)_2^{4+}+2H^+$	7.60
$3Al^{3+}+4H_2O=Al_3(OH)_4^{5+}+4H^+$	13.90
$7Al^{3+}+17H_2O=Al_7(OH)_{17}^{4+}+17H^+$	59.48
$13Al^{3+}+32H_2O=Al_{13}(OH)_{32}^{7+}+32H^+$	107.47
$13Al^{3+}+28H_2O=Al_{13}O_4(OH)_{24}^{7+}+32H^+$	98.70
$5Al^{3+}+12H_2O=Al_5(OH)_{12}^{3+}+12H^+$	43.41
$6Al^{3+}+15H_2O=Al_6(OH)_{15}^{3+}+15H^+$	53.78
$14Al^{3+}+34H_2O=Al_{14}(OH)_{34}^{8+}+34H^+$	113.14
$8Al^{3+}+20H_2O=Al_8(OH)_{20}^{4+}+20H^+$	69.82
$9Al^{3+}+23H_2O=Al_9(OH)_{23}^{4+}+23H^+$	80.14
$10Al^{3+}+24H_2O=Al_{10}(OH)_{24}^{6+}+24H^+$	81.18

Aluminium fluorides:

$Al^{3+} + F^- = AlF^{2+}$	$\log K_1 = 6.1$
$Al^{3+} + 2F^- = AlF_2^{+}$	$\log K_2 = 11.1$
$Al^{3+} + 3F^- = AlF_3^{0}$	$\log K_3 = 15.0$
$Al^{3+} + 4F^- = AlF_4^{-}$	$\log K_4 = 18.0$
$Al^{3+} + 5F^- = AlF_5^{2-}$	$\log K_5 = 19.4$
$Al^{3+} + 6F^- = AlF_6^{3-}$	$\log K_6 = 19.8$

Hydrofluoric acid

$HF = H^+ + F^-$	$\log K_a = -3.17$

If sodium fluoride was the only melt species, the titration end point could be determined from the acid constant in the bottom of Table A.2:

$$pH = ½ (\log C_{TF} + pK_a + 14) = ½ \log C_{TF} + 8.585$$

where C_{TF} is the total flour content.

But due to the presence of aluminium a more complex system arises. The first 4 hydroxide and first 4 fluorides in Table A.2 are the major species in the system and the following equilibriums will be considered:

$$Al^{3+} + H_2O = Al(OH)_x^{3-x} + xH^+ \qquad K_x = \frac{\left[Al(OH)_x^{3-x}\right]\left[H+\right]^x}{\left[Al^{3+}\right]} \qquad \text{(A.1)}$$

$$Al^{3+} + yF = AlF_y^{3-y} \qquad K_y = \frac{\left[AlF_y\right]}{\left[Al^{3+}\right]\left[F\right]^y} \qquad \text{(A.2)}$$

$$HF = H^+ + F^- \qquad K_a = \frac{\left[H^+\right]\left[F^-\right]}{\left[HF\right]} \qquad \text{(A.3)}$$

The total concentration of aluminium and fluorides are respectively:

$$C_{Al} = \sum_{y=1}^{4}\left[AlF_y\right] + \sum_{x=1}^{4}\left[Al(OH)_x^{3-x}\right] + \left[Al^{3+}\right] \qquad \text{(A.4)}$$

$$C_F = \sum_{y=1}^{4}\left[AlF_y\right] + \left[HF\right] + \left[F^-\right] \qquad \text{(A.5)}$$

If Eq. (A.4) is solved with respect to Al^{3+} and put into C_F, a fifth order equation with fluorine as variable is achieved. If this equation is solved for each pH a diagram presented in Figure A.2 is achieved for $C_F = 0.025$ and $C_{Al} = 0.00553$. This corresponds to 0.4 g melt with CR = 4 and 10 % alumina solved in one litre of HCl. No solution for F^- for pH = 8.5 and higher was found so F^- was set equal to the total F concentration.

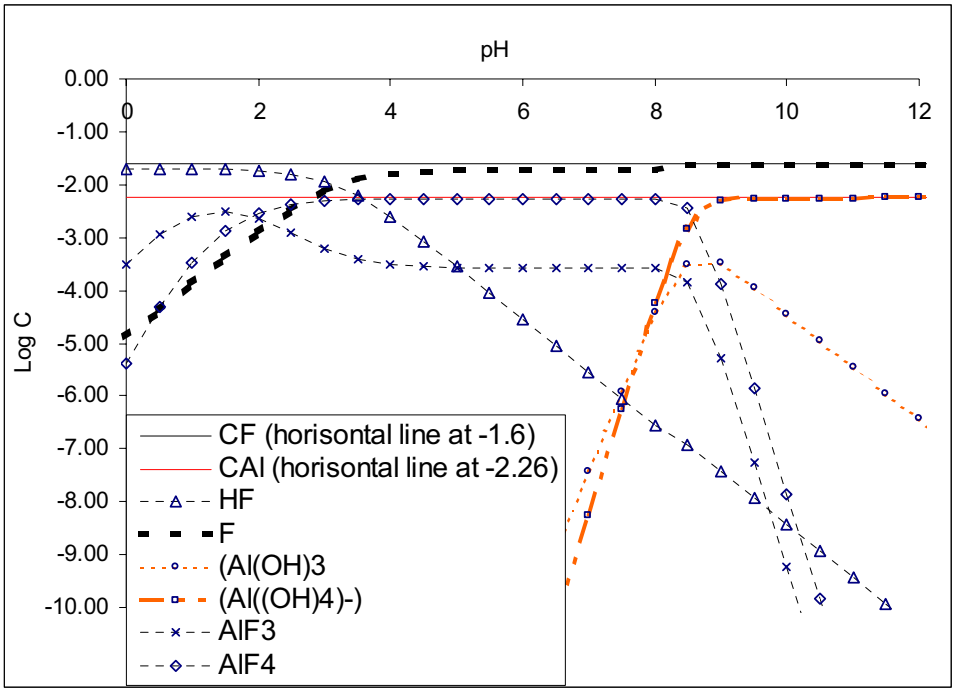

Figure A.2. Concentration of the different species versus pH with 0.4 g melt (CR = 4, 10 % alumina). Only the dominant species are shown to make it surveyable.

$Al(OH)_3$ is not the major Al(OH) - specie at a given pH. If only the aluminium hydroxide system is considered (Figure A.3) the $Al(OH)_3$ – species is dominant at pH between 6.5 – 7.0. The pH with the maximum $Al(OH)_3$ concentration depends on the fluoride content (Compare Figure A.2 and A.3).

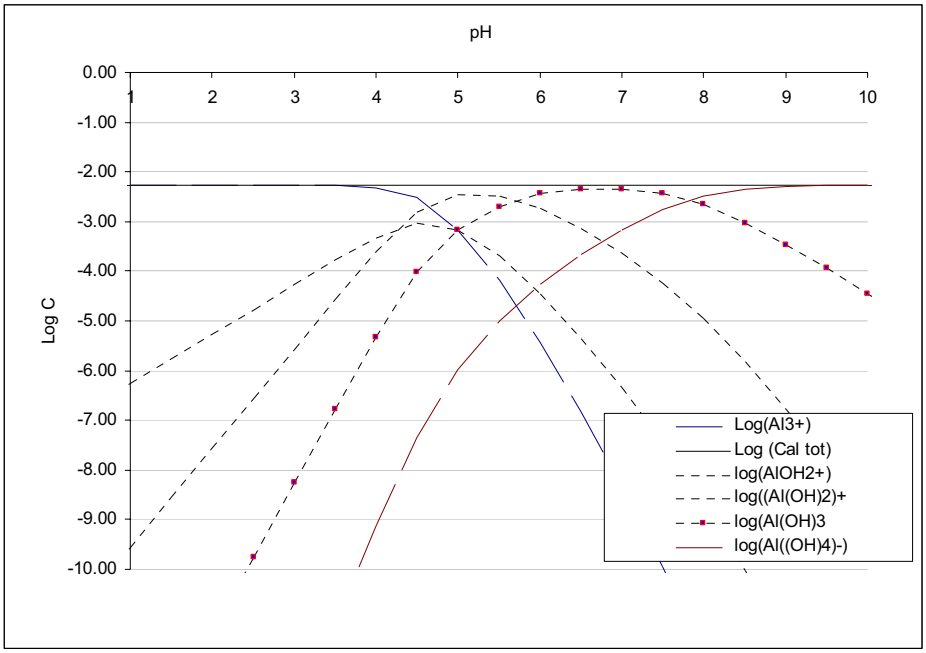

Figure A.3. Log(concentration) versus pH for $Al(OH)_x^{y-}$.

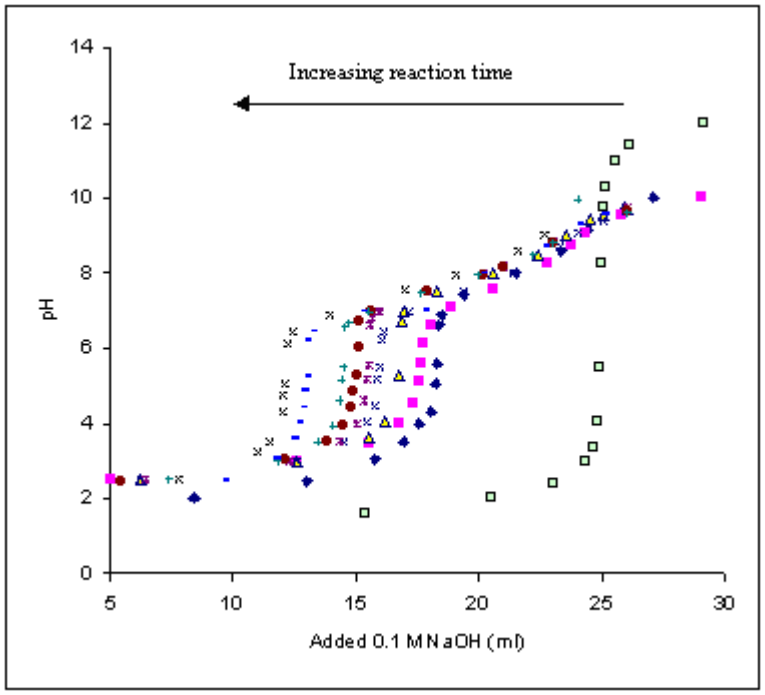

Figure A.4. Titration curves for one sample versus time.

If the total aluminium and fluoride were known there is still a problem with the solubility of cryolite only in basic solution and the precipation and slow solubility of alumina/aluminium hydroxide.

An example of a titration curves versus reaction time (12 to 500 hours) for an electrolysed sample (17 grams in one litre) is shown in Figure A.4. The rightmost curve is a blank titration curve where no sample was put in the acid. The curves move left with time. At which pH $Al(OH)_3$ dominates (if it dominates) is hard to say because of the fluoride complexes.

Appendix B. Anthracite properties

Elkem Carbon: Analysis of green anthracite lot

Type		**Standard Anthracite**
Lot no standard	unit	99054
Vitrinite reflectance		**2.95**
Hydrogen content	%	**3.07**
Volatile matter	%	**8.3**
Moisture content	%	**11.2**
Hg apparent density (-2+1mm)	kg/dm3	**-**
Vibrated Bulk Density *	kg/dm3	**795**
Sulphur	%	**0.19**
Fix C		**87.8**
Ash content, 800 °C		**3.91**
AAS / XRF	Na	**0.08**
	Mg	**0.14**
	Al	**0.33**
	Si	**0.56**
	K	**0.013**
	Ca	**0.36**
	Ti	**0.015**
	Fe	**0.34**
	P	**0.004**

- Not measured
* Measured by Elkem Research

99054: Standard anthracite used for lab scale heat treatment

Appendix C. Melt analysis

The premelted bath used for the electrolysis experiments was analysed at the research centre of Hydro Aluminium in Årdal. The phases were quantitative determined by XRD analysis by the Rheinveld method; and XRF elemental analysis using a dedicated electrolyte bath application.

Elemental Analysis

The measurement was made on a Philips PW2400 x-ray fluorescence spectrometer (XRF) running the SuperQ program package[1]. The elemental composition is shown in Table C.1 as the average of 2 parallel measurements. The application uses a calibration for each element and the sum was not normalised. See Table C.4 for a comparison with the major elements estimated from phase analysis.

Table C1. Elemental analysis from XRF (wt%). The results are from a dedicated bath application and are accurate (2s) within 5 % relative for heavier elements (>S) and 10 % relative for F to Cl. The accuracy for oxygen is only within 20 % relative. There is a problem with the calibration for Cl and K and these elements are estimated too low.

	Unit	Mean	P.1	P.2
O	(%)	3.9	3.84	4.04
F	(%)	56.6	56.50	56.60
Na	(%)	29.9	29.80	29.90
Mg	(ppm)	355	360	351
Al	(%)	14.0	14.00	14.00
Si	(ppm)	535	534	536
P	(ppm)	39	39	40
S	(ppm)	381	388	375
Cl	(ppm)	0	0	0
K	(ppm)	0	0	0
Ca	(%)	2.8	2.76	2.76
Ti	(ppm)	13	13	12
V	(ppm)	6	5	7
Fe	(ppm)	254	252	256
Ni	(ppm)	19	19	19
Cu	(ppm)	7	7	7
Zn	(ppm)	6	6	6
Ga	(ppm)	8	9	7
Cr	(ppm)	11	11	11
Mn	(ppm)	5	5	4
Co	(ppm)	10	8	11
Sr	(ppm)	46	44	49
Ba	(ppm)	16	15	17
SUM			107.125	107.429
LECO C		n.m.	n.m.	n.m.
SUM XRF trace elements	(%)		0.172	0.171

[1] SuperQ Instrument Control and Data Aqusition Program for Philips XRF PV2400, Philips Analytical X-Ray B.V., Almelo 1997-2002.

Phase Analysis

The phase scan was recorded on a Philips PW1800 x-ray diffractometer (XRD) running the Philips APD program package. The phase composition was determined by the Rietveld method[2] using the program Riqas[3]. The result is given in Table C.2 and the CR calculated from the phases in Table C.3.

The XRD diffractogram phase scan with identified phases is shown in Figure C.1 where the black line is the measured diffractogram, and the green the calculated composition.

Table C.2. Phases from XRD (wt%). The SUM is not corrected for XRF trace elements. The detection limit for the phases is in the range 0.1 to 0.5 wt% and a measurement below 0.5 wt% is uncertain and either false or if the phase is present, probably too low. ESD=Estimated Standard Deviation.

	Concentration	ESD
$Na_5Al_3F_{14}$	1.0	0.2
Na_3AlF_6	75.0	0.6
NaF	13.9	0.2
a-NaCaAlF6	0.0	
$Na_2Ca_3Al_2F_{14}$	0.3	0.1
CaF_2	5	0.1
α-Al_2O_3	0.4	0.1
β-Al_2O_3	4.5	0.2
SUM	100.1	
C from LECO	n.m.	
SUM XRF Trace elements	0.171	

[2] J. E. Post, D. L. Bish, Rietveld Refinement of Crystal Structures Using Powder X-ray Diffraction Data, Modern Powder Diffraction, Reviews in Mineralogy Vol. 20 1989 ISBN 0-939959-24-3 pp.277-308.

[3] Riqas Release 4, a System for the Analysis of XRD Powder Diffraction Data Employing Rietveld and Whole-Pattern Fitting, Riqas Ver 4.0 User's Guide, Materials Data Inc., Livermore CA USA, 1996-2002.

Table C.3 Bath acidity from thorium nitrate titration and the XRD phase analysis. The titration is the reference method. The values for 'CR from titration' were estimated using the phase concentrations.

	From Phases	From Supplier
Bath acidity from titration	n.m.	
Bath acidity from phases	-8.93	
CR from titration	n.m.	
CR from phases	3.88	4.0

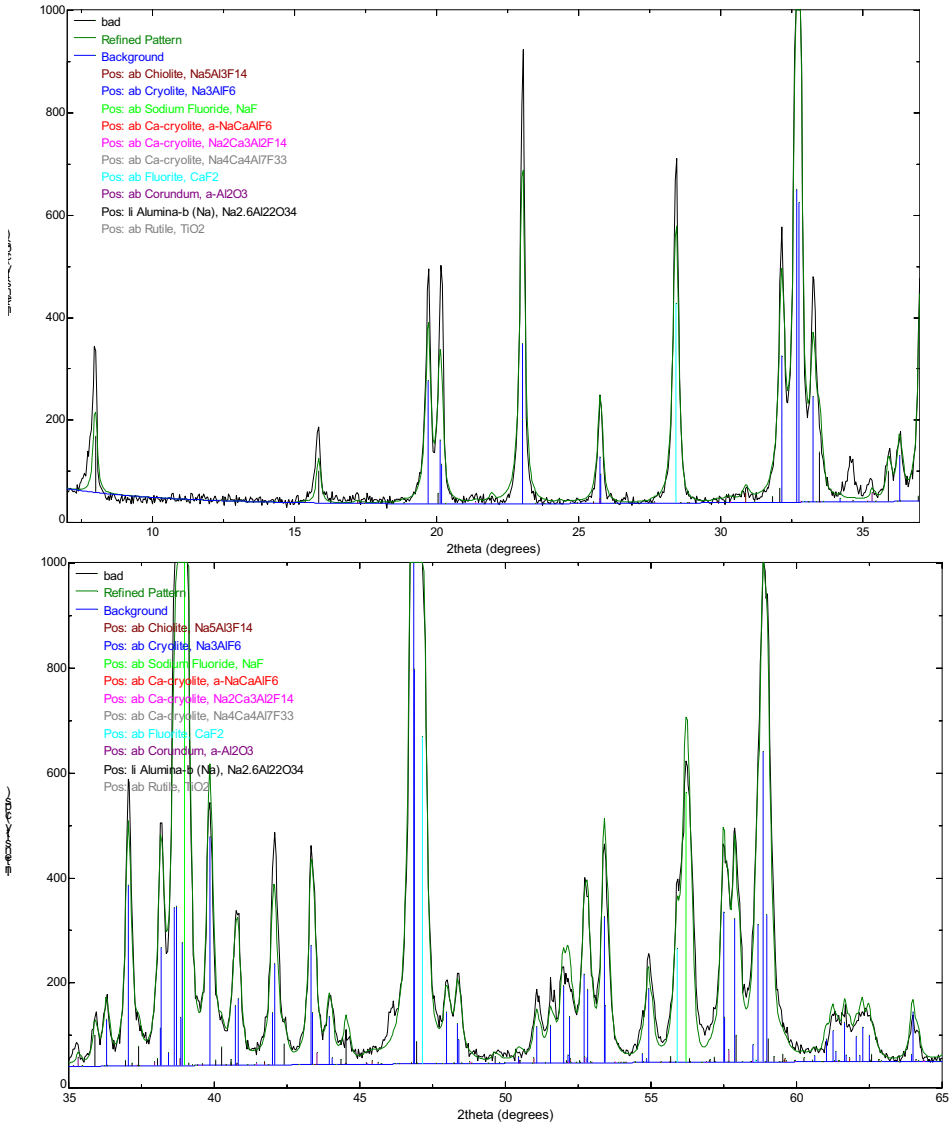

Figure C.1. XRD diffractogram of the melt sample with phases. The upper scan is 7-37°2theta and lower is 35-65° 2theta. The major phases are Na_3AlF_6, NaF, CaF_2 and β-Al_2O_3, and there are traces of $Na_5Al_3F_{14}$ and α-Al_2O_3. All peaks are identified except the minor peaks at 34.6 and 46.1°2 theta.

The amounts of oxygen and trace metals were estimated from the phases and are compared to the XRF determination in Table B.4. The close agreement of the CR from the phase analysis with the value given by the supplier indicates that for the major elements the concentrations from XRD are probably more correct.

Table C.4. The results for the elements from XRF (direct measurement) and XRD (calculated from phases). The XRF results are not normalised while the XRD results are normalised including the trace elements from XRF.

	Unit	XRF	XRD
O	(%)	3.9	2.25
F	(%)	56.6	50.06
Na	(%)	29.9	32.62
Mg	(ppm)	355	n.m.
Al	(%)	14.0	12.29
Si	(ppm)	535	n.m.
P	(ppm)	39	n.m.
S	(ppm)	381	n.m.
Cl	(ppm)	-237	n.m.
K	(ppm)	-44	n.m.
Ca	(%)	2.8	2.63
Ti	(ppm)	13	n.m.
V	(ppm)	6	n.m.
Fe	(ppm)	254	n.m.
Ni	(ppm)	19	n.m.
Cu	(ppm)	7	n.m.
Zn	(ppm)	6	n.m.
Ga	(ppm)	8	n.m.
Cr	(ppm)	11	n.m.
Mn	(ppm)	5	n.m.
Co	(ppm)	10	n.m.
Sr	(ppm)	46	n.m.
Ba	(ppm)	16	n.m.
SUM			99.86
LECO C		n.m.	n.m.
SUM XRF trace elements	(%)		0.144

Appendix D. Stresses in a Rapoport sample

Zolochevsky et al. [29] calculated the stresses induced by sodium in a Rapoport sample at different current densities. Creep was not included in the calculation . The material constants was:
E - modulus = 4.2 MPa
Poisson ration = v = 0.25
Pressure on top of cylinder = 2.3 MPa

The calculated sodium concentration profile is shown in Figure D1. The resulting axial stresses are shown in Figure D2.

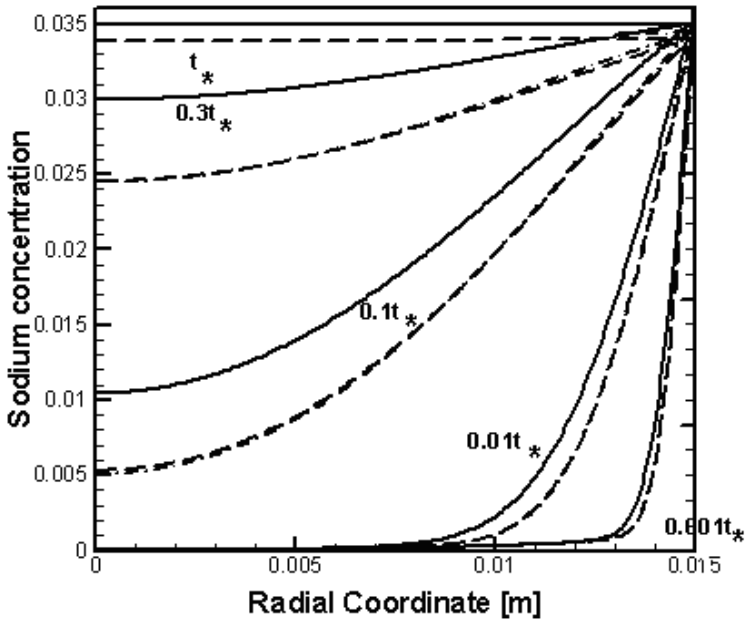

Figure D1. Distribution of sodium in a Ø30 Rapoport sample during time. The radial coordinate (r) = 0.015 corresponds to the surface of the cylinder, r = 0 is the centre. The solid line shows the distribution with a current density of 0.7 A/cm^2 and the dotted for 0.2 A/cm^2. The time t* corresponds to 128 minutes for i = and 0.7 A/cm^2 and 200 minutes for i = 0.2 A/cm^2.

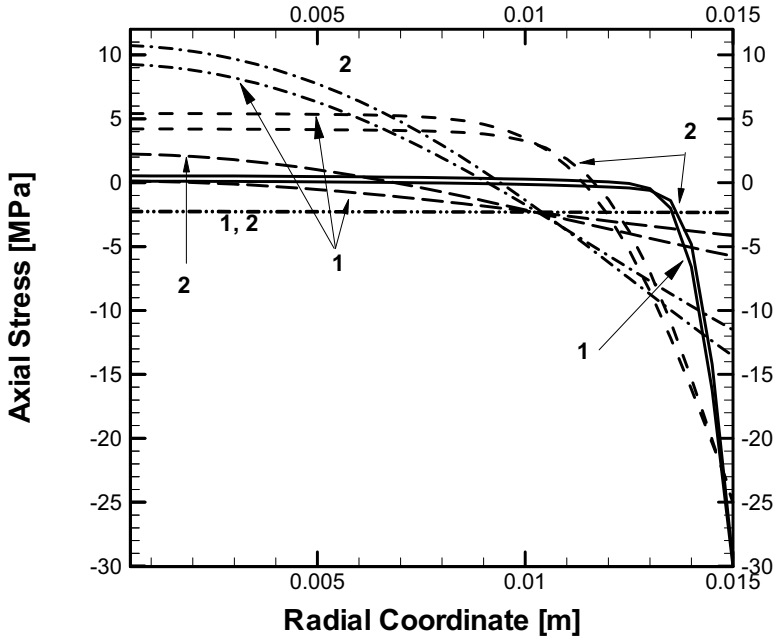

Figure D2. Distribution of the axial stress with time in a solid cylinder with i = 0.7 A/cm^2 (1) and i = 0.2 A/cm^2 (2). Time of sodium saturation: 0.001t (————), 0.01t (----------), 0.1t (·····), 0.3t (— — —), t (— ·· — ·—). t = 128 min for i = 0.7 A/cm^2 and t = 200 min for i = 0.7 A/cm^2.

When the electrolysis is started in a Rapoport experiment sodium will penetrate and induce compressive stresses in the cylindrical sides. Tensile stresses will arise in the sample middle. The stresses will relax with time as sodium saturates the sample (not because of creep).

If creep is regarded the inner tensile stressed part of the sample will expand with time. But as the electrolysed side material is containing sodium, this part of the material might creep more. So, much of the creep strain will be compressive in the outer part of the sample in the initial part of electrolysis. Stress relaxation will also occur and the above calculated stresses will be smaller than shown.

After t = 0.1 (Figure D.1) the sodium has reached the inner part of the sample while tensile stresses still is present (Figure D.2). If the creep in tension is assumed similar as creep in compression, the inner part of the sample will have increased creep properties because of sodium and further creep faster. As the tensile strength of these materials is in the order 1/5 of the compressive creep, a smaller stress is probably needed for the same creep strain in tension as in compression.

Appendix E. Calculation of sodium concentration

Input:
Current efficiency for sodium production is 100 %
Sample 65 g.
720 seconds (12 minutes) of electrolysis

A current density i = 0.2 A/cm^2 gives a total current (I) on the surface area (A) of a sample with a height h = 6 cm with a radius r = 1.5 cm:

$A = 2 \cdot \pi \cdot r \cdot h = 2 \cdot 3.14 \cdot 1.5 \cdot 6 = 56.52$ cm^2

$I = A \cdot i = 56.52 \cdot 0.2 = 11.3$ A

Produced sodium (m = molar mass of sodium = 23 g/mol, F = Faraday = 96500 Q/mol):

$Itm/nF = 11.3 \cdot 720 \cdot 23/1 \cdot 96500 = 1.94$ g

Concentration of sodium

100%*1.94g/65g = **2.98 %**